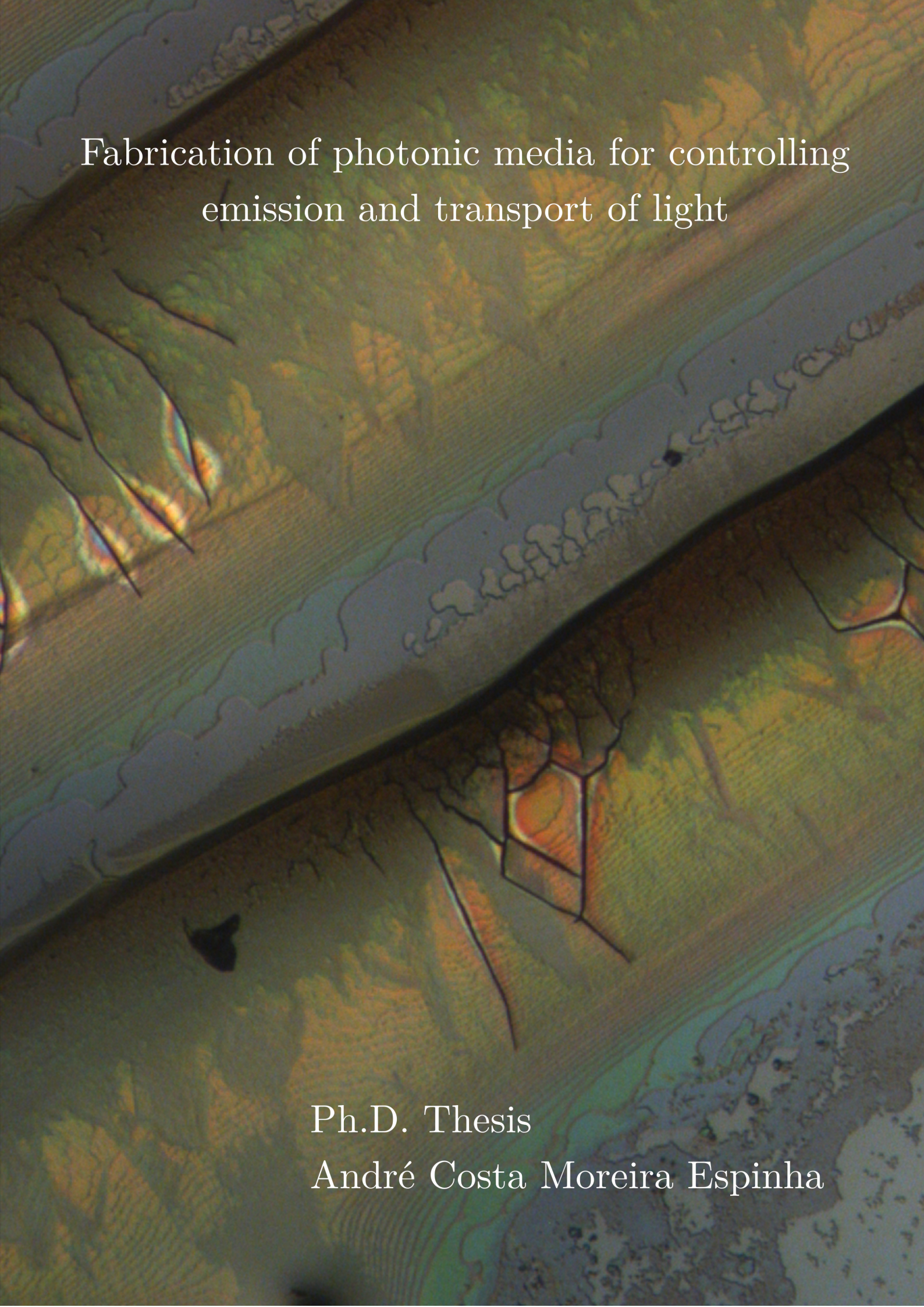

Fabrication of photonic media for controlling emission and transport of light

Ph.D. Thesis

André Costa Moreira Espinha

Universidad Autónoma de Madrid

Faculdad de Ciencias

Fabrication of photonic media for controlling emission and transport of light

Fabricación de medios fotónicos para el control de la emisión y transporte de luz

Memoria presentada para obtener el grado de
Doctor en Física de la Luz y de la Materia por:

André Costa Moreira Espinha

Tesis dirigida por:

Prof. Ceferino López Fernández
Dr. Álvaro Blanco Montes

Tutor:

Prof. Luis Viña Liste

Instituto de Ciencia de Materiales de Madrid

Consejo Superior de Investigaciones Científicas

June 2015

"Enfim duma escolha faz-se um desafio
Enfrenta-se a vida de fio a pavio
Navega-se sem mar, sem vela ou navio
Bebe-se a coragem até dum copo vazio..."

Sergio Godinho

To my family

To Conchi

Summary

This thesis is the result of research on different photonic systems, developed in the Materials Science Institute of Madrid - ICMM (which belongs to the national research council of Spain - CSIC). It is especially dedicated to the search for new functionalities in photonic crystals or disordered materials. The work herein described has been performed in the Photonic Crystals Group, under the supervision of Prof. Ceferino López and Dr. Álvaro Blanco. The thesis has been funded by the *Ministerio de Ciencia e Innovación* (MICINN), now *Ministerio de Economia y Competitividad* (MINECO) (FPI 2010 grant programm). All the samples described were fabricated in the chemical laboratories of the referred group. The programable systems based on shape memory polymers were developed in colaboration with Dr. María Concepción Serrano of the Group of Bioinspired Materials - ICMM, currently at the National Paraplegic Hospital, SESCAM, in Toledo. The work described has been published in the following papers:

1. A. Espinha, M. Ibisate, J. F. Galisteo-López, A. Blanco, C. López, "One-step-process composite colloidal monolayers and further processing aiming at porous membranes," *Langmuir*, vol. 28, issue 37, pp. 13172–80, 2012.

2. A. Espinha, M. Concepción Serrano, A. Blanco, C. López, "Thermoresponsive shape-memory photonic nanostructures," *Advanced Optical Materials*, vol. 2, issue 6, pp. 516-521, 2014.

3. A. Espinha, M. Concepción Serrano, A. Blanco, C. López, "Shape-memory effect for self-healing and biodegradable photonic systems,"

SPIE Proceedings - Photonic Crystal Materials and Devices XI, 91270B, 2014.

4. A. Espinha, M. Concepción Serrano, A. Blanco, C. López, "Random lasing in novel dye-doped white paints with shape memory," *Advanced Optical Materials*, DOI: 10.1002/adom.201500128, 2015.

Communications at national and international conferences presented by me:

1. A. Espinha, M. Ibisate, J. F. Galisteo-López, A. Blanco, C. López, "Surface nano-structuration using composite colloidal monolayers," CEN 2012: Conferencia Española de Nanofotonica, 1-4 October 2012, Carmona (Sevilla), Spain. **Oral**.

2. A. Espinha, M. C. Serrano, A. Blanco, C. López, "Reprogramable two-dimensional surface patterns using multifunctional polymers," Nanospain Conference, 11-14 March 2014, Madrid, Spain. **Poster**.

3. A. Espinha, M. C. Serrano, A. Blanco, C. López, "Shape-memory effect for self-healing and biodegradable photonic systems," SPIE Photonics Europe, 14-17 April 2014, Brussels, Belgium. **Oral**.

4. A. Espinha, M. Ibisate, E. Calle, A. Blanco, C. López, "Fine tuning of light transport in resonant random media," CEN 2014: Conferencia Española de Nanofotonica, 14-16 May 2014, Santander, Spain. **Oral** and **Poster**.

5. A. Espinha, M. C. Serrano, A. Blanco, C. López, "Nanocomposite materials for shaping the diffusive transport of light," NanoPT International Conference, 11-13 February 2015, Oporto, Portugal. **Poster**.

6. A. Espinha, M. C. Serrano, A. Blanco, C. López, "Engineering light transport in titania-doped multifunctional elastomers," Imaginenano 2015, 10-13 March 2015, Bilbao, Spain. **Oral** and **Poster**.

Communications at european scientific meetings presented by me:

1. A. Espinha, M. Ibisate, A. Blanco, C. López, "Fabrication of nanostructured media towards the development of photonic materials," Workshop Nanophotonics for Energy Efficiency, 8-13 November 2011, Erice, Italy. **Poster**

2. A. Espinha, M. Ibisate, J. F. Galisteo-López, M. C. Gonçalves, L. Fortes A. Blanco, C. López, "Rare earth doped inverse silica opals for efficient NIR light sources," N4E Hybrid Nanophotonics Workshop, 26-27 March 2013, Shouthampton, England. **Poster**.

3. A. Espinha, M. Ibisate, E. Calle, A. Blanco, C. López, "Fine tuning of light transport in resonant random media," Nanophotonics for Energy Efficiency User Meeting, 16-17 June 2014, Istambul, Turkey. **Oral**.

4. A. Espinha, M. C. Serrano, A. Blanco, C. López, "Reprogrammable two-dimensional surface patterns using multifunctional polymers," Summer School Waves and disorder, 30 June - 12 July 2014, Cargese (Corsica), France. **Oral**.

5. A. Espinha, A. Blanco, C. López, "Design of smart materials for engineering the diffusive transport of light," Nanophotonics for Energy Efficiency Final User Meeting, 11 - 12 December 2014, Castell de Fels (Barcelona), Spain. **Oral**.

Contents

List of abbreviations

ASE	Amplified spontaneous emission
CBC	Coherent backscattering cone
DSC	Differential scanning calorimetry
FIS	Fourier image spectroscopy
FTIR	Fourier transform infrared spectroscopy
IO	Inverse opal
PBG	Photonic band gap
PC	Photonic crystal
PDDC-HD	Poli(dodecanediolcitrate) hydroxyl dominant
PMMA	Polymethylmethacrylate
PL	Photoluminescence
PS	Polystyrene
RE	Rare Earth
RhB	Rhodamine B
RL	Random laser
SEM	Scanning electron microscopy
SME	Shape memory effect
SMP	Shape memory polymer

1

Introduction and key concepts

Throughout the history, incredible advances have been achieved regarding the basic understanding of light nature, as well as its use and manipulation. We know that mirrors fabricated with polished copper were already used in the ancient Egypt and that the rectilinear propagation of light, as well as reflection and refraction phenomena, were familiar to the Greek civilization. From those initial studies in optics to the dispersion experiments of Sir Isaac Newton and his corpuscular theory of light, to the wavelike behavior defended by Christiaan Huygens, to the double slit interference experiments carried out by Thomas Young, a long path was covered. The 19^{th} century was a golden period for optics, for example with the contributions of Michael Faraday unraveling the relation between light and electromagnetism and James Maxwell mathematical unification of phenomena in terms of a series of elegant equations (this year celebrates their 150^{th} publication anniversary). A huge revolution also took place during the 20^{th} century with the establishment of quantum mechanics and the wave-particle duality. Applied optics flourished considerably, especially in the second half of the century, with the invention of the laser, the optical fiber and, more recently, solid state devices.

Nowadays, light technologies are fundamental in areas such as illumination, information transmission and storage, sensing, medical diagnostics and energy, just to number a few. The essential role of light in our society was recognized by the United Nations, by selecting 2015 as the International Year of Light and Light-based Technologies. This choice aimed at raising awareness about how light science is vital for answering the global challenges faced today and how it is a key vector for a sustainable development. Its importance was also perfectly grasped by Pierre Aigrain, a french scientist, that in analogy with electronics - the science of electrons manipulation - introduced in 1967 the term “photonics” for designating the science of photons:

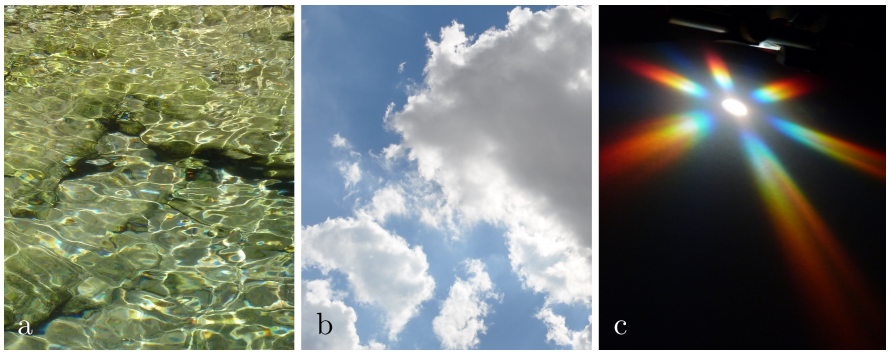

Figure 1.1: Physical phenomena resulting from light propagation and interaction in different media: a) homogeneous, b) diffusive and c) diffracting.

> "Photonics is the science of the harnessing of light. Photonics encompasses the generation of light, the detection of light, the management of light through guidance, manipulation and amplification, and most importantly, its utilization for the benefit of mankind."

Photonics deals with several physical phenomena that occur when light interacts with matter. Animals are able to see objects because they scatter, reflect and/or absorb light impinging upon them. An object that does not absorb or scatter radiation looks transparent (it would be invisible) and light interacting with it experiences only reflection and refraction at its interfaces. For example, at the surface of clear water (Figure 1.1a) one can observe bright spots of reflected light but additionally, one may also see the bottom of the pound due to transmitted and refracted light. An object that does not absorb but scatters with equal efficiency at all regions of the visible electromagnetic spectrum looks white. A paradigmatic example of such a system are clouds in the sky, where light is scattered by small drops of water (Figure 1.1b). On the contrary, if a medium strongly absorbs at all wavelengths, it looks black. Furthermore, in structured periodic media like artificial opals, light may undergo diffraction which is related to constructive or destructive interference for specific directions of space (Figure 1.1c). As may be observed in the figure, due to the fact that the diffraction angle is dependent on the radiation wavelength, white light impinging on the material is also dispersed and therefore one can observe beautiful spatial color separation.

If on one hand it is essential to understand the nature of light and the way in which it interacts with matter, the reciprocal is also true. It is of extreme importance to develop materials and optical systems that may effectively control ligh propagation in new and versatile ways. In fact, the comprehension

and manipulation of light have grown hand-in-hand with the search for new materials with enhanced functionalities. Examples are waveguides, photonic crystals, photonic random media, non-linear optical materials, metamaterials, plasmonic systems, nano-antennas and amplifying gain media, among others. In this sense, the work carried out in this thesis, aims at stimulating novel research approaches in photonics and optical functional materials, particularly from the perspective of multifunctionality.

In what follows, we start by presenting the characteristics of photonic crystals (especially focusing on self-assembled ones) and random media, which are the kind of materials directly explored in this thesis. At the same time, we try to provide a brief overview of how light interacts with these media and how they constitute an effective multifunctional platform with demonstrated potential for light manipulation. We proceed with an introduction to shape memory polymers, which were used for investigating the possibility of fabricating novel kinds of programmable photonic systems, both ordered and diffusive. We end the current chapter with an outline of the following sections of this thesis.

1.1 Photonic crystals

In natural or man-made materials the color is most of the times a result of pigmentation. This means that, in general, colored media absorb and therefore subtract, some regions of the white light spectrum shining upon them. Nevertheless, this is not the only color mechanism known. Curiously, some butterfly wings or bird feathers, which are composed of non-absorbing materials like chitin or keratin, exhibit brilliant colors that are instead due to their micro and nanostructures. This mechanism is named structural color and, in the last decades, has been extensively studied and reported in a wide list of new artificially produced materials. Structured non-absorbing dielectrics have been explored for fabricating optical components able to reflect, confine or guide light in novel ways. A paradigmatic example of this kind of systems are photonic crystals (PCs), first proposed in 1987 by S. John [1] and E. Yablonovitch [2].

PCs are defined as materials that present a refractive index periodicity in one, two or three spatial directions (Figure 1.2). The length scale of that modulation should be of the order of magnitude of the operation wavelength for which they are designed. To taylor their properties and tune their spectral features, a number of parameters can be acted on, being the dimensionality, the symmetry, the topology, the lattice parameter, the effective refractive index and the refractive index contrast. Configuring these parameters, one

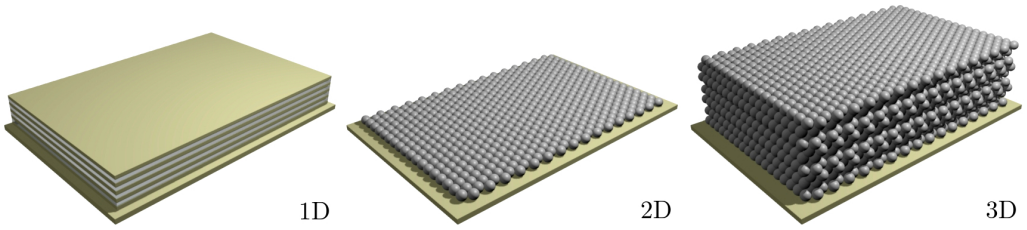

Figure 1.2: Scheme illustrating photonic crystals with different kinds of dimensionality. Spatial periodicity might occur in one, two or three dimensions of the space.

can achieve materials that interact with light in a way analogous to that of electrons interacting with semiconductors, that is to say, some gaps with no allowed energy states are opened in their dispersion relation. The refractive index in the case of PCs plays the role of the periodic atomic potential for electrons. In what follows, we focus our attention on artificial opals which are of relevance for the work presented in this thesis.

Artificial opals are obtained by self-assembly methods and are composed of spheres arranged in a face centered cubic (fcc) structure as the one illustrated in Figure 1.3a. Similar to x-rays interacting with atomic crystals, interference of light from crystalline planes of opals gives rise to diffraction (Figure 1.3b) and therefore, using Bragg's law, it is possible to estimate the wavelength of the Bragg peak (λ_B). Due to thermodynamics of the growing process, the direction parallel to the substrate is, in general, the [1 1 1], which is also the one typically probed experimentally. Consequently, considering that the diameter of the spherical building blocks is ϕ and the interplanar distance is $d_{111} = \sqrt{(2/3)}\,\phi$, at normal incidence λ_B is given by

$$\lambda_B = 2d_{111}\sqrt{fn_s^2 + (1-f)n_v^2}, \tag{1.1}$$

where f is the volume fraction occupied by the spheres, n_s is the refractive index of the spheres and n_v is the refractive index of the medium in which they are embedded. In this sense, a bare opal is composed of solid spheres in air and, on the contrary, an inverse one is composed of spherical air voids in a solid matrix. Although very useful, Equation 1.1 does not provide any information about the width of the Bragg peak or its intensity. A more complete description is therefore required.

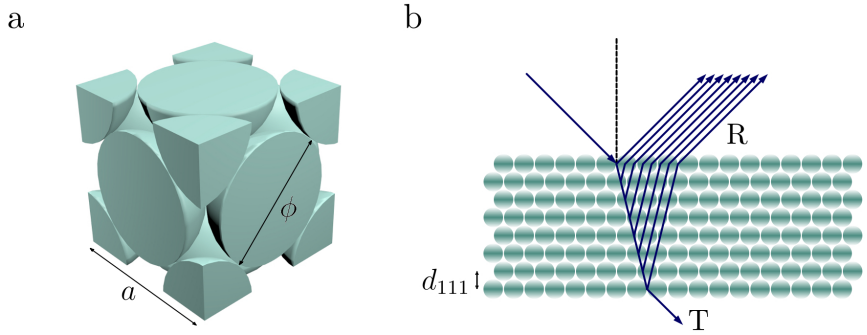

Figure 1.3: a) Scheme exhibiting the unitary cell for a face centered cubic structure. b) Scheme illustrating diffraction from crystalline planes along the d_{111} direction in a three dimensional PC.

1.1.1 Photonic band structure

As seen in the last section, due to the periodicity, the interference of waves diffracted by the crystalline planes of PCs may be either constructive or destructive for certain energies and regions of the space. A more complete description than that provided by the Bragg's law may be obtained solving the Maxwell equations for light propagation within the periodic medium. Their solution results in a so called photonic band structure, which is a dispersion relation expressed as $\omega = \omega(\mathbf{k})$ where ω is the angular frequency and $\mathbf{k}$ is the wave vector. After some manipulation, the Maxwell equations may be combined into the wave equation

$$\nabla \times [\frac{1}{\varepsilon(\mathbf{r})} \nabla \times \mathbf{H}(\mathbf{r})] = \frac{\omega^2}{c^2} \mathbf{H}(\mathbf{r}). \tag{1.2}$$

In general, the problem is stated in terms of the magnetic field $\mathbf{H}(\mathbf{r})$ so that the operator acting on $\mathbf{H}(\mathbf{r})$ is Hermitian. In this case, solving the equation translates into solving an eigenvalue problem. This would not be the case if the electric field was to be used. In Equation 1.2, $\varepsilon(\mathbf{r})$ is the dielectric constant of the medium and c is the speed of ligth in vacuum. The periodicity of the dielectric constant enables the use of Bloch's theorem [3] and so the solutions to the equation (its eigenvectors) are Bloch modes of the form

$$\mathbf{H}_{nk}(\mathbf{r}) = e^{i\mathbf{kr}} u_{nk}(\mathbf{r}), \tag{1.3}$$

$u_{nk}(\mathbf{r})$ being a periodic function with the same periodicity as the dielectric constant. Therefore, for each wave number $\mathbf{k}$ an infinite set of modes labeled by the integer n are found, defining the n^{th}-photonic band.

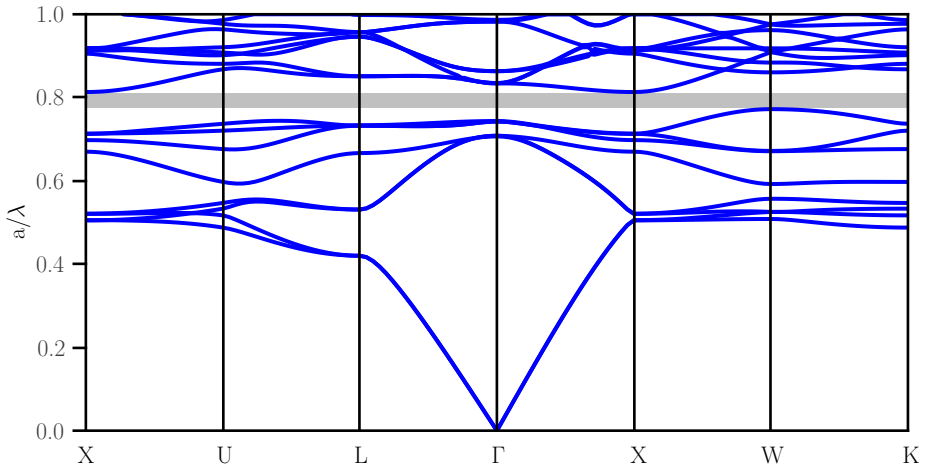

Figure 1.4: Band structure of a PC composed of air spheres embedded in a silicon matrix forming an fcc structure.

An example of the band structure of an artificial opal, composed of air voids in a silicon matrix, arranged in a fcc structure is exhibited in Figure 1.4. As may be observed, due to the periodicity, gaps are opened for specific directions of the reciprocal space meaning that there are no states to which light can couple. One can now conclude that Equation 1.1 describes the gap opened along the ΓL direction. This mentioned example, alongside with its respective band structure, is of particular relevance because a full photonic band gap (fPBG) is present between the eighth and nineth bands (signaled with a grey rectangle in the figure). Its presence implies that no radiation with energies inside the gap may propagate inside the PC. Furthermore, in Figure 1.4, one can also observe the presence of very flat bands that imply a slow group velocity (v_g) for photons, defined as

$$v_g = \nabla_k \, \omega(k) \, . \tag{1.4}$$

Therefore, bands with very small slopes such as those near a gap border or at high energy regions may be connected with slow propagation of light.

1.1.2 Self-assembled colloidal crystals

For the fabrication of PCs there are essentially two possible approaches namely *top-down*, in which small features are obtained by patterning large pieces of raw materials, and *bottom-up* where inversely, structure is materialized by the natural assembly of smaller building blocks. The first methods

usually allow for more flexibility when designing the structures (a quite spectacular example are quasi-crystals [4]). Nevertheless they typically require expensive equipment such as lithography systems or direct writing setups, they are very time consumming and also its difficult to achieve large coverage areas. On the other hand, *bottom-up* techniques allow for the production of reasonable quality crystals at a low cost. This is the reason why this kind of approaches has been tested more and more.

Colloidal crystals are produced by *bottom-up* methods and are generally composed of spherical particles. These are straightforward to synthesize and more convenient to self-assemble. In thermodynamical equilibrium, they tend to organize in a fcc structure as demonstrated by Woodcock [5]. Usual chemical compositions are silica, polystyrene and poli(methylmethacrylate) and they may be obtained in a wide range of diameters.

One of the first approaches for their fabrication was natural sedimentation, meaning that the colloid was left to evaporate subjected to the vertical gravitational field [6]. Other methods were later suggested in order to improve the samples crystallinity degree or to easier organize higher diameter particles. Electrophoresis is a growth assisted by the application of electric fields that try to compensate the gravitacional force and so decrease or increase the sedimentation rate [7]. Park *et al.* reported on the crystalization confined between parallel plates [8]. Moreover, the crystallization in patterned surfaces was shown to be useful for controling the shape, size, and orientation of opal crystals [9]. Related to that, nanorobotic manipulation of microspheres was used for producing PCs in the diamond structure [10]. Otherwise, spin coating [11] or shear-induce organization [12] may be used when large covered areas are required. Eventually, the mainstream fabrication method of opals is vertical deposition [13], that was the one adopted for the current thesis and will be described in more detail in Section 3.3.

In terms of applications, colloidal crystals have been applied for example as mechanochromic [14] or thermochromic [15] materials, in energy conversion [16] or as electrodes in Li batteries [17], in cell culture aiming at tissue regeneration [18] and naturally, in photonics [19].

1.2 Diffusive materials

Traditionally, deffects in PCs were regarded as important flaws, limiting the ideal performance of the materials. Notwidthstanding, scientists soon noted that random materials may also present many interesting properties and may lead to new physical phenomena with not only academic relevance, but with technological potential. In non-absorbing random media, light propagation

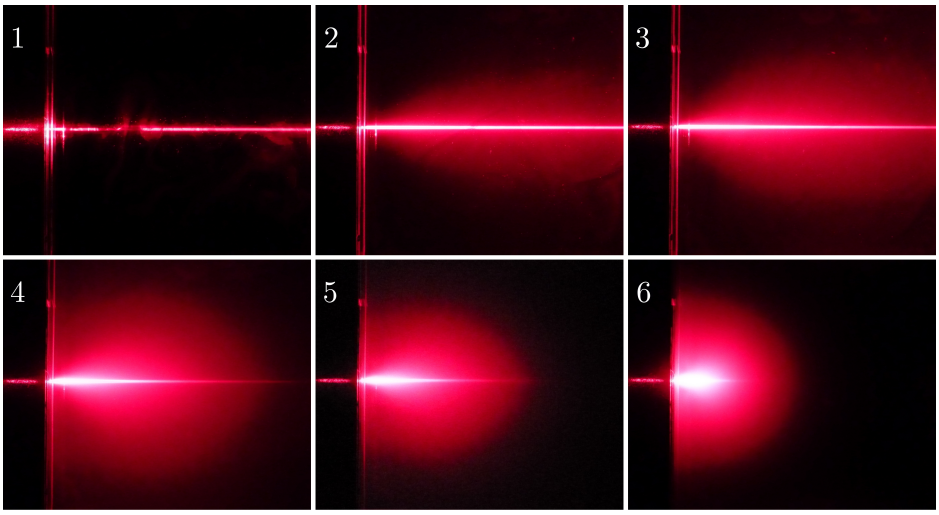

Figure 1.5: A laser beam crossing an homogeneous medium (water) presents balistic transport. As more and more drops of milk are added to the initial homogenous medium, a colloid is produced and the transport of light changes to diffusive. At a high enough concentration of colloid, the balistic transport is not observed anymore.

is dictated essentially by scattering. One can easily appreciate how light changes from a balistic transport regime to a diffusive one, by observing the behavior of a laser interacting with suspensions of milk in water at increasing concentrations (Figure 1.5). The figure shows successive images of a homemade experience using simply a laser pointer, and a water bath to which milk was added drop-by-drop. For water only, propagation is rectilinear and the laser beam can be seen only due to scattering by small inhomogenities. As milk is added, a colloid is produced and scattering from small lipidic droplets occurs. A diffusive halo surronding the original beam emerges. As the colloid becomes more and more concentrated, one observes that the balistic propagation is shortened and the diffusive halo also penetrates less and less into the colloid. In the next section, we will address single scattering of light, which is the basis for understanding diffusive transport.

1.2.1 Single light scattering

When light encounters an inhomogenity in some medium (generally referred to as a particle in what follows), it is known from experimental evidence that part of the wavefront will proceed unperturbed while other part will be diffused into other directions. This interaction is denoted as a scattering event

and the amount of angular distribution of the light scattered depends on the shape, size and materials constituting the particle. If only the wavevector direction $\mathbf{k}$ of the incident wave is changed but not its frequency, the process is denoted as elastic scattering. A scattering event may be expressed by the equation

$$\psi_{sc}(\mathbf{r}) = \mathbf{S}\,\psi_0(\mathbf{r}), \tag{1.5}$$

where $\mathbf{S}$ is the so called scattering matrix which relates an incoming state $\psi_0(\mathbf{r})$ to an outgoing one $\psi_{sc}(\mathbf{r})$, far away from the interaction potential. Thus $\mathbf{S}$ describes the process asymptotically. It is a common practise to express the scattered wave in the far field, as a superposition of outgoing spherical waves of the form

$$\Psi(\mathbf{r}) = \mathbf{s}(\mathbf{k_i}, \mathbf{k_f})\frac{e^{i\mathbf{k_f}\cdot\mathbf{r}}}{r}, \tag{1.6}$$

$\mathbf{s}(\mathbf{k_i}, \mathbf{k_f})$ being the scattering amplitude that depends on $\mathbf{k_i}$, the incident wavevector, and $\mathbf{k_f}$, the scattered one (with $|\mathbf{k_f}| = |\mathbf{k_i}| = k$). Usually, the scattering amplitude contains all the information of the scattering process but it is not experimentally accessible. This is the reason why in general it is preferable to treat the problem in terms of intensities, which are the measurable quantities. For spherical particles, the scattered intensity (energy flow per unit area) may be written as

$$I_{scatt} = \frac{d\sigma(\theta,\phi)}{d\Omega} I_0 = \frac{\sum_i |s_i(\theta,\phi)|^2}{2k^2 r^2} I_0, \tag{1.7}$$

where I_0 is the incident intensity and $d\sigma(\theta,\phi)/d\Omega$ is the differential scattering cross section. This magnitude is of extreme importance because it quantifies the normalized intensity scattered in the solid angle $d\Omega$ - it provides the time averaged power radiated by the scatter in a direction defined by the angles θ and ϕ, in a given polarization state, per unit solid angle and unit incident flux. From Equation 1.7 one may verify that the differential cross section relates to the scattering amplitude as

$$\frac{d\sigma(\theta,\phi)}{d\Omega} = \frac{\sum_i |s_i(\theta,\phi)|^2}{2k^2}\,. \tag{1.8}$$

The total probability for a scattering event to take place corresponds to the integrated differential scattering cross-section. This means that

$$\sigma = \int \frac{d\sigma(\theta,\phi)}{d\Omega}\, d\Omega = \frac{1}{2k^2}\int \sum_i |s_i(\theta,\phi)|^2 d\Omega\,. \tag{1.9}$$

The behavior of light is related not only to the total scattering cross section of the scatter but also to the concentration of scatters in the medium,

if they are all equal. If the medium is diluted enough or thin enough so that only one scattering event occurs, this is denoted as the single scattering regime.

1.2.2 Multiple light scattering

Contrary to that exposed in the previous section, if a medium is thick, light will suffer several processes of scattering, before abandoning the material. In this case, it is useful to define the average distance that it travels between scattering events, the so named scattering mean free path (ℓ_s). For diluted media, this parameter is related to σ and to the density of scatters in the medium (n_p) as

$$\ell_s = \frac{1}{n_p\,\sigma}\,. \tag{1.10}$$

In principle, this formalism is only applicable to scatters which possess no internal degrees of freedom or geometrical resonances (point-like scatters). Surprisingly, it may provide a very good approximation for the modelling of resonant media composed of Mie particles [20].

Going into a little more detail, the light propagation in random media, subjected to scattering, is contained in Maxwell's equations. Nevertheless, when the number of scattering centers is high, the solution of the equations is of high complexity and it is easier to tackle the problem from the point of view of a radiative transfer equation, neglecting phase and interference effects. More specifically, the diffusion approximation, which requires that $\lambda \ll \ell_s \ll L$, is commonly used, L being the sample size. It is reasonable that the scattering probability is the same at each point of the sample. Therefore one may write the probability that a photon propagates a distance r inside the medium, before suffering a scattering event, as $P(r) \sim \exp(-r/\ell_s)$. This argument justifies that, in such a medium, the transport of balistic radiation is thus governed by the Lambert-Beer law

$$I(\mathbf{r}) = I(0)e^{-\mathbf{r}/\ell_s}\,. \tag{1.11}$$

On the other hand, a diffusion equation describes the propagation of scattered light:

$$\frac{\partial I(\mathbf{r},t)}{\partial t} = \mathcal{D}\nabla^2 I(\mathbf{r},t) - \frac{\upsilon}{\ell_\alpha} I(\mathbf{r},t) + S(\mathbf{r},t) \tag{1.12}$$

where $\mathcal{D}$ is the diffusion constant, υ is the velocity of energy transport, ℓ_α is the absorption length (distance over which light is attenuated by a factor e, due to absorption) and $S(\mathbf{r},t)$ is the source term. The diffusion constant characterizes the rate of transport, meaning that the larger $\mathcal{D}$ is, the faster

the spread of light. Moreover, $\mathcal{D}$ can be expressed as a function of v and another parameter named the transport mean free path (ℓ_t) as

$$\mathcal{D} = \frac{1}{3} v \, \ell_t \, . \tag{1.13}$$

The transport mean free path is interpreted as the average length after which the scattered photon loses memory of its previous propagation direction. It is related to ℓ_s as

$$\ell_t = \frac{\ell_s}{1 - \langle \cos\theta \rangle} \, . \tag{1.14}$$

For isotropic scattering, $\ell_t = \ell_s$ although if the differential scattering cross-section is strongly dependent on θ, both quantities may differ by orders of magnitude.

The diffusion equation can be solved analytically in several situations. Although we will not get into further details, it is worth noting that, for a slablike geometry and in the absence of absorption, a stationary solution may be found, from which the total transmission of diffused light (integrated over all angles) can be approximated as

$$T(L, \lambda) \propto \frac{\ell_t}{L} \, . \tag{1.15}$$

1.3 Emission in photonic media

A full treatment of the light/matter interaction requires the complete description provided by the quantum theory, meaning that both matter and radiation should be quantized. Nevertheless, in order to simplify the problem, it is frequent to make the assumption that only matter is discrete and interacts with light, that is regarded as a classical field. In this picture, it is also useful to consider the two energy levels scheme for the atom or molecule composing the material (Figure 1.6). The level 1 is the ground state while 2 is the excited state, with respective energies E_1 and E_2. A photon with energy $h\nu = E_2 - E_1$, where h is Planck constant, may be absorbed leading the atom to the excited state (Figure 1.6a). Eventually, by coupling to vaccum fluctuations, it will tend to decay and radiate the absorbed energy. One of the possible ways to do so is the spontaneous emission, that is characterized by the emission of a photon with energy $h\nu$. Contrarily, if the atom, already in the excited state, is perturbed by a photon having the same energy $h\nu$, it may decay to the ground state with the emission of a second photon with energy and phase equal to the incident one. This process is known as stimulated emission and is in the basis of LASER action, which is an accronym referring to light amplification by stimulated emission of radiation.

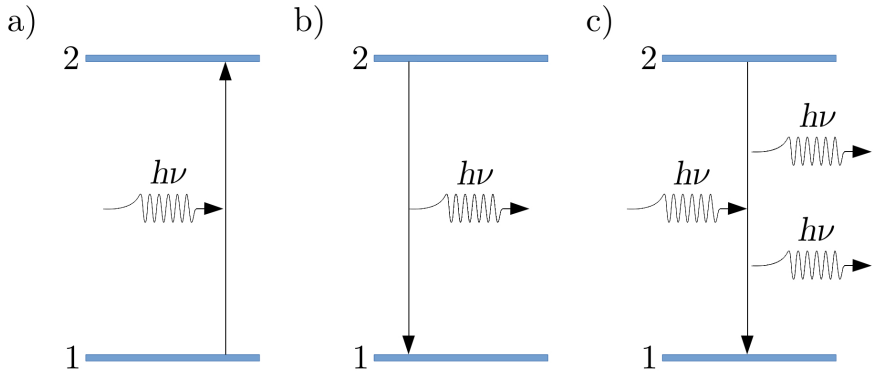

Figure 1.6: Two energy levels scheme to describe light/matter interaction. When a photon interacts with an atom, the phenomenon of a) absorption, b) spontaneous emission and c) stimulated emission may take place.

1.3.1 Amplified spontaneous emission

In an active medium (a medium with internal electronic states as described above, able to sustain optical gain), if the pump is enough to populate extensively the upper energy level, amplified spontaneous emission (ASE) may take place [21]. Thus, ASE is observed when spontaneously emitted photons are amplified, while propagating in the excited region, but in the absence of a resonant cavity that selects the resonant mode of oscillation - ASE may be considered as light amplification without mode selection.

To some degree, ASE has similar properties to laser action such as directionality, a narrower bandwidth than spontaneous emission (because of the higher gain experienced by frequencies near the maximum of the gain curve), it shows a threshold behavior and it can be quite intense. Additionally, it has some spatial and temporal coherence, although to a much less extent than laser action.

The ASE is characterized by a parameter known as the optical gain lenght, expressed in units of cm^{-1}, that is basically the distance that light must travel in order to be amplified by a factor e. This parameter may be determined for example with the variable stripe length method [22].

In order to accomplish true laser light, a resonant cavity must be used to select the oscillating mode of amplification. Different strategies may be considered, the most common one being to place the active medium inside a cavity composed of two mirrors. The distributed feedback may be also provided by PCs or scattering in the active medium itself. These approaches will be discussed briefly in the following sections.

1.3.2 Light emission in photonic crystals

The control of spontaneous emission is of utmost importance in photonics research and technology [2]. By engineering the local density of states (LDOS) in some medium, it is possible to influence its light transport properties [1]. In fact, it is well-known from Fermi golden rule that the radiative rate $\Gamma_{2\to1}$ of spontaneous emission is expressed by

$$\Gamma_{2\to1}(\omega) = \frac{2\pi}{\hbar}|\langle 1|H|2\rangle|^2 D(\omega), \tag{1.16}$$

$\langle 1|H|2\rangle$ being the matrix element of the perturbation (H) between the final and initial states and $D(\omega)$ the photon density of states to which light can couple. For free space, it can be shown to be [23]

$$D(\omega) = \frac{w^2}{\pi^2 c^3}\,, \tag{1.17}$$

but for material systems it may become considerably different. One possible effective route to the manipulation of the LDOS is to impose some periodicity in the dielectric constant (and consequently in the refractive index) of the material [24]. Further, the typical pitch of the modulation must be of the order of magnitude of the wavelength. This is the groundwork of PCs such as those presented in Section 1.1.

In comparison to the corresponding effective media (same effective refractice index n_{eff} but no periodicity), PCs conserve the total spectral number of states [25]. This implies that if the LDOS is reduced in some frequency region, due to the presence of a PBG, it must be enhanced in a distinct region. In PCs, the LDOS suppression takes place at PBG centers and its enhancement at PBG borders. Moreover, the increase of the available number of modes in a gap border is associated with a decrease in the group velocity of the corresponding modes. This is the mechanism which promotes the interaction of radiation and matter and allows either the spontaneous emission inhibition of an embedded emitter in a PC (when its characteristic transition is tuned with the PBG center) or spontaneous emission enhancement (when the transition is tuned with a PBG border).

Due to the previously discussed, PCs are promising for constructing photonic devices such as efficient light sources, particularly more compact or low-threshold lasers. In the last decades, there have been countless works on this field. To cite some examples, Nishijima *et al.* reported laser action from dye solutions infiltrated into silica inverse opals (IOs), due to a mechanism of gain distributed feedback [26]. Furumi also discussed laser emission of organic dyes, tuned with the gap border of PCs [27]. Moreover, the emission

may be spectrally tuned by applying mechanical stress. Interestingly, Garcia *et al.* reported on UV lasing in both ZnO PCs and disordered structures and furthermore, the transition between a Bloch to a random laser [28].

1.3.3 Light emission in random media

Contrary to conventional lasers in which the feedback mechanism is ensured by an optical cavity or to Bloch lasers, discussed in the previous section, in random lasers (RLs) it is provided by multiple scattering [29]. RLs were first proposed in 1966 as a possible strategy to achieved more robust lasers with respect to frequency [30]. A very comprehensive review of this phenomenon was provided by Cao [31].

Laser action in such systems is determined by the gain length ℓ_g (length over which the intensity is amplified by a factor e) and the amplification length ℓ_{amp}, which is defined as the root mean square average distance between the beginning and the ending point for paths of length ℓ_g. In a 3D system, they are related as

$$\ell_{amp} = \sqrt{\frac{\ell_t \ell_g}{3}}. \tag{1.18}$$

There are three possible regimes for light transport in a random medium, which affect the emission and lasing behavior, namely a) ballistic regime, $L \leqslant \ell_t$, b) the diffusive regime, $L \gg \ell_t \gg \lambda$, and c) the localization regime, $k_e \ell_s \simeq 1$ (k_e being the effective wavevector in the random medium). In the case of the diffusive regime, amplification may be taken into account in the diffusion equation, thus expression 1.12 would be re-written as

$$\frac{\partial I(\mathbf{r},t)}{\partial t} = \mathcal{D}\nabla^2 I(\mathbf{r},t) - \frac{\upsilon}{\ell_\alpha} I(\mathbf{r},t) + \frac{\upsilon}{\ell_g} I(\mathbf{r},t) + S(\mathbf{r},t)\,. \tag{1.19}$$

RLs have been commonly used in the development of ultra-compact lasers [32] or to achieve multicolor emission over the whole visible spectrum [33]. Additionally, RLs can be tailored to present characteristics such as high radiance and low spatial coherence, which are most desirable for illumination in applications such as speckle-free microscopy [34]. Stimulated emission has been observed in diverse diffusive platforms such as semiconductor powders [35], colloidal suspensions [36], paper-based devices [37] or polymers [38,39]. Compared to other systems, polymers possess notable advantages [40], for instance, a typically low fabrication cost, wide-range tunable properties by appropriately designing their syntheses, amenability for the production of mechanically flexible components, and industrial processability.

In recent years a new type of random material was proposed, named photonic glass [41]. These are composed by monodisperse Mie scatters (just like colloidal PCs), although in this case the spheres are arranged in a disordered way. Transport properties of these materials present resonant behavior and, by making use of those resonances, it is possible to tune the lasing frequency of some emitter, in case optical gain is introduced in the material. In this way, photonic glasses allowed the observation of resonant random lasing [42].

1.4 Shape memory polymers

Technological applications increasingly demand materials with sophisticated features and improved functionalities. In this context, multifunctional materials are especially attractive as they are often capable of responding to different physical, chemical and/or biological stimuli. A particularly useful property that has been incorporated into multifunctional materials is the shape-memory effect (SME), which was first identified in a gold-cadmium alloy [43] and later discovered in polymers (the so called shape-memory polymers, SMPs) [44, 45]. Compared to conventional shape-memory alloys, they represent a more efficient alternative, allow higher strains before rupture, are less expensive and easier to implement with high throughput. SMPs are able to switch from a temporary to a permanent shape in response to an external stimulus [46, 47]. This effect is exemplified in Figure 1.7. Slabs of polydiolcitrate polymer were cut in a predefined way (capital letters), thus acquiring their permanent shape (B1). The polymeric pieces were then subjected to a heat/stress/cool cycle in order to store the temporary shape (B2) and finally, after re-heating, the permanent shape was recovered (B3) [48].

In general, the SME is triggered by heat and arises due to chemical or physical switchings at the molecular level. This means that the flexibility of the polymeric chains is a function of temperature. Above the so called transition temperature (T_{trans}), the chain segments are flexible and therefore the polymer is in a rubber-like state that may be deformed. Below the thermal transition, the flexibility of the segments becomes totally or partially limited and so the elastomer becomes rigid. In the case of chemical switching, the change in flexibility is based on reversible covalent bonding while in the case of physical switching, intermolecular interactions drive the SME. As an example, polydiolcitrates, studied in this thesis, are composed of two seggregated domains: a crosslinked elastomeric network responsible for the permanent shape and non-crosslinked microdomains embedded in that matrix that undergo a phase transition (melting) at T_{trans}, that controls the switching.

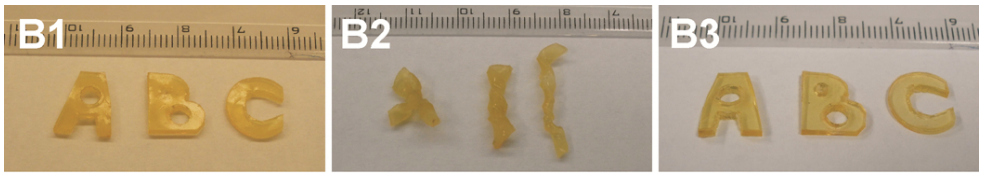

Figure 1.7: Illustration of the SME in polydiolcitrate polymers being B1) the permanent shape, B2) the temporary deformed shape and B3) the permanent restored shape. Adapted from [48].

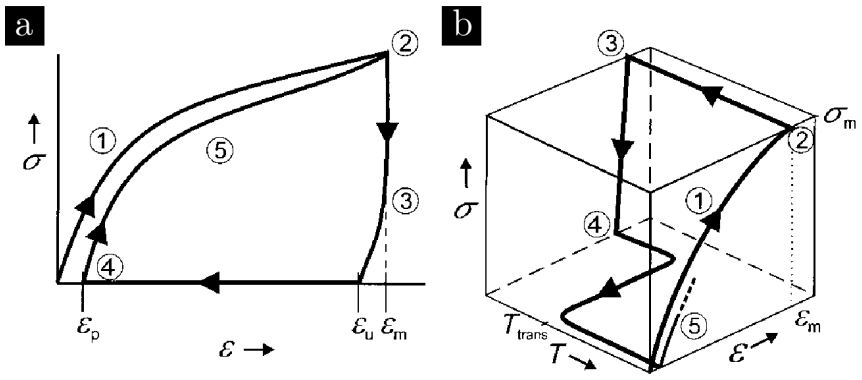

Figure 1.8: Scheme illustrating the two more typical protocols of thermomechanical programing: a) two-dimensional measurement and b) three-dimensional programming. Adapted from [46].

The SME is usually quantified by cyclic thermomechanical investigations [46]. The most typical test protocols are presented in Figure 1.8. The first one (Figure 1.8a) is denoted as a two-dimensional measurement as it is presented in the form of a stress/strain cycle ($\sigma(\varepsilon)$). On their turn, three-dimensional thermomechanical measurements (Figure 1.8b) have the advantage that T_{trans} can be straightforwardly determined, at the same time that stress and strain are.

Although heat is typically responsible for directly triggering the SME [49], recent advances have identified other possible indirect mechanisms such as electrical stimulation [50] or alternating magnetic field excitation [51]. For achieving such effects, specific fillers able to absorb energy under excitation and increase temperature are usually incorporated to the original shape memory polymeric matrix. Interestingly, there are also reports describing heat-independent light-activated SME [52, 53]. In terms of chemical composition, SMPs made of acrylamides [54], caprolactones [55], and polyurethanes [56] have been explored as stimuli-sensitive polymers with advanced function-

alities [57]. They are suitable for applications as diverse as biomedical devices [58], packaging [59], temperature sensors [60], self-deployable sun-sails or microfoldable vehicles [61,62]. Recently, SMPs are also drawing an increasing interest for photonics [63].

1.5 Outline of this thesis

This thesis is devoted to the development of advanced photonic materials and their potential implementation in multifunctional systems. It is divided in two main parts. The first one comprises Chapters 2 and 3 and regards the fabrication of PCs using conventional inorganic materials. The second part, comprising Chapter 4 and 5, relates to the exploration of SMPs for fabricating both periodically organized and diffusive media. Specifically, it is organized in the following chapters.

- Chapter 2 reports the fabrication and characterization of two dimensional PCs, specifically inverse monolayers of silica. A fabrication protocol introducing some novelties is presented, which allows to grow composite monolayers in a one step method and porous membranes, by sacrificing one of the components. This work is partially extended in an attempt towards the fabrication of porous membranes of silicon.

- Chapter 3 discusses the growth of three dimensional PCs by self-assembly methods. Composite opals are grown by vertical deposition and co-assembly techniques and several doping strategies with Rare Earth elements are tested. The aim of this work is to search for photonic effects, in the infrared region of Er^{3+} photoluminescence, induced by the presence of a pseudogap in silica IOs or by a full PBG in silicon ones.

- Chapter 4 describes a replica molding procedure adequate to imprint 2D gratings in the surface of SMPs, by using self-assembled colloidal monolayers as templates. The obtained crystals are characterized with different techniques to assess their structural and optical properties. Their applicability in new multifunctional photonic devices with programmable and self-healing capabilities is ascertained.

- Chapter 5 explores the possibility of using SMPs to fabricate new nanocomposites containing titania nanoparticles that may perform as functional photonic white paints. Furthermore, their potential use as shape programmable active media is verified by doping them with organic dyes. Systematic photoluminescence studies are performed.

Part I

Fabrication of 2D and 3D photonic crystals by self-assembly methods

2

Two-dimensional PCs as porous membranes

In this chapter, the fabrication of inverse colloidal monolayers is described. In a first step we demonstrate that, for producing composites of polystyrene spheres embedded in a silica matrix, it is possible to conjugate co-assembly with a cell confined growth, while profiting from the advantages of both techniques. The inverse silica monolayers are obtained by thermal calcination of those composites. Results show that extense regions of good quality porous membranes can be obtained with this procedure. Additionally, these membranes may are subjected to magnesiothermic reduction in order to test for replication in silicon.

2.1 Introduction

The pursuit of materials with uncommon optical properties has increadibly boosted the research effort during the last decades, in the photonics community. As far as the control of the radiation/matter interaction is concerned and consequently the manipulation of light, two-dimensional (2D) photonic crystals (PCs) have proven to be strong candidates for such purposes, due to their high versatility. Among those, slablike crystals based on the packaging of dielectric spheres are perhaps the most straightforward to fabricate [64]. These systems can be implemented in applications such as filtering or waveguiding [65], microlens arrays [66], and hybrid photonic−plasmonic materials [67]. Additionally, they can play an extraordinary role as masks, in nanosphere lithography [68], or as templates for more complex colloidal structures [69–71]; they are very effective for the production of nanoparticles [72] and, from a fundamental point of view, they can be addressed by theoretical studies [73].

In order to accomplish this kind of 2D PCs, self-assembly techniques are the simplest and most widely used methodologies. The most widespread one is probably the vertical deposition method [13], starting from diluted colloidal suspensions. This technique relies on convective particle assembly and delivers crystals consisting of dielectric spheres, arranged in a hexagonal lattice. Nonetheless, polycrystalline domain structure is a major limitation of the method. Consequently, a number of publications have proposed refined processes of convective particle assembly and reported on the influence of different growth parameters on the quality of the monolayers [74, 75]. It was recently shown that, by controlling the geometry of the three-phase contact line at the meniscus of the suspension, one can achieve better quality monolayers than those obtained by vertical deposition, in particular, single domain ones, centimeters across [76]. This is achieved by confining the suspension in a wedge-shaped cell. The characteristic feature of this kind of evaporation cell is that it permits an almost rectilinear interface between the three phases involved during evaporation.

Despite the considerable interest that these 2D arrangements of spheres can raise, there is also a significant demand on the fabrication of the inverse structures, that is, membranes composed of nanobowls, nanopore arrays or interconnected air voids [77]. Inverse structures, based on colloidal crystal monolayers, might be used for the development of gas sensors [78] and superhydrophobic surfaces [79], evaporation masks [80], templates for cell growth [81], or protein self-assembly [82]; for the study of photoluminescence [83]; or even for the enhancement of magnetic properties of thin films [84]. They have been produced with diverse compositions such as inorganic materials [79], oxides [85, 86], semiconductors [87], metals [88], or polymers [53, 89]. With regard to fabrication, the inverse monolayers have been achieved by infiltration with techniques such as electron beam evaporation [90], doctor blade technique [91], solution/sol-dipping, or electrodeposition [92]. Additionally, gas phase deposition techniques can also be used for the infiltration, with additional advantages. They permit a very good degree of conformality of the deposited material and also fine-tuning of the film thickness [93].

Regarding three dimensional (3D) crystals, recent experiments pointed out that good-quality, crack-free, inverse opals could be fabricated in a two-step method using co-assembly [94] (this topic will be further detailed in Chapter 3). The obtained crystals presented a high degree of order, over length scales of centimeters. The mainstream method to produce inverse opals is essentially (a) growth of a bare opal of sacrificial material, (b) infiltration with the desired material, and (c) selective removal of the sacrificial one. Using the new approach (coassembly), the composite is obtained in a sin-

gle step in which a chemical precursor of the background material is added to the spheres suspension. Therefore, it deposits in the spheres interstices simultaneously to the particle assembly. Subsequently, using calcination or plasma etching, the sacrificial spheres are removed and the inverse opal is obtained. Moreover, the authors show that direct conversion into other materials (silicon and titania) is possible using shape-preserving gas/solid displacement reactions [94].

In this work, we test the possibility of fabricating silicon oxide inverse monolayers using a sol-gel approach and combining the wedge-shaped cell growth, on the one hand, with coassembly on the other. By adopting this procedure, one might benefit from the advantages that both techniques permit. In comparison with similar tests, previously carried out by other groups, our approach has the advantage of achieving the composite (PS spheres embedded in silica matrix) in one single step, as opposed to work by Li *et. al.* [95], which relies on sol-dipping, and also of increasing the effective macroscopic area of the final monolayers. In these lines, Lu and co-workers reported a typical ordered area of 100 μm^2 [96], while we were able to obtain monodomain areas around 1000 μm^2.

2.2 Samples fabrication

The PS spheres used in this work were commercially acquired (Thermo Scientific). Two diameters were compared, $\phi = 430$ and $\phi = 520$ nm, with polydispersity below 3%, in both cases. The monolayers were grown on glass substrates using the wedge-shaped cell method. More details are provided in reference [74]. Briefly, the substrates were carefully cleaned in a detergent and water ultrasound bath. Then, they were rinsed with distilled water, dried under a nitrogen flux, and immersed in a hydrogen peroxide solution at 80°C for approximately 1 h. Afterwards, they were rinsed and dried once again. Finally, the wedge-shaped cells were assembled accordingly to the photo exhibited in Figure 2.1. The angle described between the substrate and the cover slide was 2°.

The concentration of spheres was kept constant in all the suspensions (100 μL of the commercial suspensions at 10 wt%, final concentration of $\approx$ 0.5 wt%). The silica precursor used was a mixture of ethanol, 0.1 M HCl in water, and tetraethylorthosilicate (TEOS) in the mass ratios of 1.5 : 1 : 1, stirred for 1 h - for convenience this mixture is referred to as TEOS throughout the text. Sets of crystals were fabricated varying the added volume of TEOS to the initial colloid from 20 to 120 μL. This corresponds to a concentration range from 1 to 6 vol%. The total volume of the suspensions prepared was 2 mL for

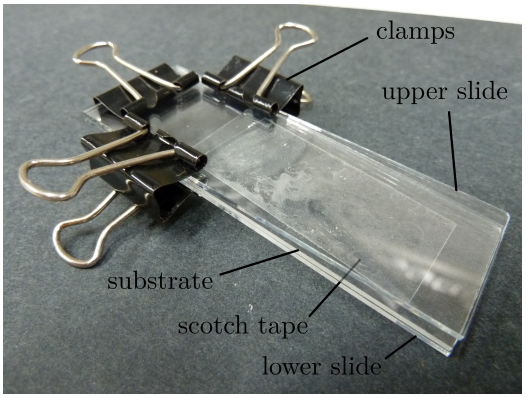

Figure 2.1: A schematic illustration of the wedge-shaped cell used for the fabrication of the composite monolayers. Clamps are set in order to lock all the components in position. We note that the scotch tape is placed between the lower slide and the substrate.

all cases. The suspensions were prepared in clean glass vials. First, distilled water (18.2 MΩ) was poured into them, the respective volume of precursor was added, and lastly the spheres. In order to homogenize the mixtures, the vials were briefly immersed in an ultrasound bath. Finally, a volume of 100 μL of the suspension was inserted into the wedge cell with the aid of a micropipette. The cells were placed in a climatic chamber over a polymeric platform in order to minimize vibration. The chosen temperature was 20°C and the relative humidity 90%. Typically, four replicas were prepared for each concentration in order to minimize the intrinsic variability of the fabrication process. The samples were withdrawn after approximately 24 h.

At a later stage, the samples were treated in order to remove the polymer of the composite and obtain the inverse matrix. They were subjected to calcination in a tubular furnace using the program shown in Figure 2.2. First, the temperature was raised from room temperature to 90°C at a rate of 1°C/min. This ramp was followed by a plateau of 3 h at 90°C. Afterward, the sample was heated until a temperature of 450°C was reached, at a rate of 1°C/min. The monolayers were maintained at this temperature for 8 h. Finally, cooling was performed at 5°C/min until the temperature of 30°C was reached. Due to thermal inertia of the furnace, this rate was not correctly fulfilled and, particularly at low temperatures, the cooling rate was determined by the natural cooling rate of the furnace (grey area of the figure).

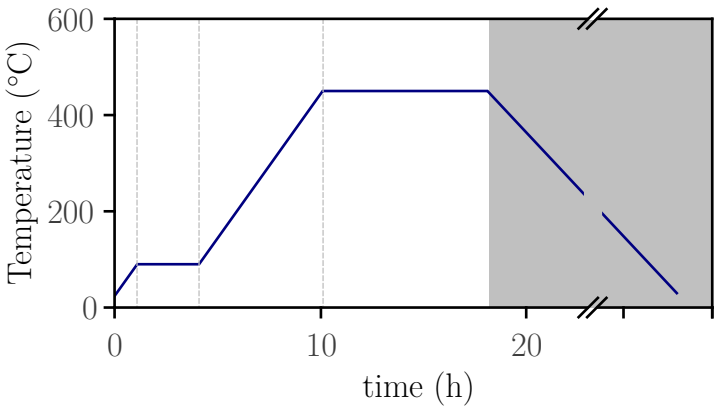

Figure 2.2: Temperature program, as a function of time, used for the calcination of the composites in order to remove the sacrificial PS spheres.

2.3 Composite monolayers

As stated in the previous section, we propose a one step method for the fabrication of the composite monolayers, based on co-assembly. This fabrication scheme permits the straightforward achievement of an opened topology, which to be obtained for example by CVD infiltration, would require an additional etching step. This is a drawback, as expensive techniques like reactive ion etching are required to carry out etching of the top surface. In what follows, the systematic analysis of the composite is reported and then the inverse monolayer is presented.

A common feature was observed in all the monolayers grown by coassembly confined in a wedge-shaped cell. They typically exhibit three different regimes of growth, as can be appreciated in Figure 2.3, which shows examples of optical microscopy photographs. The first regime (Figure 2.3a) occurred mainly at the beginning of the process, but sometimes it also extended along the growth direction (especially near the borders of the confinement cell). In this regime, the samples presented poor quality, with disorder, small domains, and even the formation of multilayers. After some time elapsed, the growth stabilized and a good-quality composite monolayer started to develop; this is the second regime, depicted in Figure 2.3b. In this region (as in the previous one), the infiltration with silica took place. At some point, the condensation reaction was terminated as TEOS ran out and bare monolayer grew from there on; this is the third regime, as observed in Figure 2.3d. A marked frontier separating the last two regions was observed (Figure 2.3c). Comparing regions b and c of the figure, it is seen that the amount of defects that appear in the bare region, typically as small islands of two or three

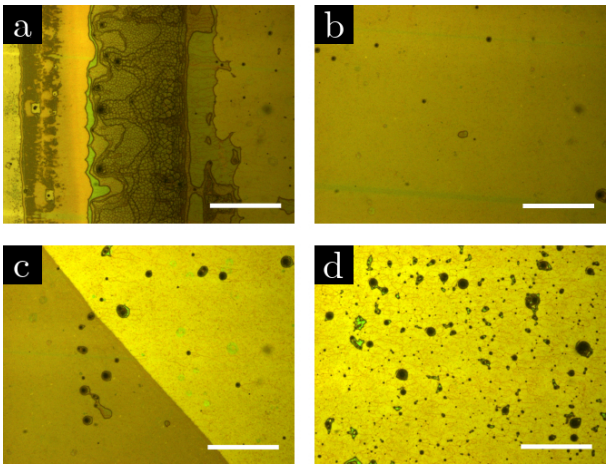

Figure 2.3: Three growth regimes can be identified by observing the samples at the optical microscope: a) beginning of the growth exhibiting poor quality, b) silica infiltrated monolayer, and d) bare monolayer. The transition between the two last regions, shown in figure c, is significantly abrupt. In this example, the sample grown with spheres of diameter $\phi = 430$ nm and [TEOS] = 1.5 vol% is grown. The scale bar corresponds to 250 μm in all cases.

layers, was larger than in the composite region. The defects are identified as darker spots standing out from the bright background. That observation was a general feature of the samples studied.

To the naked eye, the crystals grown with spheres of $\phi = 430$ nm typically started to nucleate nearer the borders of the substrate. For almost all the samples a V shape was observed. As the growth proceeded, those regions expanded toward the center and joined at some point. After this, the material grew as a continuous region occupying all substrate width. Near the borders the samples exhibited intense colors and iridescence while the center region usually presented a milkier aspect that is characteristic of disorder. On the other hand, very good quality and large regions were obtained for the samples grown with spheres of $\phi = 520$ nm. In these, the three regimes mentioned above were also observed, but to the naked eye, the crystal developed along all the width of the substrate, right from the beginning. As expected, the infiltrated areas were slightly more transparent due to the lower refraction index contrast and thus to the lower scattering efficiency.

A quantitative analysis of the above-mentioned aspects is summarized in Figure 2.4. The data points were collected by hand-drawing the contours of the regions of interest, digitalizing them, and then using a software to calculate their respective areas. The analysis showed that the percentage of good-quality infiltrated area of the sample with respect to the total initial

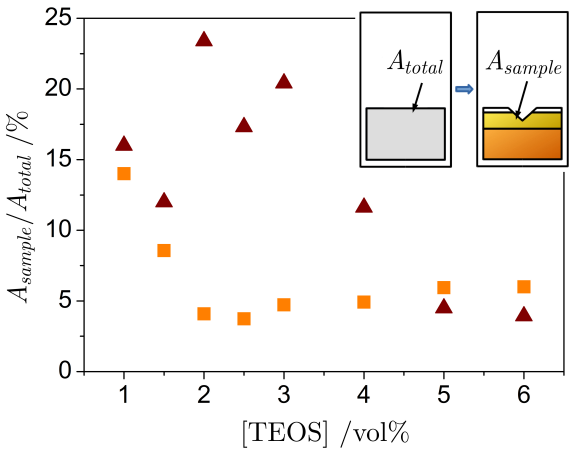

Figure 2.4: Quantitative analysis of the good-quality infiltrated area (A_{sample}) with respect to the total area susceptible of growing (A_{total}), versus concentration of TEOS. A_{total} is the area initially occupied by the liquid colloid. Squares (triangles) express results for samples grown with spheres of diameter 430 (520) nm. The inset shows the definition of A_{sample} and A_{total}.

area covered by the colloid (2.6×1.5 cm^2) was on the order of 15% in the case of the samples grown with $\phi = 430$ nm spheres and [TEOS] = 1.0 vol%. Low precursor concentrations favored the extension of the infiltration as for [TEOS] higher than 2 vol% the area extension oscillated around 5%. In the case of the samples grown with spheres of $\phi = 520$ nm, the best result was obtained for [TEOS] = 2.0 vol% with an infiltrated area on the order of 25%. In general, for most TEOS concentrations studied, these samples performed better than their low diameter sphere counterparts, except for [TEOS] above 5.0 vol%. Possibly, the parameters that might induce these significant differences are the angle described by the wedge-cell and the type of spheres or surfactant present in the commercial suspension. In fact, some preliminary experiments have shown that the angle of the cell should be slightly tuned according to the diameter of spheres used. Nevertheless, a study of the quality of the samples as a function of the referred angle was out of the scope of the present thesis. Regarding the type of stabilizers of the commercial suspensions, it is possible that they have an effect on the colloid. This could not be ascertained, as details about the commercial colloids are proprietary information.

The structural characterization of the samples was accomplished with a FEI NovaNano SEM 230 field emission electron microscope. This analysis permitted us to corroborate that the differences between the two kinds of regions observed in each sample were due to the presence or absence of silica.

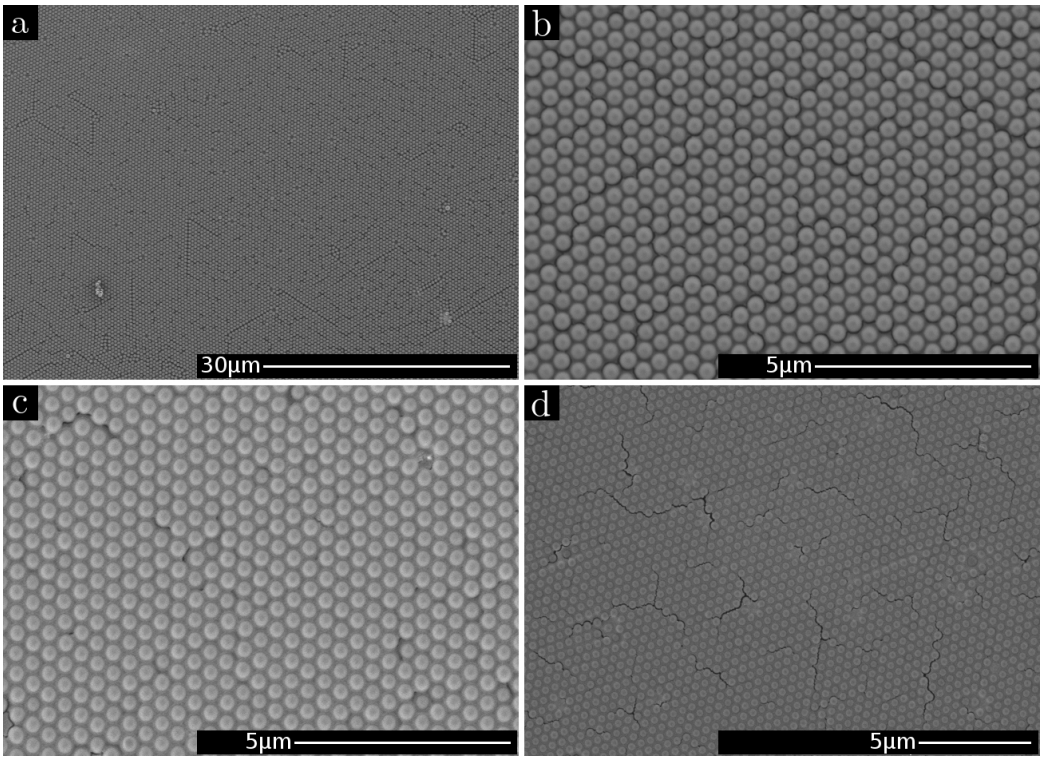

Figure 2.5: Representative SEM images of samples fabricated with spheres of ϕ = 430 nm. The concentration of TEOS used was a) and b) 1.0 vol %, c) 2.5 vol %, and d) 4.0 vol %. The large domains obtained and the changes in the infiltration degree are noteworthy.

It showed that the areas corresponding to the mentioned second regime were formed of composite material (PS embedded in silica), while the areas corresponding to the third regime were not infiltrated (PS bare monolayer). Figure 2.5 shows representative SEM micrographs of the composite part of samples fabricated with spheres of 430 nm in diameter. In all cases, it was possible to observe a good degree of order and extensive monodomain regions. For example, Figure 2.5a illustrates a small piece of a much larger monodomain of approximately 8500 μm^2. The good quality of the samples was eventually perturbed by defects such as some spheres detached from the matrix, which originate cracks like those shown in Figure 2.5d, possibly during the drying process. Frequently, point defects such as missing spheres or slightly different diameter spheres and linear defects like dislocations are observed [74]. Nevertheless, the overall extension of monodomains is typically preserved. This degree of quality is representative and was also found for the samples grown with $\phi = 520$ nm spheres.

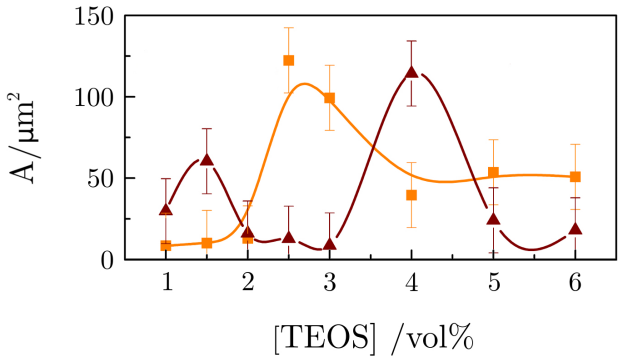

Figure 2.6: The average area of good-quality, crack-free areas, inside the larger monodomains of the composite monolayers. Squares (triangles) express the results for samples grown with spheres of diameter 430 (520) nm. The drawn curves simply intend to highlight the general tendency of the data and do not correspond to any theoretical fitting.

SEM showed that the single domains are typically very broad, of the order of 1000 μm^2. Nevertheless, perfect regions do not present such large areas. These were defined as smaller parts of the crystals which belong to the same monodomain, although they present cracks originated in the drying phase, as is exemplified in Figure 2.5d. Figure 2.6 shows a statistical analysis of the average area of these smaller crystallites. The areas were estimated with the help of a drawing software and averages were typically taken from 10 regions belonging to at least five images of different regions. Despite data dispersion, a clear quality improvement was observed for determined [TEOS]. Maxima are observed in both curves corresponding to the two diameters studied. In both cases, the larger areas of crystallites achieved were of the order of 120 μm^2. The maximum area was obtained for [TEOS] = 2.5 vol % in the case of using 430 nm spheres, while for samples produced with larger spheres, the maximum was observed for [TEOS] = 4.0 vol%. The fact that there was an optimal TEOS concentration is not surprising. If too low, it is not possible to reach a continuous silica film, filling in the interstices between spheres. On the contrary, if too high, the quantity of additional charge introduced in the colloid is significant and this induces rheological instability [97].

The most remarkable aspect resulting from the analysis of SEM images was the fact that the apparent diameter of the spheres (ϕ_{app}) - their diameter observed from a surface view - presented significant changes as the added quantity of TEOS in the starting suspension was increased. For the analysis

of the images, a complete infiltration was assumed meaning that the silica occupies the entire available volume in the spheres interstices, from $z = 0$ (location of the glass substrate) to $z = h$, which is the maximum thickness of the silica film - z being the coordinate normal to the substrate. It was further assumed that the infiltration surpassed the spheres equator ($h > \phi/2$). From simple geometrical considerations, it is possible to express h as a function of the measurable parameter ϕ_{app} as

$$h = \left(\frac{\phi}{2}\right) + \sqrt{\left(\frac{\phi}{2}\right)^2 - \left(\frac{\phi_{app}}{2}\right)^2}. \tag{2.1}$$

In this sense, a decrease in ϕ_{app} implies that h increases and vice versa. Therefore, the experimental observations suggested the hypothesis that it was possible to change the filling fraction (f) of the silica in the final inverse matrix by acting on the concentration of its precursor. The filling fraction is defined as

$$f = \frac{h}{\phi} - \frac{\pi h^2}{3\sqrt{3}a^2\phi}(3\phi - 2h), \tag{2.2}$$

where a is the lattice parameter. This hypothesis was supported by previous observations in similar systems, for which it was reported that it was possible to control the morphology of the grown inverse monolayer by controlling the concentration of the infiltrating precursor [85]. In order to carry this analysis further and ascertain the behavior of f, it is also necessary to account for a. For all samples, in the second growth regime, due to the presence of silica, it was verified that a was larger than the sphere diameter, implying that the material organized in cermet topology. On the contrary, in regions belonging to the third regime of growth (Figure 2.3d), apart from intrinsic defects, the structure assumed a close-packed form.

A systematic analysis of ϕ_{app}, a and f was carried out. The results are summarized in Figure 2.7. Concerning the samples produced with spheres of $\phi = 430$ nm, a linear fitting of the experimental data showed that ϕ_{app} decreased *c.a.* 11% and a increased approximately 2%, accompanying the increase of [TEOS] from 1 to 6 vol%. In the same range, the increase of the filling fraction was of the order of 5%. For the samples with spheres of $\phi = 520$ nm, an actual increase of *c.a.* 2% was observed in ϕ_{app} while the increase in a was of the order of 4%, thus implying a variation of f much less expressive - only an increase of 1% was determined. Although the mentioned linear fits exhibit the expected behavior, it is necessary to point out that, for both sets of samples, a monotonic increase of f was not evident. Care should be taken as the observed changes in f were of the order of magnitude of the experimental error. The error was estimated by applying the propagation equation to f

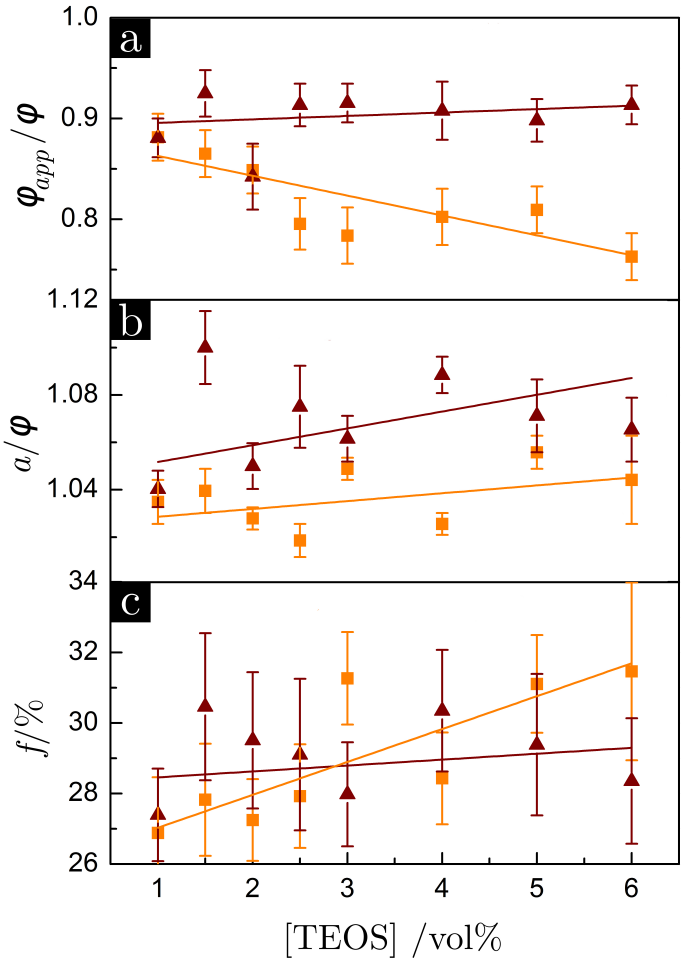

Figure 2.7: a) Normalized apparent diameter (ϕ_{app}), b) normalized lattice parameter (a) and c) filling fraction (f) as a function of TEOS concentration. With the apparent diameter and the lattice parameter one can extract the filling fraction of the silica. Squares (triangles) express the results for samples grown with spheres of diameter 430 (520) nm. The drawn curves correspond to linear fittings of the data points.

and assuming the standard deviation as the error of ϕ_{app} and a. Although the data were noisy, they suggested that, for low concentrations of the precursor, the degree of infiltration was higher in those samples fabricated with spheres of $\phi = 520$ nm. As the concentration of TEOS increased, that relation was inverted and the filling fraction became higher for the samples with $\phi = 430$ nm. The inversion occurred approximately for [TEOS] = 3.0 vol%.

2.4 Inverse silica monolayers

The second step of the inverse monolayers fabrication consisted of the sacrificial PS spheres removal. For this purpose, calcination and plasma etching were preliminary tested. It was verified that calcination led to similar results to oxygen plasma etching, and that being so, both processes introduced some amount of defects and cracks in the matrix. Calcination was the adopted treatment.

Figure 2.8 shows the aspect that the monolayers presented after calcination. These SEM images are examples of the samples fabricated with spheres of 430 nm of diameter and [TEOS] = 1.0, 2.0, and 3.0 vol %. Images taken in cross section, as exemplified in Figure 2.8a, confirmed that the interconnected 3D structure was preserved as expected and that the infiltration surpassed the equator of the spheres. The thickness h of the monolayer could be estimated by measuring the thickness observed in the image and correcting it with the tilt angle of the microscope stage. In this example, the thickness obtained was 260 nm. From low-magnification images, such as those presented in Figure 2.8b−d, the hexagonal pattern was clearly visible and large monodomain regions were preserved. The area of the exhibited monodomain in Figure 2.8b is ≈ 2900 μm^2, the one in Figure 2.8c is 2100 μm^2 and the one from Figure 2.8d is 2000 μm^2. While in Figure 2.8b some point defects which originate in the formation of the composite are observable, due to missing spheres or different size spheres, in Figure 2.8c all region presents minimum defects. In Figure 2.8d cracks can be observed that are associated with the drying step and posterior thermal treatment. It is probable that for high [TEOS] the grown silica is less porous, which gives rise to increasing mechanical tension during the removal of the spheres, and small cracks like the ones exhibited in Figure 2.5d increase in size. The insets in Figure 2.8b−d show the digital Fourier transform of the respective image and permit one to appreciate the 6-fold symmetry characteristic of the lattice, as individual points in the reciprocal space. This is a strong evidence of the good quality of the monolayers, even after calcination.

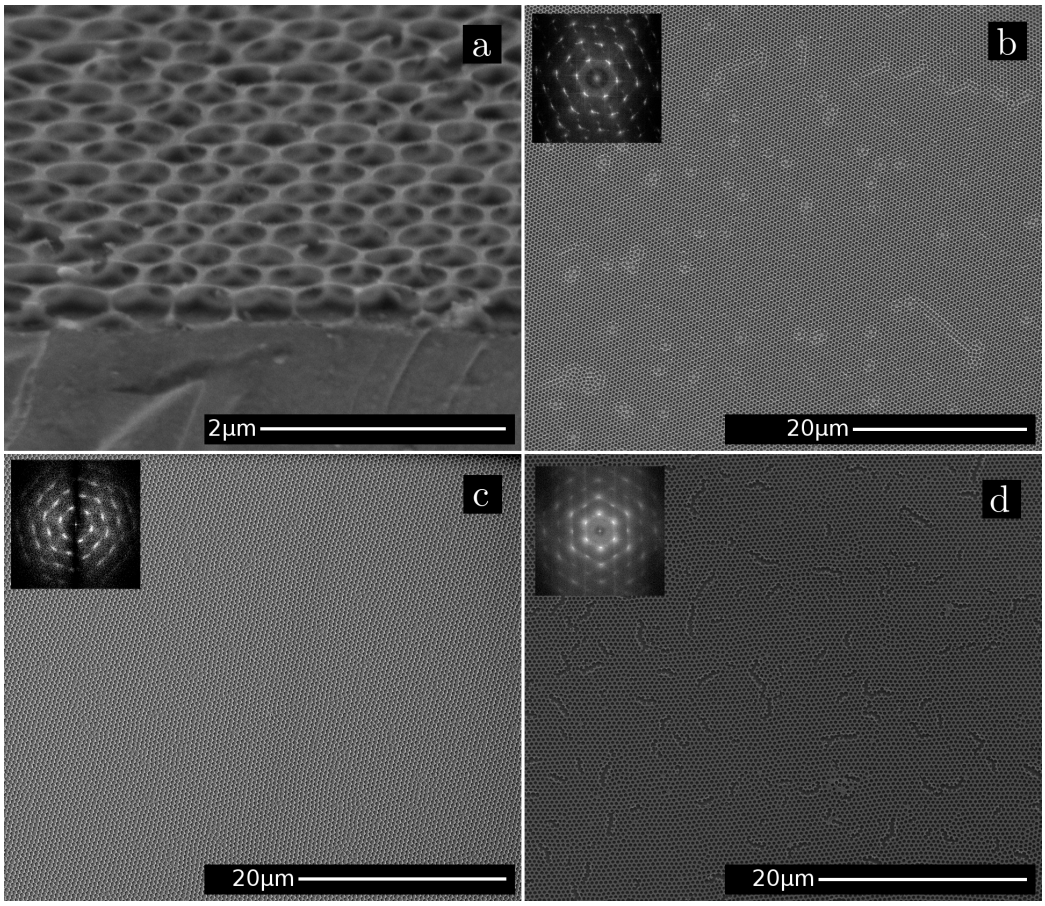

Figure 2.8: a) An example of a high-magnification SEM image of the inverse monolayer in cross section, with [TEOS] = 2.0 vol%. SEM images at low magnification of samples grown with b) [TEOS] = 1.0 vol%, c) [TEOS] = 2.0 vol%, and d) [TEOS] = 3.0 vol% - samples fabricated with spheres of 430 nm diameter. It is possible to appreciate good quality and wide domains after the thermal treatment. The insets of figures b, c, and d show the digital Fourier transform of the respective image.

2.5 Optical characterization

Using FIS, angle resolved reflectance spectra were investigated for our samples. A brief overview of the technique is provided in Appendix A. Although differences in the filling fraction of the composite could not be resolved for different concentrations of TEOS, the second and third regime of growth - composite and bare monolayer - were compared and analyzed in the framework of an effective medium model. The results are exhibited as gray scale

plots in Figure 2.9. This figure shows an example for the case of the monolayers produced with spheres of $\phi = 520$ nm.

Results are represented for increasing angles of incidence along the two high-symmetry directions in reciprocal space for a hexagonal lattice: ΓM and ΓK. In the plots corresponding to the experimental results of the bare crystal (Figure 2.9b), a number of modes appear as lines crossing at $\lambda \approx 650$ nm, at the Γ point. The dispersion of the different modes is clearly different for the two directions considered. In order to account for these results, we have employed an effective medium model [98]. In this approach, one considers a homogeneous medium having a real refractive index n_{eff}. The effect of the periodicity is introduced in two ways: folding the dispersion relation at the Brillouin zone edges (bands ΓM1, ΓM4) and taking into account the diffraction by different reciprocal lattice vectors (bands ΓM2, ΓM3, ΓK1−3). The outcome of this model assuming an $n_{eff} = 1.45$ is shown in Figure 2.9a. Here it is evident that the overall shape of the experimental dispersion relations is well-reproduced.

In order to get a good agreement between the theoretical bands and the experimental ones, a much higher effective refractive index had to be assumed than that expected from the effective medium approximation - 1.45 versus 1.35 - which would result from the weighted volume average of the two indices composing the monolayer, considering a filling fraction of PS of 60% and 40% of air. This can be explained by examining the spatial distribution of the total field intensity. The contributing modes correspond to guided modes of the monolayer, so it is shown that, in the system under study, the total field intensity becomes much more concentrated inside the spheres. For this reason, the actual refraction index the radiation feels is higher [98].

The broad gray bands in Figure 2.9a represent the first-order diffraction onset and the re-entrance in the detector [98]. They can also be observed in the measured spectra and the positions are in good agreement. Furthermore, this agreement is also verified in the case of the modes ΓK1, ΓK3, ΓM1, ΓM2, and ΓM3. The position of the ΓK2 mode is also well-predicted. In the collected spectra it is possible to observe another mode adjacent to it. Actually, it is verified that the ΓK2 branch corresponds to two modes whose degeneracy is lifted, as can be seen in the experimental measurement. Finally, concerning the ΓM4 mode, it is the least intense, as expected, but its slope, in the dispersion relation, is higher than expected.

The spectra of the composite were also measured and are presented in Figure 2.9c. The results are exemplified for the case of the sample fabricated with [TEOS] = 1.0 vol %. The signal-to-noise ratio was smaller and the reflectance of the sample droped to approximately half that of the previous bare monolayer. This was due to the decrease in the contrast between the

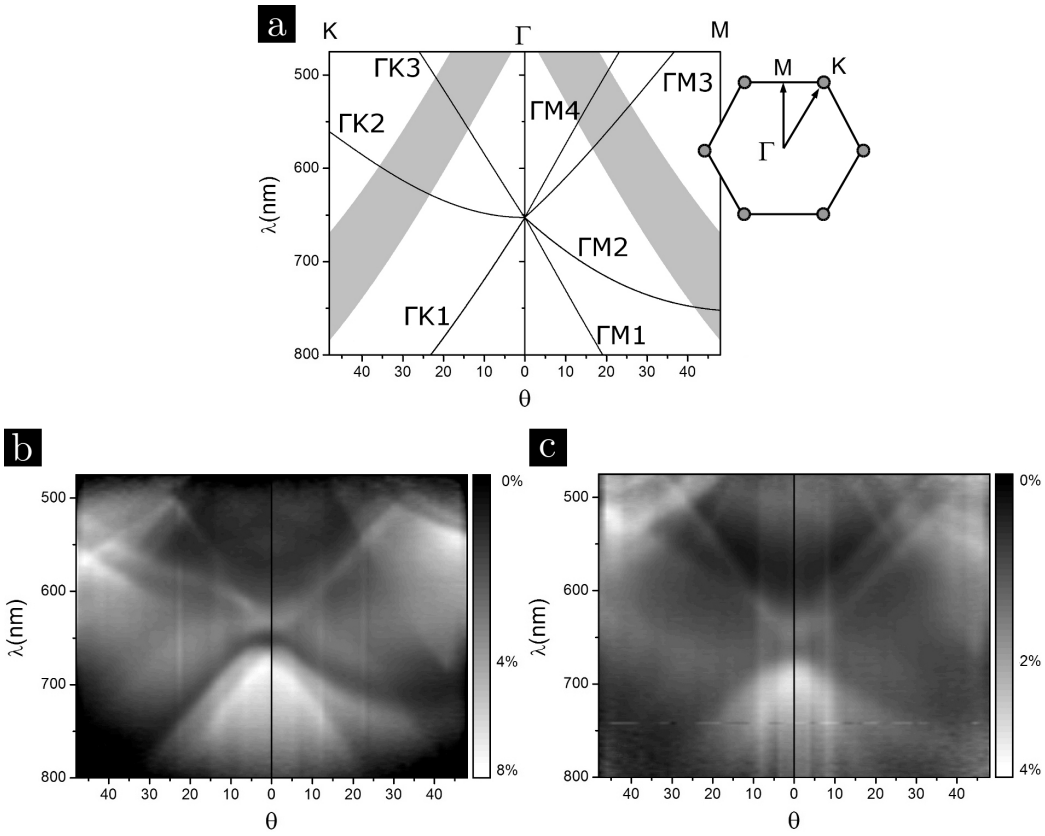

Figure 2.9: a) Theoretical dispersion relation of a bare monolayer of PS spheres. b) Experimental angle-resolved reflectance spectra resulting from Fourier image spectroscopy measurements of a bare monolayer and c) similar measurements for a composite membrane (ϕ = 520 nm).

refractive indices forming the lattice. Two important changes took place when comparing the gray scale plots of the bare monolayer with those from the composite. The first concerns the spectral position of the origin of the modes, in the Γ point. In the case of the direct structure, it was found at $\lambda = 646$ nm, while for the composite it displaced to a lower energy ($\lambda = 657$ nm). The second one was the observation of a slight decrease in the slope of the modes in the dispersion relation. This was especially visible in modes ΓK3, ΓM3, and ΓM4. Both changes are consistent with the increase of the effective refraction index and lattice parameter induced by the presence of the silica.

Fourier image spectroscopy was also used in the case of the inverse colloidal structure, although it was not possible to infer any characteristic optical features from the collected contour plots. This was due to the fact that the reflectance signal was too low. This was expected, as the inverse mono-

layer had a very small amount of matter and hence a negligible scattering strength. In theory, according to Equation 2.2, the maximum silica volume fraction in a closed packed structure is 40 %. In the case of our system, the filling fraction is, at most, of the order of 30 %, which implies, in the context of an effective medium theory, that the net refractive index is only ≈ 1.1 as opposed to that of the composite (≈ 1.6).

2.6 Magnesiothermic reduction of silica

As a next step, and as an attempt to achieve structures with higher refractive index that could present increased photonic functionality, efforts were made in order to replicate the inverse monolayers described in Section 2.4 in silicon. For doing so, a displacement chemical reaction denoted as magnesiothermic reduction was explored. The magnesiothermic reduction is a process which aims at converting silica into porous nanocrystalline silicon. Its main advantage is the fact that it preserves the initial morphology of the material, particularly micro or nano features. It has been employed to convert structures such as microshells [99], waveguides [100], inverse opals [94] or monodisperse microspheres and direct opals [101]. From the point of view of photonic materials fabrication, this technique draws much attention. In fact, while silicon has a considerable higher refractive index than silica, using the current self-assembly techniques it is easier to accomplish photonic crystals composed of SiO_2. Therefore, employing the magnesiothermic reduction approach one can, in principle, fabricate materials with enhanced order and higher refractive index.

In the magnesiothermic reduction, silica is made to react with elemental magnesium gas, in an inert atmosphere. The products of the reaction are magnesia and elemental silicon, according to the reaction [99]

$$2\,\mathrm{Mg}\,(\mathrm{g}) + \mathrm{SiO_2}\,(\mathrm{s}) \rightarrow 2\,\mathrm{MgO}\,(\mathrm{s}) + \mathrm{Si}\,(\mathrm{s}). \tag{2.3}$$

The magnesia is then selectively removed by immersion in a solution of hydrochloric acid, according to the equation

$$\mathrm{MgO}\,(\mathrm{s}) + \mathrm{HCl}\,(\mathrm{aq}) \rightarrow \mathrm{MgCl_2}\,(\mathrm{aq}) + \mathrm{H_2O}\,(\mathrm{aq}). \tag{2.4}$$

The protocol followed in the current work was similar to the one proposed by Ibisate et al. [101]. A scheme of the homemade stainless steal reactor used for the reductions is shown in the figure 2.10a. Solid elemental magnesium was introduced in one of the chambers while the sample was placed in the other. As the quantity of silica composing the samples was hard to estimate

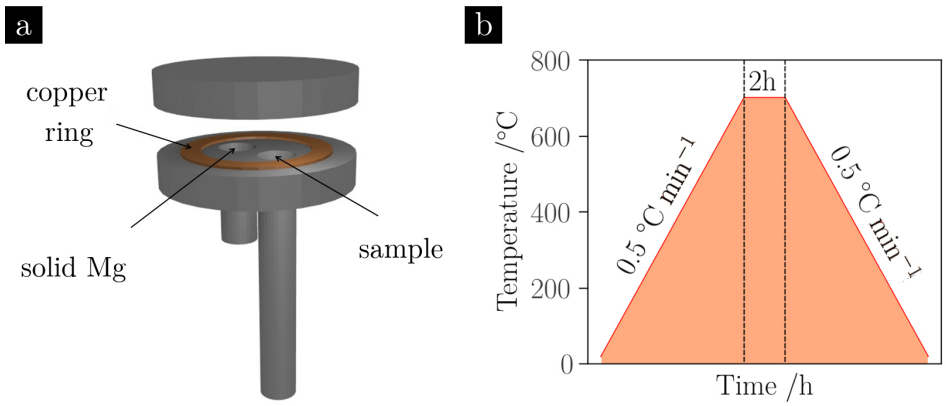

Figure 2.10: a) Scheme of the reactor used for the magnesiothermic reduction of the silica inverse membranes. b) Temperature program adopted for the process.

accurately, the quantity of elemental magnesium was qualitatively adjusted. The reactor was sealed inside a glove bag with an athmosphere composed of argon. A copper ring was compressed between the two pieces of the reactor, when screwing them together, to assure hermetic isolation. Afterwards, it was introduced in a muffle furnace and subjected to a temperature cycle composed of three ramps as illustrated in Figure 2.10b. The heating ramp was performed from room temperature to 700°C at a rate of 0.5 °C min^{-1}. Subsequently the temperature was maintained constant for 2 h and then ramped to 30 °C with an equal rate than the one of heating. Such low heating and cooling rates were selected so that thermal inertia of the furnace was not significative and also to avoid drastic mechanical strain in the samples derived from fast thermal expantions. For etching the magnesium oxide, the samples were immersed in a solution of HCl at 10 vol% in ethanol. Typically, three cycles of immersion in the etcher followed by washing with ethanol were performed.

2.7 Inverse silicon monolayers

For producing new composites with spheres of 520 nm of diameter and [TEOS] = 4.0 vol%, a process similar to that described in Section 2.2 was followed. In this case, they were fabricated using a cut piece of silicon wafer as substrate (glass cannot be used due to the high temperatures reached during the reduction). As before, these samples were calcinated for eliminating the PS spheres and next they were subjected to the magnesiothermic reduction. Figure 2.11 exhibits the SEM characterization monitored for each step of the fabrication process, both in surface and tilted views.

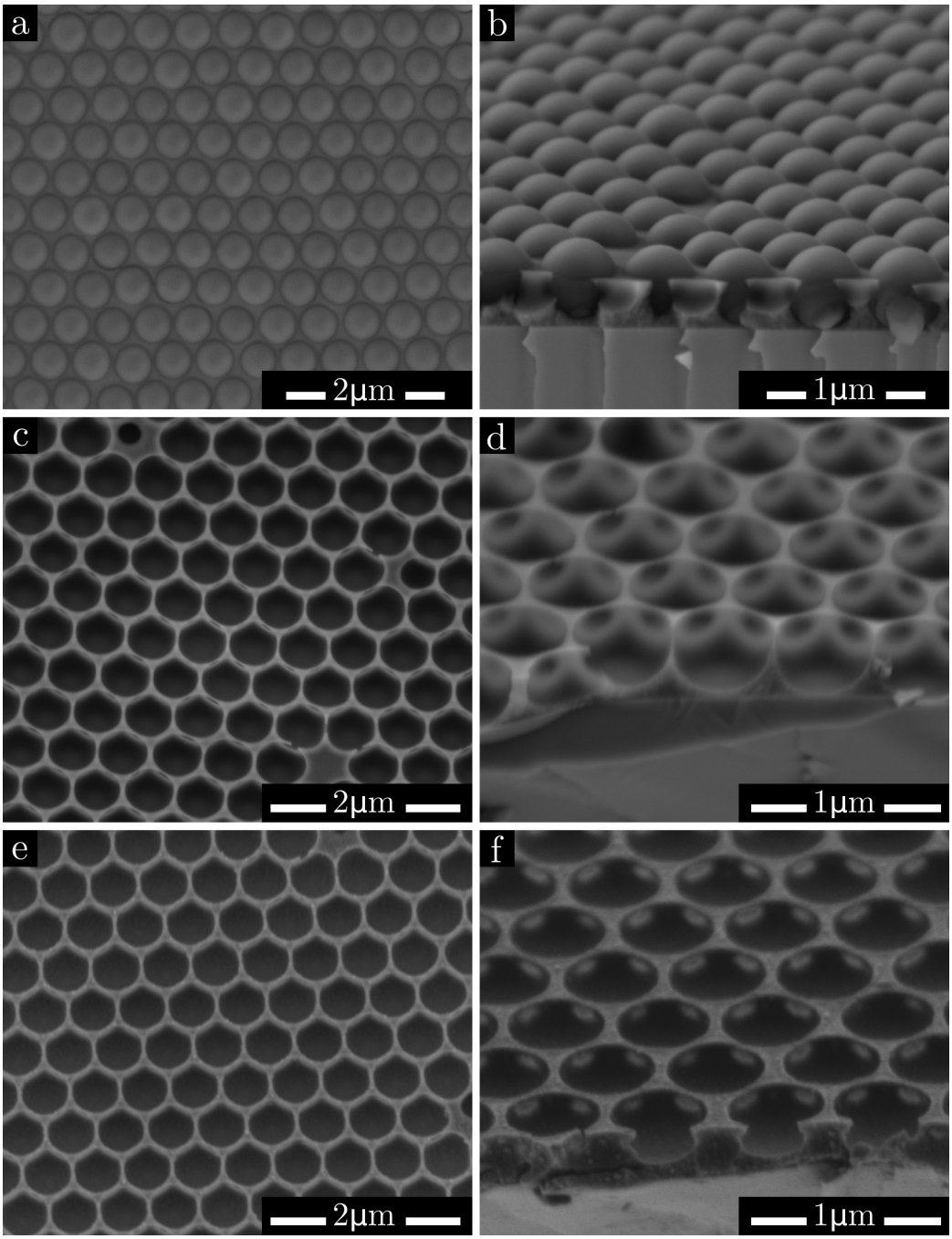

Figure 2.11: Representative SEM images of a crystal produced with spheres of diameter 520 nm and [TEOS] = 4.0 vol%. a) Surface view of the composite, b) tilted angle observation. c) and d) Respective images for the same sample after calcination. e) and f) Respective images after magnesiothermic reduction.

Figure 2.12 displays an example of the sample after being subjected to magnesium oxide etching with HCl. As may be appreciated in Figure 2.12a, the hexagonal structure was still present in the final materials, although a very distinct aspect from the one in Figures 2.11c and Figure 2.11e was observed. Tilted observation showed that the structure was not robust enough to undergo the etching procedure (Figure 2.12b). In fact, the silicon connections at the hexagon edges were lost and an unusual structure more similar to tetrapods attached to the bottom nanobowls, at the hexagon vertices of the lattice was obtained.

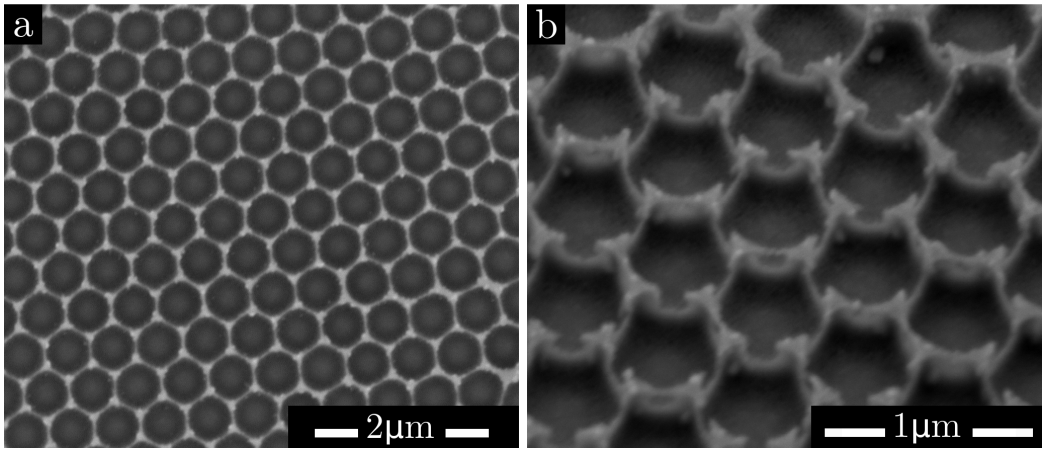

Figure 2.12: Representative SEM images of a sample produced with spheres of diameter 520 nm and [TEOS] = 4.0 vol %, after magnesiothermic reduction and chemical etching with MgO. a) Surface view of the crystalline structure and b) tilted angle observation at a higher magnification.

Furthermore, energy dispersion X-ray spectroscopy was used in order to verify the chemical composition of the final structures. As may be apreciated from the spectrum presented in Figure 2.13, the characteristic peak of the Kα transition of silicon was clearly visible at *c.a.* 1.74 keV. This peak was approximately a factor 20 more intense than that characteristic of the Kα transition of oxygen (*c.a.* 0.50 keV). Quantification of the elements resulted in a weight percentage of 98.06 % for Si and 1.94 % for O. Additionally, no peak characteristic of magnesium could be identified. These results demonstrated that the oxides were correctly etched from the sample and assured that only silicon remained on the crystals, as expected.

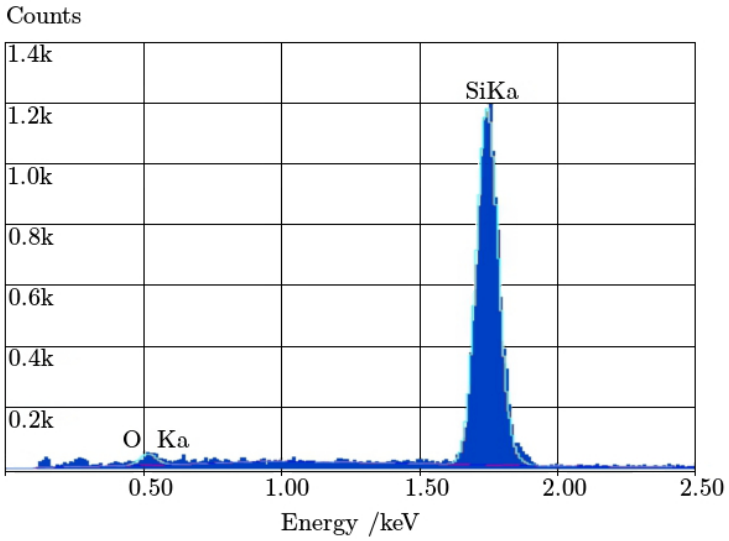

Figure 2.13: Representative energy dispersion X-ray spectrum of an attemp to fabricate silicon IOs, at the end of the fabrication process.

2.8 Conclusions

The optimal growth parameters for the fabrication of composite monolayers consisting of ordered arrays of PS spheres in a silica background were investigated in order to achieve the widest areas of infiltration, as well as to achieve the best quality at the microscopic level. Specifically, we studied the correlation between the concentration of the silica precursor in the original suspension with the degree of infiltration of the sample and the thickness of the silica layer. Although linear fits of the filling fraction as a function of [TEOS] exhibit a slight increase for samples produced with spheres of 430 and 520 nm of diameter, a definite tendency is not demonstrated as the experimentally found values do not stand out significantly from the experimental error. At a later phase, it was shown that the composite structure was robust enough to withstand the thermal treatments used for the removal of the PS spheres. Thus, although defects were introduced by the calcination, it was possible to obtain large area inverse monolayers of good quality.

The reported results demonstrated that coassembly growth was compatible with the wedge-shape confinement method for the fabrication of composite monolayers. Thus, it is possible to reduce the number of steps to produce these structures while taking advantage of the increased quality attainable by the cell confinement. Moreover, this material served as the basis for the production of the inverse monolayer, achieved by thermal treatment.

The trials for the replication of these membranes using silicon have not been successful until now as, although the membranes resisted the magnesiothermic reduction process, the interconnected lattice was lost after chemical etching for the removal of possible remaining oxides. Incidently, the proposed fabrication method has shown to be interesting for achieving more exotic structures with potential interest for coatings and for templating.

The procedure here presented allows for versatile control over the composite morphology and thus its optical response. Although the current approach is based on the use of SiO_2, the applicability of the method is currently being studied and optimized for higher refractive index materials such as TiO_2 [94] and silicon [99]. Their use could grant higher light/matter interactions. Further, the possibility of adding metallic components could pave the way to realize hybrid photonic−plasmonic systems whose optical properties are being actively explored [102,103]. We envision the kind of system proposed here may be applied in solar cells, sensing, as black silicon [104] or in the manipulation of nanocrystalline porous silicon emission [105, 106]. Moreover, silicon porous membranes, for example, are expected to be useful as anode materials in rechargeable Li ion batteries [107]. Optionally, the proposed growth can be applied in surface patterning or in the production of nanostructured templates for diverse applications.

3

Three dimensional PCs aiming light control in the infrared

The possibility of incorporating rare earth ions, specifically erbium and ytterbium, within silica three dimensional photonic crystals fabricated by self-assembly is assessed. For this end, two strategies are discussed. In first place, doped coassembly is shown uneffective for producing doped inverse opals, due to the fact that the rare earth ions induce colloidal instability, hindering the self-assembly. The second strategy consists of vapor phase doping of previously grown crystals. This method is shown to be adequate for achieving rare earth ions incorporation. Photoluminescence is systematically analyzed in these samples in order to study potential effects of the ΓL pseudogap in the emission.

Alternatively, the fabrication of inverse silicon opals with a full photonic bandgap in the infrared region (1.5 μm) is tested. Intermediate steps towards this end are presented and characterized with SEM and FTIR spectroscopy. The proposed experimental approach is shown to be effective for partially fulfilling the objective, although very low quality and non-uniform crystals are obtained. In this way, the throughput of the process is reduced, limiting the application of this system for further studies.

3.1 Introduction

As detailed in Section 1.3.2, artificial opals grown by self-assembly of submicrometer spheres, are very attractive, cost-effective photonic systems [64]. The effect of opaline structures on spontaneous emission has been already demonstrated for luminophores such as organic dyes [108], quantum dots [109], and rare earth (RE) ions [110]. For luminescence studies, RE emitters

present significant advantages [111], mostly due to the fact that their emissions typically correspond to 4f intra-subshell transitions, which are screened by the completely filled 5s and 5p outer shells. For this reason, RE ions typically present very narrow emission lines, reasonably insensitive to the chemical environment surrounding them. Further, RE emission is also highly photostable, exhibits high quantum yields and monoexponential decay behavior, with characteristic lifetimes of the order of miliseconds or hundreds of microseconds.

Previous work reporting the effect of opal-like structures in the manipulation of RE ions spontaneous emission includes the use of bare silica opals [112, 113] and composite opals with infilled pores [114–116]. RE elements have been incorporated directly into colloidal silica [117] or titania [118] spheres. Moreover, inverse opals (IO) have been employed for hosting RE ions as well. They have been fabricated in such diverse compositions as lanthanum phosphate [119], magnesium silicate [120], silicon oxide [121, 122] and silicon [110, 123], this last one possibly exhibiting a full-PBG. Interestingly, RE-doped opal systems have also been used to study the influence of PBGs in the emission resulting from nonlinear processes, in which upconversion luminescence enhancement or inhibition has been reported [124, 125]. In the above work, the doping of the photonic crystals (PCs) was performed with RE elements such as europium, terbium, neodymium, ytterbium and erbium, the incorporation of the ions being accomplished with impregnation, sol/gel dip-coating and also ion implantation. While the last method enables a fine control of the position of the doping emitter in the structure, with the former techniques it is possible to achieve a more homogeneous distribution of the REs within the crystal.

As mentioned, erbium is among the targeted RE emitters for incorporating in PCs aiming at the control of its emission. Trivalent erbium is, in fact, one of the most relevant RE ions due to its importance for optical communications. The transition between its atomic levels $^4I_{13/2}$ and $^4I_{15/2}$ corresponds to emission of photons at the wavelength of 1.54 μm, which superimposes the lowest absorption band in silica - the fundamental material composing optical fibers. This is the commonly known C-band of optical communications. Er has been used, for example, for the development of a new kind of fiber amplifier (EDFA), which allows the amplification functionality to be kept in the optical domain [126].

In spite of its relevance, Er has an important drawback: its low absorption cross section, which makes it difficult to pump and implement in devices. One strategy to overcome this problem is to sensitize Er with another ion with higher absorption cross section. Ytterbium is the most favorable selection [127], as it possesses a resonant energy level - corresponding to transi-

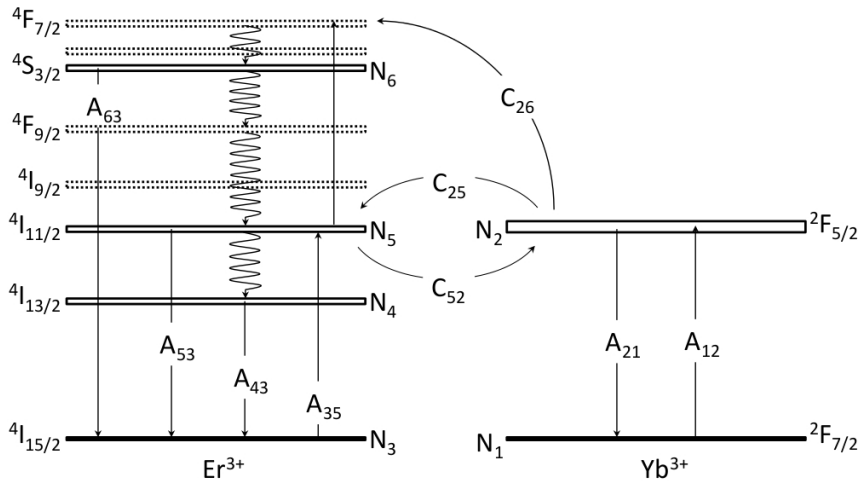

Figure 3.1: Diagram of the energy levels of Er^{3+} and Yb^{3+} ions illustrating the possible energy transfer mechanisms between them. Straight arrows represent absorption or radiative relaxations while waving arrows represent non-radiative de-excitations.

tions between levels $^2F_{5/2}$ and $^2F_{7/2}$. The energy diagram in Figure 3.1 aids the visualization of the possible energy exchange mechanisms between the two ions. Besides its own radiative relaxation mechanism, an electron in the excited state $^2F_{5/2}$ of Yb might relax to the fundamental state via resonant transfer of a photon to an electron in the fundamental state of Er - which excites to the $^4I_{11/2}$ level - or via transfer of a photon to an already excited electron in state $^4I_{11/2}$ - in which case the electron excites to level $^4F_{7/2}$. In the erbium energy diagram, the waving arrows illustrate nonradiative relaxation mechanisms. The downward straight arrows signal the three most significant lines of the emission spectrum of Er at 1.5 μm, 1.0 μm and 0.55 μm. The last one corresponds to emission in visible range occurring through an upconversion mechanism.

The objective of the present work was to ascertain the behavior of the Er^{3+}/Yb^{3+} system in a photonic environment consisting of the silica IO and, afterwards, of the silicon IO. Particularly, we discuss the possibility of using a doped coassembly approach followed by calcination for producing three dimensional silica/polystyrene composites and their respective inverse crystals. This method revealed to be non-effective, hindering the fabrication of good quality samples. For this reason, an alternative approach consisting of vapor phase doping of previously grown inverse opals was explored. We present the comparison of the Er^{3+}/Yb^{3+} system luminescence in two different silica IO structures: one with the PBG (ΓL direction) centered at the 1.5 μm region

and one with the PBG far from the photoluminescence (PL). Contrarily to previous approaches (based on impregnation), for the RE doping of the IO, atomic layer deposition was selected [128]. By doing so, we tried to solve the problem of RE low solubility in silica [129] and obtain a homogeneous distribution of the emitters in the PC. This study emmerged as an intermediate step for fabricating doped silicon IO, exhibiting a full PBG at the erbium PL line. Attempts for fabricating silicon IOs are discussed afterwards.

3.2 Theoretical calculations

For the design of the PCs and the correct choice of spheres size constituting the template, theoretical calculations of band structures were done using the freeware package *MIT Photonic Bands* [130]. This software calculates eigenstates of the Maxwell equations using a planewave basis expansion. In Figure 3.2 we present several band structures for the ΓL direction, which is the one typically probed in experiments corresponding to different kinds of crystals fabricated in this thesis. In particular, the structures of a bare PS opal, a composite made of PS spheres embedded in a silica matrix (that is the structure resulting from the co-assembly deposition), a silica IO and the finally aimed silicon IO are shown. The vertical axis is expressed in relative units (a/λ), being $a = \sqrt{2}\phi$ for the fcc symmetry, where ϕ is the spheres diameter.

For the PS bare opal, a gap was found at $a/\lambda = 0.60$. It is well known that this corresponds to a pseudogap as, due to its low refractive index contrast, this structure cannot sustain a fPBG. If the PC is infiltrated with silica, this gap displaced to lower energies ($a/\lambda = 0.56$), due to the increase of the effective refractive index. Moreover, because the index contrast decreases, the width of the gap is also reduced. This had also effect on the high energy region. Comparing the bands at this spectral region between the PS bare opal and the composite, it was possible to conclude that the degeneracy separation is much more pronounced in the first ones, while the second dispersion relation was much more similar to the one of a homogeneous medium. If the PS was substituted by air in the opal, the gap suffered a blueshift becoming centered at $a/\lambda = 0.77$ and again widened due to the increase of refractive index contrast. Two photonic gaps could be observed in the band structure of the silicon IO, as expected. The ΓL pseudogap was obtained for $a/\lambda = 0.48$ and another gap centered at 0.79, which corresponds to the fPBG, as may be appreciated from the calculation of the complete Brilloin zone (as shown in Chapter 1, Figure 1.4). Therefore, in order for the fPBG to be centered at $\lambda = 1550$ nm, the sphere size to use should be of around $\phi = 870$ nm.

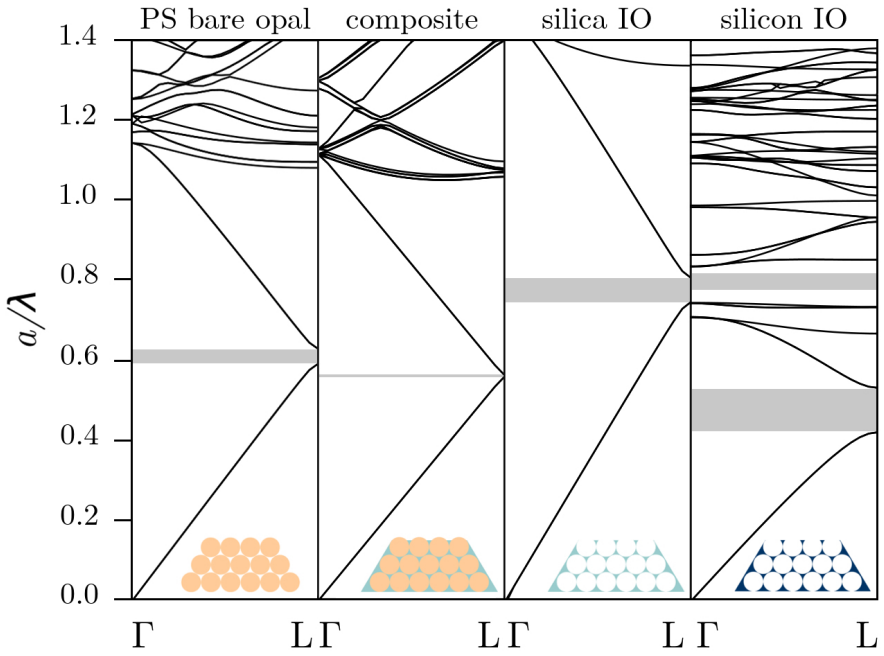

Figure 3.2: Theoretical bandstructure calculations for the ΓL direction of different photonic structures - bare PS opal, composite of PS spheres embedded in a silica matrix, silica IO and silicon IO. Photonic gaps are signaled as grey rectangles.

3.3 Fabrication of crystals by vertical deposition method

The vertical deposition method, was introduced in 1999 by Jiang *et al.* [13] and it became one of the most widespread techniques used to grow artificial opals. The reason is that it enables the fabrication of uniform, good quality crystals and, to some extent, it allows the control over their thickness (number of sphere layers). The method is based on the convective self-assembly of the particles at an interface solid/liquid/vapor, by the action of a moving meniscus [131].

In general, a flat hydrophilic substrate, such as a microscope slide or a piece of crystaline silicon wafer, is immersed in a colloidal suspension (Figure 3.3). The crystal begins to grow at the point where the thickness of the liquid meniscus becomes smaller than the spheres size - onset of ordering [132]. The deformation of the meniscus around the particles, at that interface, gives

origin to interparticle attraction, leading to the formation of small clusters. These play the role of nucleation points. As the solvent evaporates, the local capillary pressure at the interface increases and the spheres are pulled towards the substrate and towards each other. The growth develops from there on by convective transport of particles and the opal thickness increases monotonically untill an equilibrium thickness is reached.

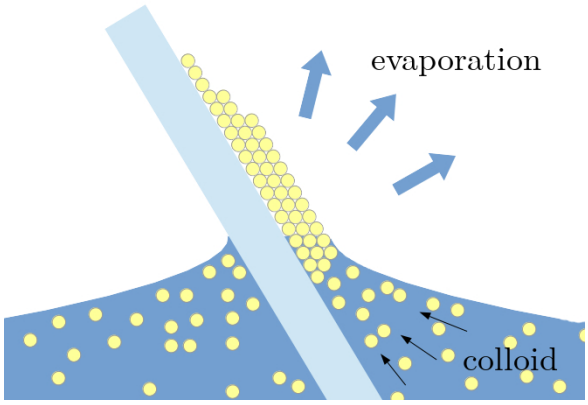

Figure 3.3: Schematic illustration of the vertical deposition method based on the convective self-assembly of particles at a solid/liquid/vapor interface.

From the previously discussed, the evaporation rate of the solvent is a determinant parameter affecting the crystallization, as is the mechanism responsible for the solvent transport and, consequently, the particles supply towards the meniscus. It may be controlled by acting on the temperature - specifically, by increasing the temperature, the evaporation rate will increase - or on the relative humidity - decreasing the relative humidity, the evaporation rate will increase. Therefore, these parameters should be adjusted in order to compensate for the sedimentation of particles due to gravitational forces. If the evaporation is too slow, a significant amount of spheres may sediment before being able to assemble. This effect is more dramatic for silica particles with sizes above 600 nm, which are heavy and therefore precipitate fast. In this sense, regarding big sized particles as the ones with interest for this work, it is easier to assemble polymeric spheres due to their smaller mass density and, consequently, their slower sedimentation rate in comparison to silica particles. Another important parameter influencing the crystallization is the concentration of the colloid. In general, an increase of the colloid concentration leads to a increase of the opal thickness.

3.4 Fabrication of composites by co-assembly

The conventional method for fabricating three dimensional opaline composites or inverse opaline structures has relied mostly on producing the bare crystal and then infiltrating it using some chemical or physical deposition system, followed by removal of the sacrificial template (for inversion). Nevertheless, there are some limitations of these methods. For example, liquid phase infiltration frequently gives origin to the formation of defects as overlayer coatings, multiple domains and cracking [94]. On its turn, vapor phase infiltration may only take place while the crystal presents interconnected pores through which the precursors may diffuse. This fact implies that it is impossible to fill 100% of the pore volume using these techniques [93].

In 2010, Hatton and coworkers introduced a single step method for fabricating a colloidal composite consisting of PS spheres embedded in a silica matrix [94]. It combines the simultaneous PS template self-assembly with the silica matrix infiltration by sol/gel processing. This approach presents some advantages such as the reduction of cracks density, growth of large and highly ordered domains, prevention of non-uniform infiltration and the ability to assemble crystals in non flat substrates. In what follows, we discuss briefly the sol/gel process through which the silica is synthesized.

The sol/gel synthesis is a very convenient route for the deposition of inorganic matrices from the polymerization of molecular precursors. It allows the production of glasses or ceramics, at temperatures much lower than those usually employed in powders synthering techniques [133]. It is also the basis of the well-known Stöber method for the fabrication of monodisperse silica spheres [134]. Specifically, the sol/gel synthesis is based on the formation of a colloidal suspension of solid particles in a liquid phase (sol) by means of hydrolysis and condensation reactions and the gelation of the sol. For producing silica by sol/gel, the precursor is usually a liquid alkoxide $Si(OR)_4$, where the group R is typically of the form C_nH_{2n+1}. The synthesis is schematized by the chemical equations shown in Figure 3.4. In our case, the selected alkoxide was tetraethyl orthosilicate ($n = 2$).

The hydrolysis reaction must be performed in an alcoholic medium due to the low miscibility of tetraethyl orthosilicate in water. Because an alcohol (ethanol) is also the product of the condensation, its presence may slow the reaction kinetics. This fact, added to the extremely slow rate of the hydrolysis in neutral pH, justifies the addition of an acid or basic catalyst to accelerate the synthesis. However, for the same concentration of catalyst, the kinetics is typically much faster in acid environments than in basic ones. For this reason, a sol/gel process will tend to produce a continuous matrix using acid catalysts as opposite to individualized particles for basic catalysts. The target of the

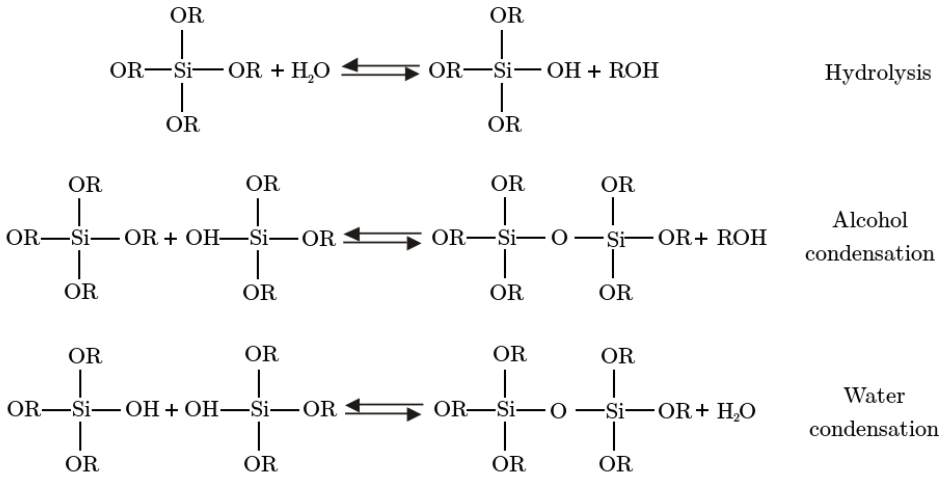

Figure 3.4: Chemical equations illustrating the sol/gel silica synthesis based on the hydrolysis of an alkoxide followed by condensation reactions producing either an alcohol or water.

current work was to achieve a continuous matrix infiltrating the interstices of the PS template, therefore an acid (HCl) was selected as catalyst. Following the procedure of Hatton and coworkers [94], the mixture (1.5 vol% ethanol : 1 vol% 0.1 M HCl in water : 1 vol% tetraethyl orthosilicate) (denoted as TEOS from now on) was pre-hydrolyzed during 1 h before adding it to the colloids for performing the vertical deposition. After this addition, the hydrolysis keeps taking place, as well as the condensation reactions. In this step, silanol species produced during the hydrolysis polymerize with the formation of siloxane bonds (≡Si-O-Si≡) and production of water or ethanol (Figure 3.4).

3.5 Optimization of TEOS concentration

Similarly to the monolayers presented in the previous chapter, it was also possible to observe different growth regimes for the three dimensional composite crystals. Co-assembly, accompanied by template infiltration of the structures, occurred while there was tetraethyl orthosilicate available to hydrolyze and condense. Nevertheless, at some point, TEOS was consumed, although there were still particles available in the colloid to continue the crystallization. For this reason, the growth of a bare opal developed from thereon. The frontier marking this transition is exemplified in Figure 3.5 which shows a representative SEM image of the effect.

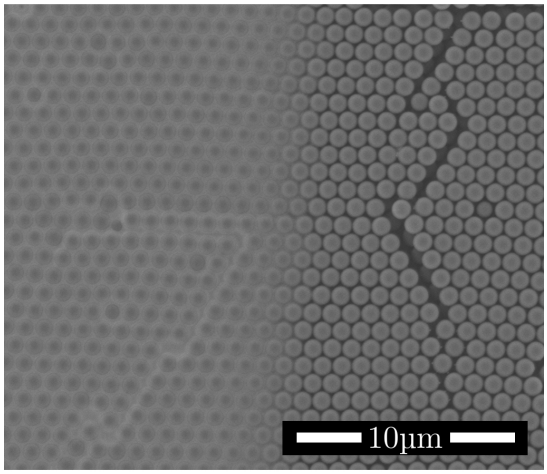

Figure 3.5: Representative SEM image exhibiting the typical frontier observed in co-assembly grown crystals, after all TEOS precursor had condensed and only bare opal grows thereon.

As a first step for the co-assembly vertical depostion implementation, aiming at the fabrication of composite opals, the concentration of the TEOS precursor was adjusted in the interval [0.0, 2.0] vol%. A set of samples was produced using pieces of silicon wafer (approximately 1 × 2 cm^2) as a substrate. They were immersed in chromic mixture for 30 min and then abundantly rinsed with distilled water. Colloids were prepared in clean vials, totalling a final volume of 10 mL each. A volume of 250 μL of the commercial suspension (ϕ = 870 nm, originally at a concentration of 10 wt%) was added to each vial, as well as the respective volume of TEOS and double distilled water. The substrates were immersed in the colloid and everything was placed in a climatic chamber, with temperature 45°C and relative humidity of 20 %, in order to evaporate the solvent and proceed with the crystallization of the opal.

Figure 3.6 shows a representative SEM image of a sample produced with [TEOS] = 0.25 vol%. As may be appreciated, it was not possible to achieve a continuous matrix of silica filling in the interstices between spheres. In this case, it is probable that silica aggregates nucleate in the colloid and increase size by condensation. Similarly to the PS particles, they displace towards the meniscus region by convective transport and incorporated into the crystal. Nevertheless, due to the low precursor concentration, the amount of silica produced is not enough to fill the pores. Notably, the presence of silica induces a non-close packed morphology with an approximately 7% increase of the lattice parameter with respect to the close packed structure.

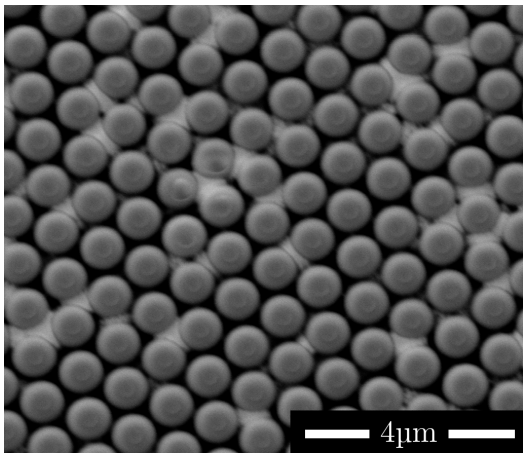

Figure 3.6: SEM image of a composite opal produced with a too low concentration of the silica precursor - [TEOS] = 0.25 vol%.

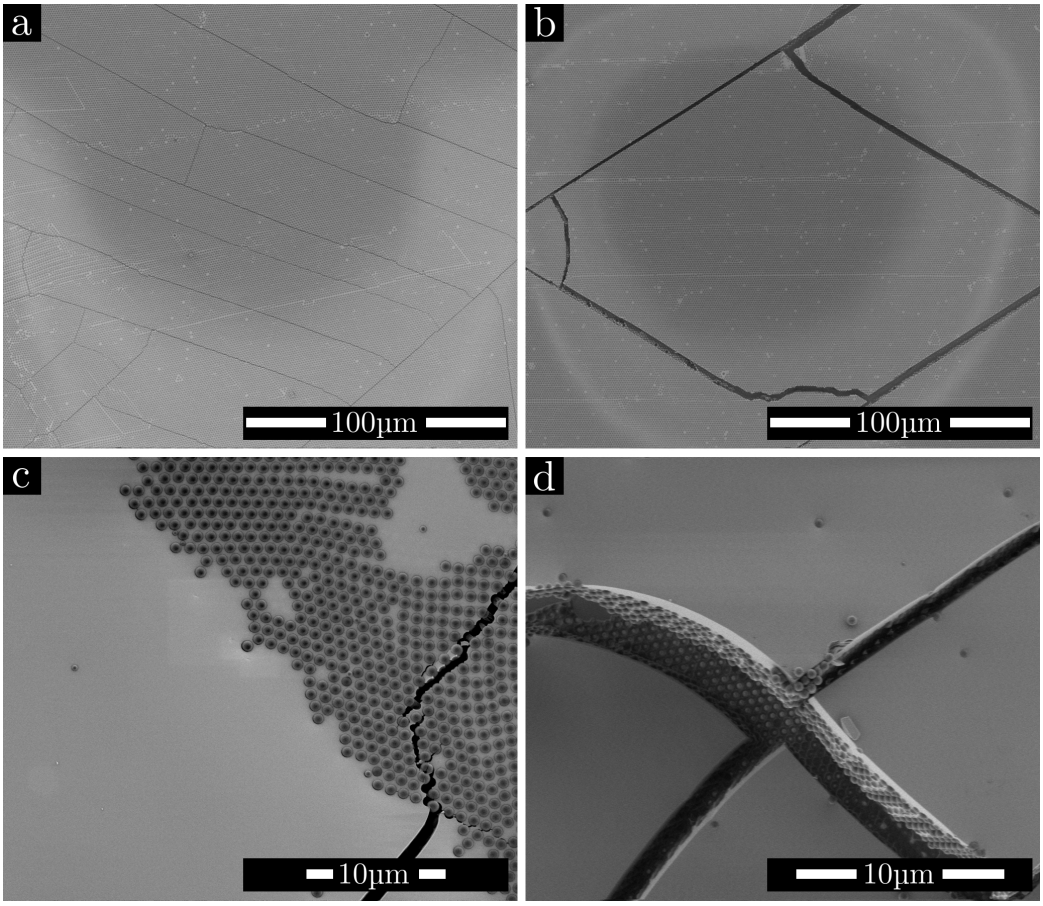

Figure 3.7: SEM images of composite opals produced with a concentration of TEOS of a) 0.5 vol%, b) 1.0 vol%, c) 1.5 vol% and d) 2.0 vol%.

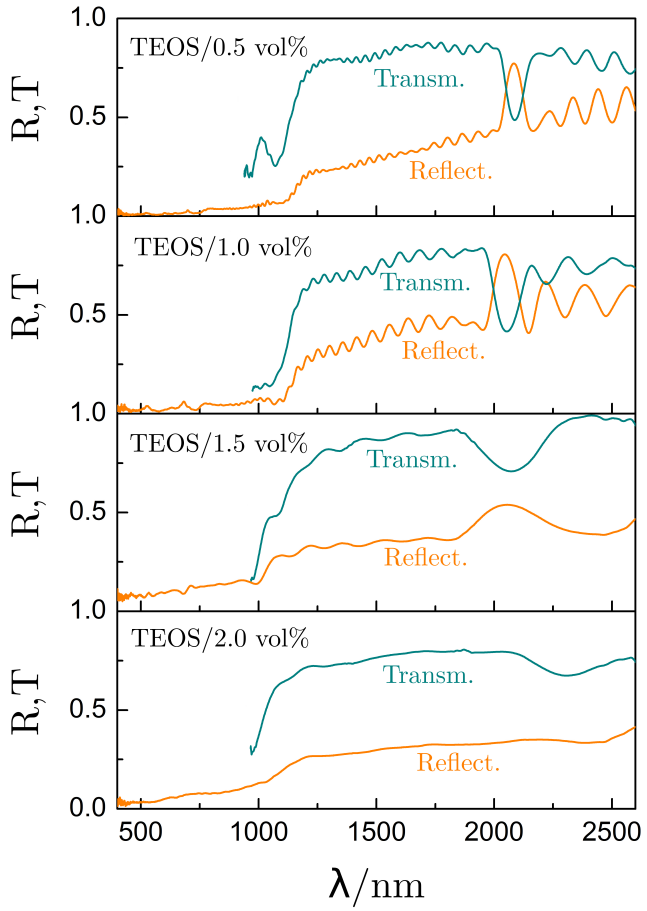

Figure 3.8: Reflectance and transmittance spectra collected along the 111 direction for the composite opals grown with increasing concentration of silica precursor.

For the TEOS concentrations of 0.5 vol% and 1.0 vol%, a complete matrix infiltrating the PS template was observed (Figure 3.7a and Figure 3.7b, respectively). The samples presented good crystalline order and extense regions free of cracks. For higher TEOS concentrations (Figure 3.7c and Figure 3.7d), a silica overlayer was observed covering the underlying composite. Moreover, it was observed that, for such concentrations, the crystallinity degree was worse, more appearing deffects and different packaging structures. Additionally, there seems to be an increase of mechanical stresses, as the crystal curved at the edges between cracks.

The samples were further characterized by FTIR spectroscopy. Figure 3.8 presents the evolution of reflectance and transmittance spectra with increasing amount of TEOS in the range of [TEOS] = [0.5, 2.0] vol%. The shape of

the spectra agreed with the results obtained by SEM. A Bragg peak was observed centered at $\lambda = 2082$ nm (2044 nm) for [TEOS] = 0.5 vol% (1.0 vol%). The positions of these peaks were near that theoretically predicted (Figure 3.2) - calculations determined that the gap should be centered around $\lambda =$ 2197 nm. The smaller value of the colloidal silica refractive index, as well as finite crystal size effects, acounts for the slight differences observed [135]. For the sample produced with [TEOS] = 1.5 vol%, the Bragg peak was still detected, centered at $\lambda = 2038$ nm, which indicated that the grown overlayer was very thin. Nevertheless, the peak was spectrally much broader and the Fabry-Perot oscillations more spaced, a signal that the sample was constituted by a smaller number of sphere layers. Therefore, the overlayer seemed not to have a dramatic impact on the presence of the pseudogap, although the effective reduction of the opal was a hint that some colloidal instability could be starting to take place at this concentration. Finally, Fabry-Perot oscillations were not observed in the spectra for the sample of [TEOS] = 2.0 vol%, neither the Bragg peak. These results, in conjunction with SEM analysis, pointed out that the concentration interval [0.5, 1.0] vol% was the most suitable for fabricating the composite opals.

3.6 Fabrication of composites by doped co-assembly

As a preliminary study for the preparation of IOs by doped coassembly, silica films were fabricated on bare silicon substrates, by a sol-gel method, starting from different Er dopant precursors. This study was done in order to investigate which of the precursors allowed the best RE dispersion in the silica matrix, aiming at the highest possible emission efficiency. Specifically, a TEOS solution was prepared (see Section 2.2) and after 45 min of pre-hydrolysis it was separated in three parts. A quantity of 1 mol% of dopant erbium precursor, namely erbium (III) fluoride (ErF_3), erbium (III) chloride ($ErCl_3$) or erbium (III) nitrate pentahydrate ($Er(NO_3)_3{\cdot}5H_2O$), was added to each pre-hydrolised TEOS solution, after which the solutions were further sonicated for 15 min. Three films containing the Er precursor were cast into the substrates and then annealed at 1000 °C for 1 h. This treatment is required in order to activate the Er PL by removing hydroxyl groups, which are known to be responsible for the 1.5 μm band emission quenching [136]. PL spectroscopy results revealed similar performance of samples doped with $ErCl_3$ and $Er(NO_3)_3{\cdot}5H_2O$, while no PL signal could be identified from the

film doped with ErF_3. In view of these results and in order to keep the ionic species in the colloid similar (Cl^- is present already due to HCl), $ErCl_3$ and $YbCl_3$ precursors were initially selected.

To ascertain the maximum RE doping quantities allowed without perturbing the colloidal stability of the suspensions, flocculation tests were carried out. A set of suspensions (10 ml each) was prepared. For a fixed concentration of commercial polystyrene (PS) colloid of 1.0 vol% (Thermo Scientific, $\phi = 870$ nm, original concentration 10 wt%) and a concentration of TEOS of 1.0 vol%, the concentration of Er and Yb ions was varied in the range [0,1] mol% and [0,7.5] mol%, respectively, according to previous optimization reports [137]. The colloids were sonicated for a few minutes for homogenization and then introduced in an oven with temperature conditions similar to those used for assembling opals. The state of the suspensions was monitored up to a maximum of 24 h. It was verified that in all of the co-doped samples (containing both Er and Yb) flocculation and precipitation occurred in the first few hours. However, samples produced incorporating up to 1 mol% of Er exclusively, preserved their stability for the complete period. This preliminary experiment allowed us to conclude that the presence of the charged ions perturbed the rheological stability of the colloid [97]. It also showed that the maximum concentration of REs not dramatically affecting that stability was 1 mol%.

Considering the conclusions of these preliminary tests, new experiments were performed aiming at the fabrication of composite opals by RE-doped coassembly - therefore constituted by PS spheres embedded in a matrix of Er-doped silica. For this, an adapted version of the vertical deposition procedure [94], incorporating the doping with Er, was employed. Similarly to the preliminary tests, colloids were prepared using a fixed [TEOS] = 1.0 vol% and a concentration of the PS commercial colloid of 1.0 vol%. A small quantity of $ErCl_3$ was added to the pre-hydrolized TEOS, in the range [0,1.0] mol%. The samples were placed in an oven at T = 65°C and left to evaporate the solvent for approximately 48 h.

After collecting the substrates, very low adhesion of the composites was observed. The deposited materials presented small thickness, with only a few layers of spheres. Furthermore, they presented a white aspect, with no observable iridescence, which is a characteristic of disordered non-absorbing photonic materials. The typical microscopic aspect of these samples is exemplified in Figure 3.9. As may be appreciated, a composite was in fact obtained, although the crystallization was dramaticaly precluded due to the presence of the RE ions. These results demonstrated that, even using the minimum quantity of Er dopant possible, no crystalline opaline materials were obtained.

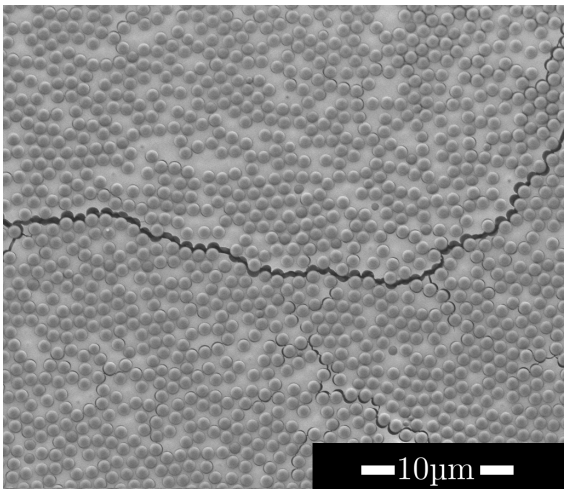

Figure 3.9: Representative SEM micrograph of a sample fabricated by Er-doped coassembly using polystyrene spheres of 870 nm in diameter (Er concentration 0.75 mol%).

In the previous experiment, PS spheres were employed for testing the fabrication of the opal composites. This kind of particles possesses a hydrophobic anionic surface. In order to test the possible effect of surface properties in the opals growth and to improve their crystalline quality, new tests were done using PMMA spheres which are synthesized with a hydrophilic anionic surface. In first place, a new preliminary aggregation test was performed. Similarly to the PS essays, a set of samples each with a total volume of 10 ml was prepared using [TEOS] = 1.0 vol% and a concentration of commercial colloid of 1.0 vol% (PMMA particles with $\phi = 652$ nm at an original concentration of 10 wt%). The quantity of $ErCl_3$ and $YbCl_3$ added to the TEOS mixture ranged from [0, 1] mol% and [0, 7.5] mol%, respectively. Interestingly, no flocculation was observed for the colloids prepared with PMMA spheres, regardless of the RE dopants concentration used, up to the maximum ones.

New composites were tested for co-doped coassembly growth using the PMMA spheres. A summary of the colloids prepared in this experiment is presented in Table 3.1. With these conditions, it was hypothesized that their stability could be better preserved, what could have a positive impact on the spheres crystallization during the evaporation step. Figure 3.10 exhibits representative SEM images of two composites obtained. Figure 3.10a shows an example of the (undoped) control sample - sample 5 in Table 3.1. Although it was possible to identify some characteristic defects such as missing spheres or dislocations, a very good overall degree of order could be appreciated. On the contrary, for the doped samples, even those doped with Er only,

	v_{tot} [ml]	[TEOS] [vol%]	$c(\phi)$ [vol%]	[Er] [mol%]	[Yb] [mol%]
1	10	1.0	1.0	1.00	0.75
2	10	1.0	1.0	1.00	0.00
3	10	1.0	1.0	0.75	0.00
4	10	1.0	1.0	0.50	0.00
5	10	1.0	1.0	0.00	0.00

Table 3.1: Summary of the set of samples produced by co-doped coassembly and using PMMA spheres. From left to right: sample label, total volume of colloid prepared (v_{tot}), concentration of silica precursor ([TEOS]), concentration of commercial colloid originally at 10 wt% ($c(\phi)$), concentration of erbium ([Er]) and ytterbium ([Yb]) added to the pre-hydrolized TEOS solution.

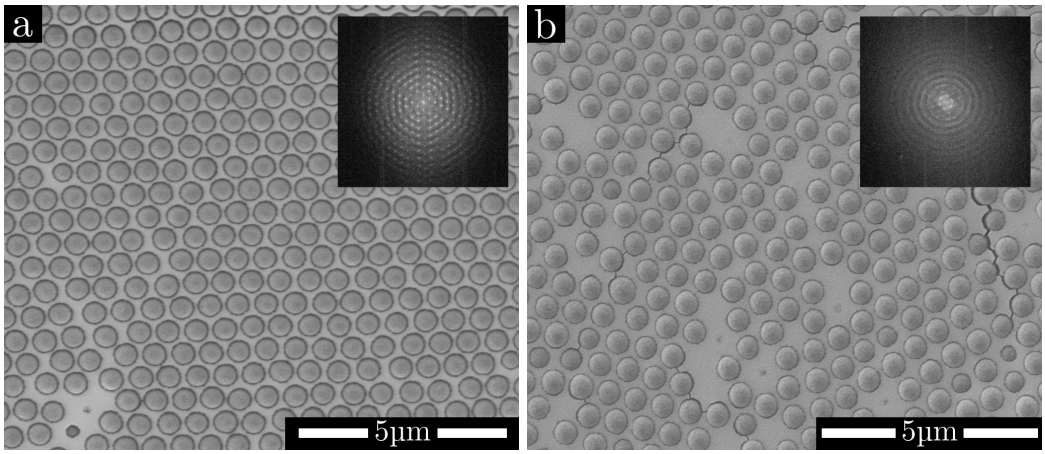

Figure 3.10: Representative SEM images of the composites grown by co-doped coassembly, using spheres of PMMA of $\phi = 652$ nm. a) Control sample with [Er] = 0.00 mol% and b) [Er] = 0.50 mol%. The respective Fourier transform of the image is shown in the insets.

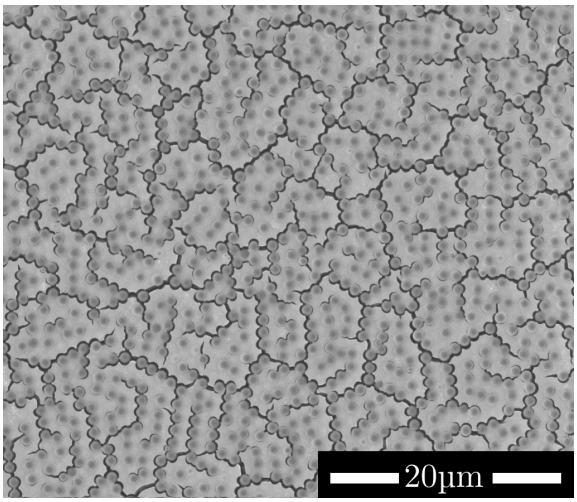

Figure 3.11: SEM image of a co-doped coassembly test, using tris(2,2,6,6-tetramethyl-3,5-heptanedionate)erbium(III) as doping precursor. In this example, the concentration of Er was 0.75 mol%.

amorphous morphologies were obtained, exhibiting only very short range order (the sample doped with 0.50 mol% - sample 4 in Table 3.1 - is shown in Figure 3.10b). The comparison may be also appreciated in the Fourier Transformed images shown in the insets of the figure. In the first case, the transform exhibits individual points, disposed in the characteristic hexagonal pattern, pointing out to a good quality and high degree of order. In the case of the amorphous structure, the transform is composed of a small number of concentric rings, a typical sign of short range order, only.

The search for the improvement of the crystalline order of the samples encouraged us to investigate the influence of some additional parameters namely, the time of addition of the RE ions during the TEOS hydrolisis and the kinetics of the hydrolisis reaction (by changing the amount of acid catalyst in the mixture). Systematic tests done changing these conditions led to the growth of composites quite similars to those shown in Figure 3.10b, meaning that it was not possible to identify any correlation between them and an enhancement of order. Furthermore, doping with other precursors was explored, including ErF_3 and $Er(NO_3)_3{\cdot}5H_2O$, which had been initially discarded, with equivalent results. As a final test, doping using tris(2,2,6,6-tetramethyl-3,5-heptanedionate)erbium(III) was attempted. In this case, the Er ion is protected by organic methyl groups which could lead to some charge shielding. Nevertheless, results showed that also in this case very poor degree of order was obtained and furthermore, the silica properties were compromised as it presented significant cracking (Figure 3.11).

3.7 RE doping of inverse opals using atomic layer deposition

As detailed in Chapter 1, IOs are functional materials that present a high degree of interconnected porosity, with a very narrow distribution of pore sizes [138]. For that reason, they have impact on areas as distinct as tissue engineering where they can play the role of scaffolds for cell growth [18, 139], sensing for pH measurement or chemical species detection [140, 141], catalysis where the presence of photonic bandgaps may enhance photocatalytic activity [142], energy for the fabrication of electrodes with application in lithium ion batteries [17] and, certainly, in photonics [143, 144].

Based on the outcome of the initial tests regarding the production of doped IOs, discussed in the last section, a new approach was attempted based on four successive steps: a) fabrication of good quality composites made of PS spheres embedded in a silica matrix, b) calcination for removal of the sacrificial PS and production of the inverse structures, c) co-doping with Er^{3+} and Yb^{3+} ions by atomic layer deposition, and d) thermal annealing for photoluminescence activation of the REs. For comparison, in order to ascertain possible photonic effects due to the presence of gaps, two kinds of samples were fabricated, one with spheres of diameter $\phi = 490$ nm and the other of $\phi = 870$ nm. According to theoretical calculations, the IOs produced with the former ones should not present any gaps in the Er PL region, while the ΓL pseudo gap should be tuned with the PL peak in the later ones.

Composites of PS spheres embedded in a silica matrix were produced using the vertical deposition method [13] in conjunction with coassembly [94]. As the process was already described in Section 3.4, in what follows we briefly review only the specificities. For the preparation of the colloids, in the case of the samples produced with spheres of $\phi = 490$ nm, 9.8 ml of distilled water (18.2 MΩ) were poured into each vial, as well as 50 μl of TEOS and 150 μl of the commercial spheres suspension. In the case of the samples produced with spheres of $\phi = 870$ nm, the volume of distilled water added was 9.7 ml, the volume of TEOS 50 μl and the one of the commercial suspension 250 μl. The slight concentration adjustment was made for compensating the highest sedimentation rate of the heavier particles. Regarding the preparation of the substrates, quartz slides were cut and washed with water and detergent. Then, they were rinsed with distilled water and dried under a nitrogen flux. The same was done for the preparation of glass vials. The vials were filled with hydrogen peroxide (H_2O_2) and placed in a thermal bath at the temperature of 80°C. The quartz substrates were immersed into them and left to hydrophilize. After 1 h, both substrates and vials were carefully

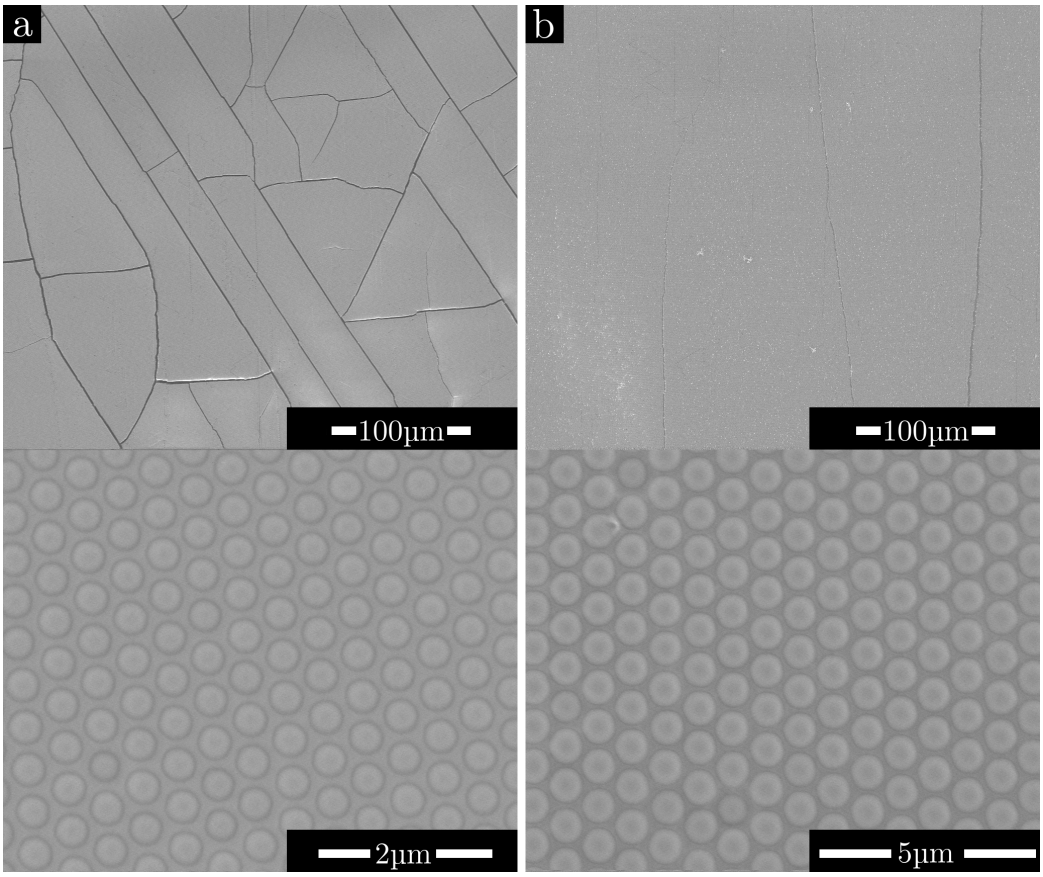

Figure 3.12: Representative SEM images at low and high magnifications of opal composites grown with spheres of a) 490 nm and b) 870 nm in diameter.

rinsed with distilled water and again dried under a nitrogen flux. The samples were left to grow at a temperature of 45°C and relative humidity of 20% and collected after approximately 60 h. Figure 3.12 exhibits the aspect of the composites obtained. As appreciated in Figure 3.12a, good quality crystals were obtained with the low diameter spheres. In particular, crack free regions of areas as high as $6\times10^3\,\mu m^2$ could be observed. In the case of the high diameter spheres, the quality was even better, with areas of the order of $3\times10^4\,\mu m^2$. A statistical analysis was performed from SEM images, to determine the average apparent diameter and the lattice parameter of the structures. Results demonstrated that the composites organized in a close packed form, with the embedded spheres touching each other.

For the inversion of the composites, a comparative study was done between calcination and oxygen plasma etching. Although, as stated in Section 2.4, no significant differences could be appreciated between both processes for

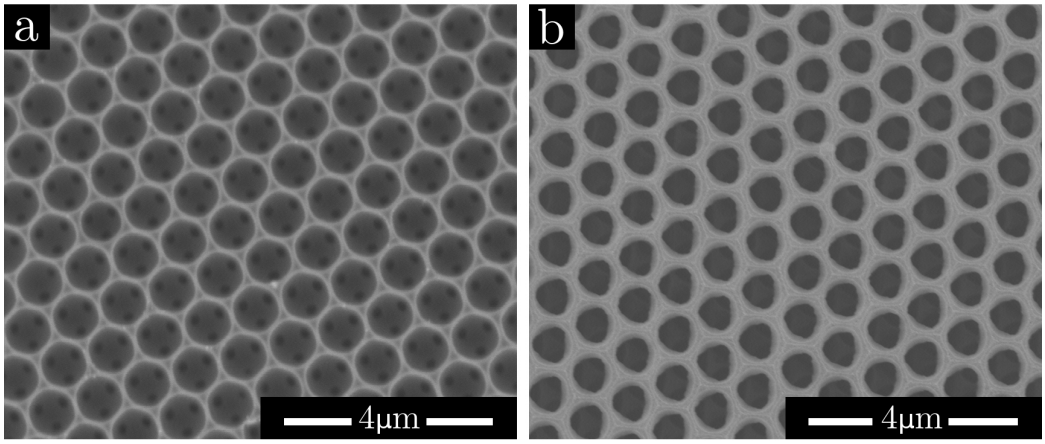

Figure 3.13: Comparison between two pieces of the same composite sample, produced with spheres of $\phi = 870$ nm, after PS removal by a) thermal calcination and b) oxygen plasma etching.

the inversion of monolayers, that was not the case for the three dimensional PCs. The obtained inverse crystals were characterized by SEM. Figure 3.13a shows the typical aspect of a sample after being subjected to thermal annealing (same protocol as presented in Figure 2.2) while Figure 3.13b exhibits a piece of the same sample that was instead subjected to plasma etching. In the later case, the treatment consisted of two cycles of plasma etching of 10 h each. It was observed that, not only the walls of the silica IO obtained by plasma etching were thicker, but also more irregular. This could be explained by the second method leaving some polymeric residues remaining in the IO. Therefore, calcination was in general the technique adopted for the opals inversions.

Figure 3.14 exhibits the SEM analysis of the crystals after calcination, for both the 490nm spheres (Figure 3.14a) and 870 nm (Figure 3.14b). Results showed that the spheres were correctly removed and the crystals preserved their quality. Nevertheless, it was possible to observe cracks widening, due to the fact that the substrate thermal expansion is different from that of the silica opal. Windows interconnecting the spherical voids, at the points where the spheres were initially touching, were also observed. These are characteristic of the IO morphology and was also a hint that the structure was initially in a close packed form. Moreover, the results pointed to an increase of 20% of the apparent diameter of the top layer of spherical voids and a 10% increase of the lattice parameter, after calcination. This effect may be due to mechanical relaxation induced by the thermal expansion and contraction

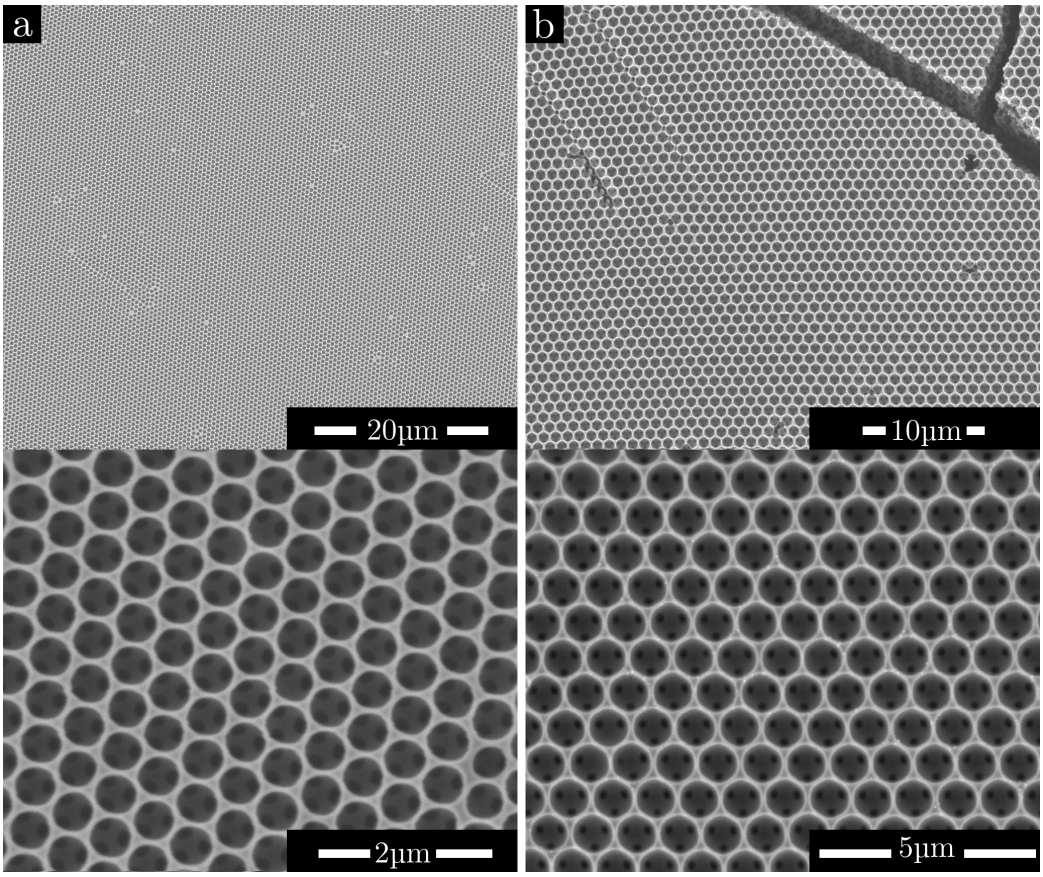

Figure 3.14: Representative SEM images at low and high magnifications of IO grown with spheres of a) 490 nm and b) 870 nm in diameter, after calcination and removal of the sacrificial PS spheres.

during the annealing. Naturally, this aspect must be taken into account when configuring inverse structures for specific spectral ranges.

For doping the crystals with the RE elements, atomic layer deposition (ALD) was used [128]. This technique is similar to chemical vapor deposition, although allowing a much finer degree of control over the quantity of materials deposited. It was performed in a Cambridge Nanotech Savannah S100 system. The selected precursor for erbium was tris(2,2,6,6-tetramethyl-3,5-heptanedionate)erbium(III), which was heated at 160°C, and for ytterbium, it was the tris(2,2,6,6-tetramethyl-3,5-heptanedionate)ytterbium(III), heated at 220°C. Additionally, the selected temperature for the ALD chamber center plate was 300°C. Nitrogen flux was maintained at 20 sccm. Both precursors of the REs were pulsed during 0.01 s (1Er: 3Yb) and made to react with ozone for the deposition. The duration of the ozone pulses was 0.25

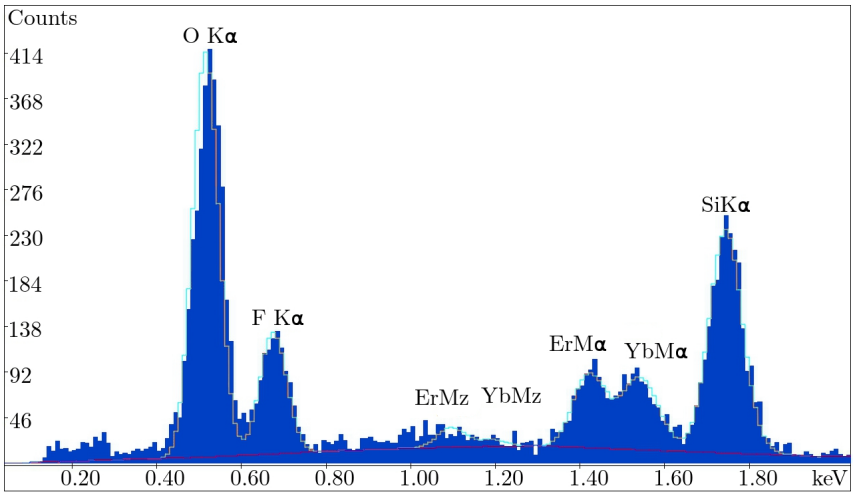

Figure 3.15: Representative energy dispersion X-ray spectrum of an IO ($\phi = 490$ nm), after RE deposition using ALD.

s. Finally, in order to activate the Er emission, the samples were subjected to a second thermal annealing, composed of three ramps: heating at a rate of 10°C/min from room temperature up to 900°C, followed by a plateau of 2 h and a final cooling stage performed at the natural rate imposed by the furnace inertia.

To confirm the doping of the PCs, energy dispersion X-ray spectroscopy was employed. A representative spectrum for one sample produced with spheres of 490 nm is shown in Figure 3.15. In general, the spectra showed the characteristic signals of oxygene, erbium, ytterbium and silicon. It also showed some potential fluor or zinc peak of an unclear procedence (probably some contamination during the deposition procedure). Elemental analysis resulted in an atomic percentage of 33.30% (O), 4.60% (Er), 12.72% (Yb) and 20.05% (Si), in reasonable agreement with the expected ratios.

3.8 Optical characterization

As calculated theoretically and depicted in Figure 3.2, the ΓL gap of an opal composed of PS spheres embedded in silica appears at $(a/\lambda) = 0.56$ and that of a silica IO at $(a/\lambda) = 0.77$. Therefore, for the spheres used in the current work, the gaps should appear respectively at 1238 nm and 895 nm for the samples of $\phi = 490$ nm and at 2197 nm and 1588 nm for those of $\phi = 870$ nm (Table 3.2). The fabrication steps discussed in the previous section were also monitored using Fourier transform infrared spectroscopy (FTIR), in order

sample	(a/λ)	$\phi(490)$	$\phi(870)$
composite	0.56	1238 nm	2197 nm
IO	0.77	895 nm	1588 nm

Table 3.2: Summary of the theoretical spectral positions of the ΓL pseudogaps for a fcc structure, for the two sizes of spheres used in the current work.

to follow the behavior of the referred gaps. Reflectance and transmittance spectra were collected employing a Bruker IFS 66S spectrometer coupled to an optical microscope. Some representative spectra obtained are shown in Figure 3.16.

The position of the gaps could be clearly appreciated as peaks corresponding to maxima in reflectance mode or minima in transmittance. For the composite samples, the agreement between the experimental data and the theoretical expectations was good. For the sample $\phi = 490$ nm (870 nm), the gap was found at 1207 nm (2117 nm). We note that a typical variation of 2% was found in the central wavelength of the peak (λ_{Bragg}) by scanning along different points of the same sample, to check for reproducibility. Therefore, the differences with respect to the values shown in Table 3.2 can be considered within the experimental error. An additional factor that may contribute to this small discrepancy (since the experimental one was systematically smaller than the theoretical calculation) is the refractive index of colloidal silica being smaller than that of bulk silica considered for calculations.

After thermal treatment, the peaks displaced towards the blue region of the spectrum, in agreement with to the predictions. Nevertheless, this displacement was significantly larger than the theoretical one for both sizes of particles. This observation could not be explained by the changes in geometry of the opal since the lattice parameter showed an increase after the annealing, which, if any, would imply a redshift of the peaks. On the contrary, the observations implied an effective refractive index smaller than the initially supposed. This result seems to be plausible considering a more significant porosity increase in the calcinated structure, implying that the silica filling fraction of the calcinated samples was lower than the theoretical 26%.

Finally, we note that after REs ALD, the peaks suffered a slight redshift. This was explained by the increase of the refractive index, due to the presence of the dopant species thus, the increase of material amount. We observe that,

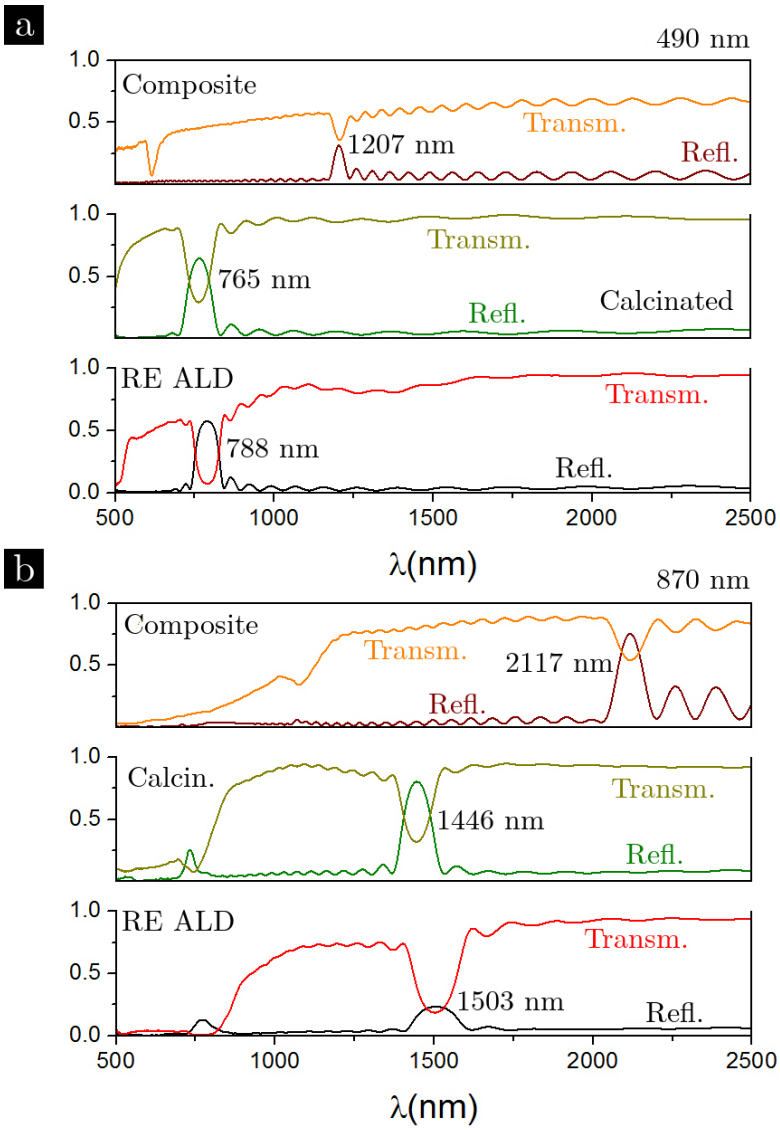

Figure 3.16: Reflectance and transmittance spectra of the samples fabricated with spheres of a) 490 nm and b) 870 nm in diameter at three successive fabrication steps (composite, calcinated and RE-doped by ALD).

as intended, the Bragg peak was centered around 788 nm (1503 nm) for the samples produced with spheres of 490 nm (870 nm) in diameter. Thus, it was demonstrated that the ΓL pseudogap was relatively far from erbium PL spectral region while, for the samples produced with particles of $\phi = 870$ nm, the PL was approximately coincident with the gap border.

3.9 Study of emission in silica inverse opals

Recent results showed evidences of silica IO influencing Er ion emission, by analyzing the 1.5 μm line [129]. Specifically, effects on the PL intensity and on the full width at half maximum of the emission peak were reported. In the current work, we tried to ascertain similar effects in our samples, doped by using ALD, as described in the fabrication section.

The PL of silica IOs, doped with RE using ALD was characterized using the setup explained in Appendix B. Samples were pumpped at $\lambda = 980$ nm which corresponds to an absoprtion band of Yb, which resonantly transfered the energy to Er. Figure 3.17a shows a comparison between the Er^{3+} ion PL embedded in a crystal produced with spheres of 490 nm and one with 870 nm in diameter. As may be appreciated, the characteristic PL peak could be clearly identified, with the maximum appearing at 1532 nm in both cases. The shape of the spectra presented some slight differences. In particular, that of 490 nm showed a more pronounced bump at high energies while, on the contrary, that of 870 nm exhibited a more important contribution for lower energies. Nevertheless, the full widths at half maximum were similar for both crystals - 50 nm and 51 nm, respectively.

Regarding PL lifetime measurements, the two respective examples are exhibited in Figure 3.17b. These curves were collected at the PL maximum wavelength, meaning that the monochromator (Figure B.1) was configured to $\lambda = 1532$ nm in the experiments. The excitation pulse had an approximate duration of 20 μs. Results revealed that the curve for the doped crystals of 490 nm presented an almost monoexponential decay while, on the contrary, the behavior of the PL in the samples of 870 nm showed a non-monoexponential decay. For extracting the characteristic decay times, a preliminary study was performed in order to investigate which kind of decay model [145] could better fit the experimental data. Using the 870 nm curves, the models tested were bi-exponential decay, stretched-exponential decay, lognormal distribution and gaussian distribution. Results are plotted in Figure 3.18. As may be appreciated, the model which minimized the fitting residues was the bi-exponential decay thus, the experimental data were fit using an expression of the form

$$PL(t) = A_1 e^{-t/\tau_1} + A_2 e^{-t/\tau_2}. \tag{3.1}$$

For the samples of $\phi = 490$ nm, the fast characteristic lifetime was $\tau_1 = 0.33 \pm 0.02$ ms while the slow time τ_2 was not defined. For the samples grown with particles of $\phi = 870$ nm, the result of the fittings was $\tau_1 = 0.31 \pm 0.01$ ms and $\tau_2 = 2.0 \pm 0.1$ ms. Comparison of the lifetimes τ_1 revealed

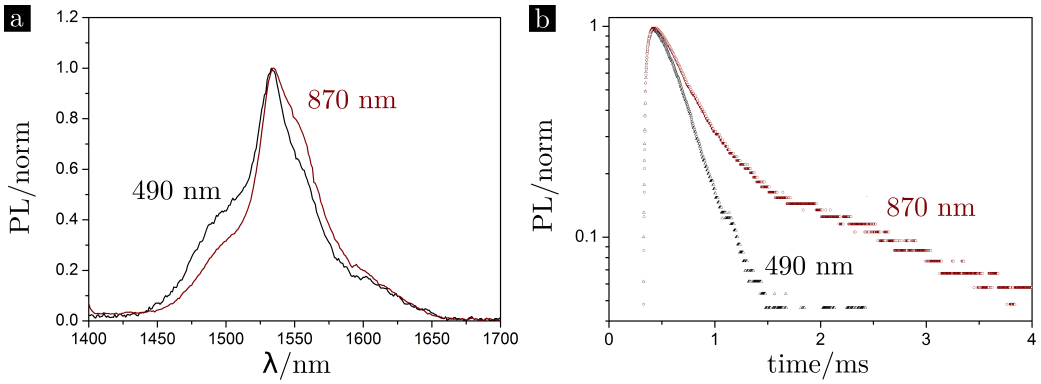

Figure 3.17: a) Normalized PL spectra and b) PL lifetime measurements of erbium ion embedded in silica IOs produced with spheres of 490 nm and 870 nm in diameter.

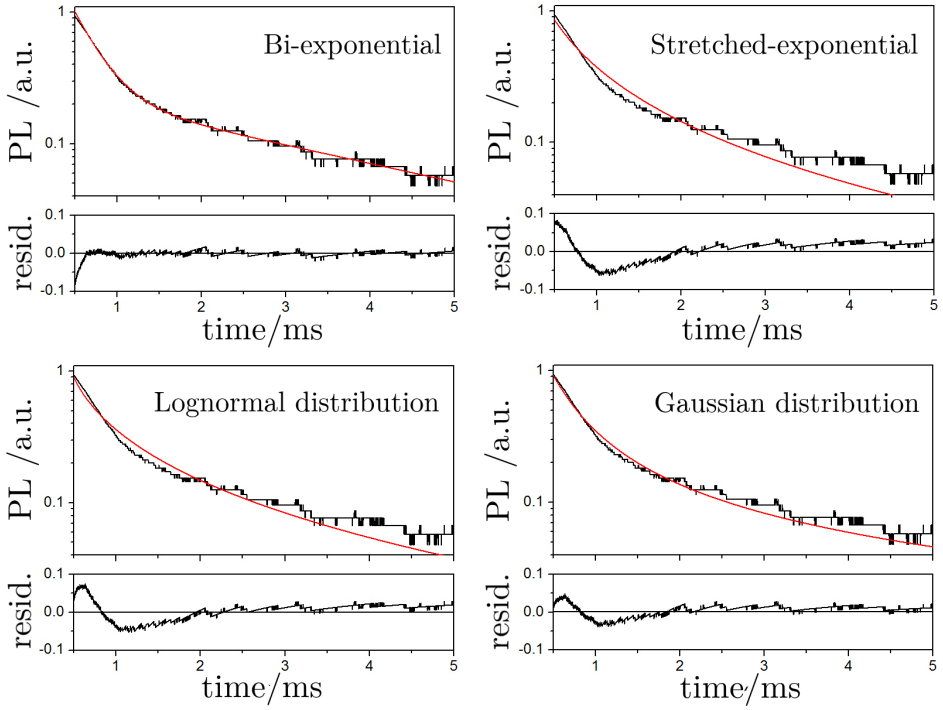

Figure 3.18: Fitting studies for ascertaining which decay model could better fit the experimental data for the PL of erbium incorporated in a silica IO produced with spheres of 870 nm.

ϕ [nm]	τ_1 [ms]	τ_2 [ms]
490	0.33 ± 0.33	0.31 ± 0.01
870	not defined	2.0 ± 0.1

Table 3.3: Fitted life times of the Er^{3+} ion PL, comparing its behavior when embedded in a silica IO with the ΓL gap near the PL or far from it.

a difference of only 6% between the samples with the gap either far from the PL or near it, which was of the same order of magnitude than the one of the fittings uncertainty. Table 3.3 presents a summary of the life times fitted from experimental data.

3.10 Scanning of the pseudogap through Er emission

In an attempt to further conclude about the influence of the ΓL gap in the erbium PL, a representative silica IO, produced with 870 nm spheres, was additionally infiltrated with alumina using ALD. The gap was scanned along the PL peak, in the 1.5 μm region. The infiltration process was monitored using FTIR spectroscopy. Normalized reflectance spectra are exhibited in Figure 3.19a, where the displacement of the Bragg peak towards the red is observed. The evolution of the peak center, as well as of the gap borders (considered as the points at half maximum) is presented in Figure 3.19b. The observed red-shift was consistent with the increase of the effective refractive index of the structure due to the alumina.

Simultaneously with reflectance, the Er PL was also analyzed for each infiltration cycle. PL spectra are presented in Figure 3.20a. Very slight changes were detected on the spectra as more and more alumina was deposited. The most significant aspect seems to be a small relative increase of the high energy bump (at *c.a.* 1500 nm) with respect to the maximum. We hypothesize that this is due to a filter effect induced by the PC [146], although this observation could be also related to local changes in the concentration of Er or Yb or to the change of their chemical environment and not due to any gap influence. In order to clarify this aspect in more detail, the evolution of the lifetimes τ_1 and τ_2 was also studied (Figure 3.20b). As can be confirmed, the

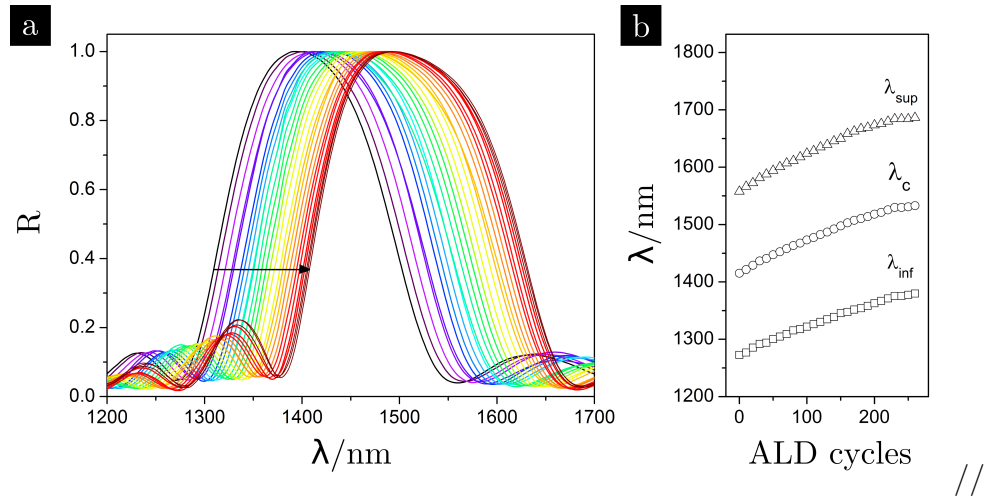

Figure 3.19: a) Evolution of the reflectance spectra of the representative RE-doped silica IO ($\phi = 870$ nm) as alumina was stepwise infiltrated using ALD. b) Evolution of the Bragg peak center and gap borders with the number of alumina ALD cycles.

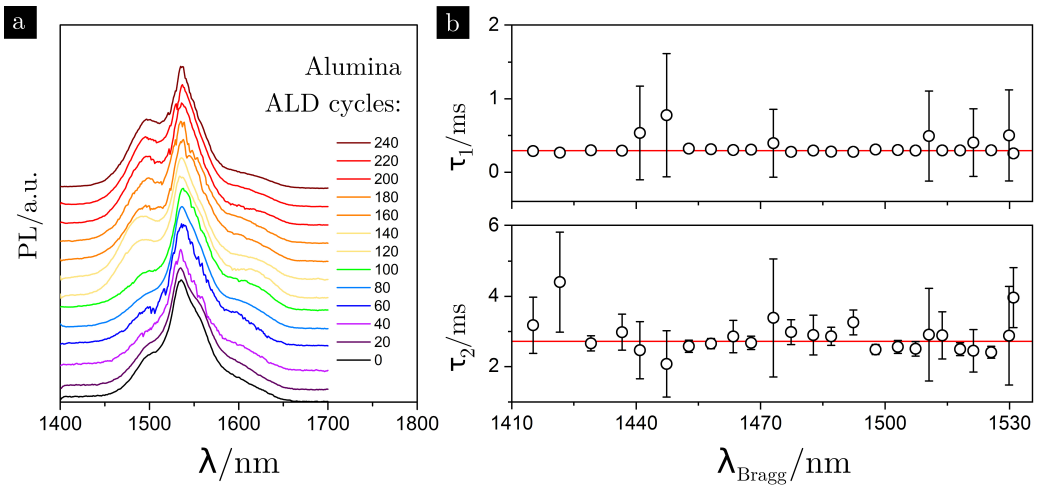

Figure 3.20: a) PL spectra of erbium incorporated into silica IO ($\phi = 870$ nm) as a function of alumina ALD cycles. For clarity, the spectra were vertically displaced. b) Evolution of the characteristic lifetimes τ_1 and τ_2 with respect to the Bragg peak center, as it suffers a redshift due to ALD infiltration.

lifetimes did not present any relevant trend as more alumina was infiltrated and the peak experienced a red shift (τ_1 and τ_2 are plotted against the central position of the Bragg - λ_{Bragg}). These results point out that no significant photonic effects were induced by the presence of the gap.

3.11 Towards the inverse silicon opals

As was seen, the effect of the ΓL PBG of silica IOs was not significant. Alternatively, we wanted to asses the possibility of manipulating the Er luminescence using silicon IOs, with higher refractive index contrast and presenting a fPBG. Therefore, new sets of composites and silica IOs were fabricated, following the same method than before.

After their characterization, the calcinated samples were subjected to the process of magnesiothermic reduction for converting the silica into silicon. The typical procedure used was that described in Section 2.6 for colloidal monolayers. Figure 3.21 presents a representative EDX spectrum of the IOs at this stage. Three characteristic peaks were found, belonging to oxygen, magnesium and silicon. Elemental analysis resulted in atomic percentages of 31.33% (O), 44.04% (Mg) and 21.45% (Si). A carbon contamination was also identified (3.18%). We note that the percentage of magnesium was slightly higher than that of oxygen. This was not expected as, in a stoichiometric reaction, magnesia is composed of equimolar parts of O and Mg. This observation may indicate the formation of magnesium silicide (Mg_2Si) occurring to some extent. In fact, if the molar quantity of elemental magnesium available to react is more than twice that required of SiO_2, besides the reduction of silica, the formation of Mg_2Si according to the chemical reaction

$$4\,\mathrm{Mg}\,(\mathrm{g}) + \mathrm{SiO_2}\,(\mathrm{s}) \rightarrow 2\,\mathrm{MgO}\,(\mathrm{s}) + \mathrm{Mg_2Si}\,(\mathrm{s}) \tag{3.2}$$

also takes place. This was a frequent problem affecting the produced samples. We remind that the quantity of elemental Mg introduced in the reactor was hard to estimate. Therefore, for some of the attempts, that implied a poorly reduced sample (high quantity of silica still present after the procedure, besides magnesia) while, in other cases, an abundant production of Mg_2Si was obtained.

The elemental analysis characterization was repeated after etching with HCl. An example of the typical results obtained is shown in the bottom graph of Figure 3.21. As may be verified, the Si Kα peak at 1.74 keV was still visible, that of magnesium became only residual and that of oxygen suffered a considerable decrease (comparison of relative intensities between peaks). The calculated atomic percentages in this case were 4.45% (O), 0.45% (Mg), 95.10% (Si). Although a small oxide contamination was still present, the results showed that the protocol used was effective for achieving a material exclusively composed of silicon.

Further inspection of the samples was performed using SEM. Figure 3.22 shows representative examples of the images obtained. As may be verified in Figure 3.22a, the IO structure could be correctly achieved. Nevertheless,

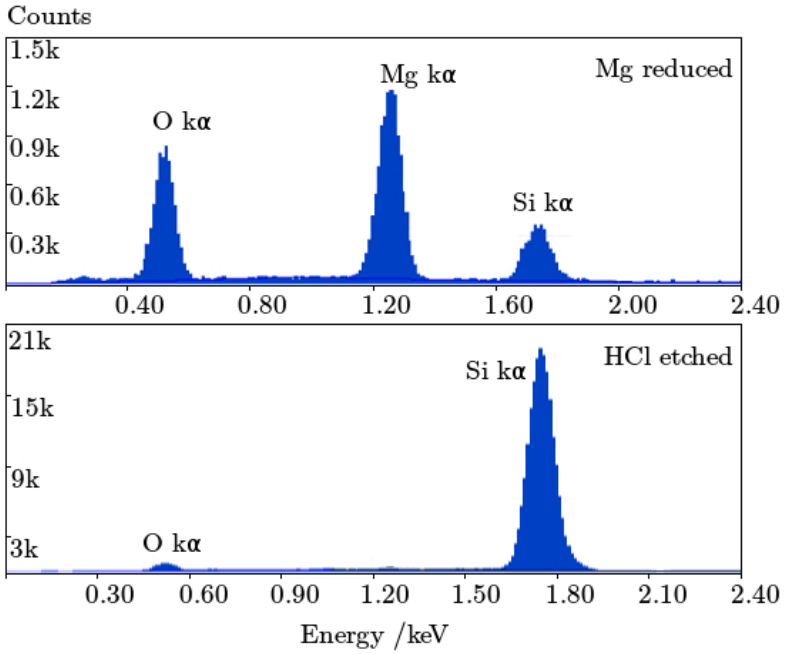

Figure 3.21: Energy dispersion X-ray spectra of an opal after magnesiothermic reduction (top) and after later chemical etching with HCl (bottom).

lower magnification images such as those exemplified in Figure 3.22b-d revealed a significant amount of defects and a considerable variability presented by the crystals. In fact, other kinds of domains orientation were frequently observed (Figure 3.22b). Additionally, cracks possibly derived from mechanical deformations during the thermal annealings drastically limited the area of the small crystallites available (the average area was of the order of 160 μm^2). Figure 3.22d exemplifies another typical problem related to the fabrication, the loss of adhesion of the IO to the substrate, leading to liftoff and loss of the crystallites.

According to the discussion above, the protocol described until now for the fabrication of the crystals was effective and it was possible to obtain small regions of silicon IOs. In spite of this, the samples obtained were, in general, composed of porous silicon, due to the intrinsic nature of the fabrication. For this reason, it was expected that the position of the photonic gaps was not exactly that determined by theory. Figure 3.23 shows a summary of the reflectance spectra evolution of the sample for the intermediate fabrication steps used towards the final silicon IO. These spectra are representative but naturally, the variability pointed out previously was also reflected significantly on the optical properties and on the position of the Bragg peak center (from sample to sample and even from different areas in the same sample).

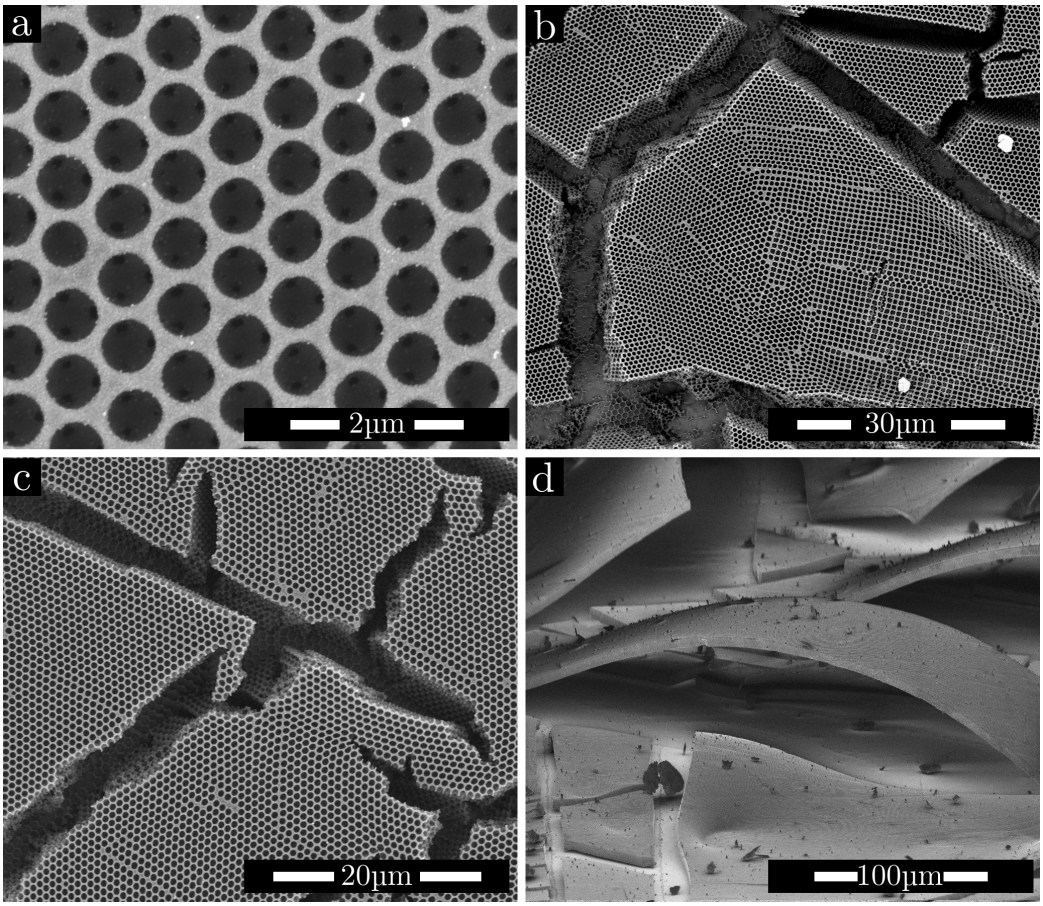

Figure 3.22: Representative SEM images of silicon IOs at different magnifications, obtained after magnesiothermic reduction of silica IOs and later chemical etching with HCl. Image in d) shows a tilted view.

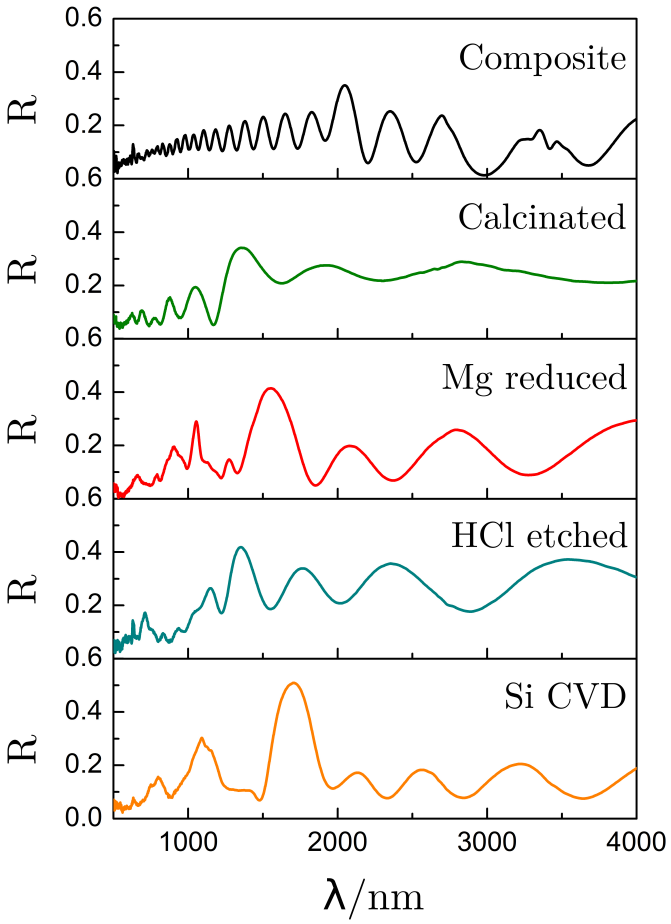

Figure 3.23: Evolution of the reflectance spectrum of the crystal at every step of the fabrication procedure: composite opal, calcinated sample, magnesiothermic reduced crystal, after chemical etching with HCl and finally after additional Si infiltration with CVD.

The pseudogap was found at $\lambda = 2045$ nm for the composite opal, which agreed with previous results (Figure 3.8) and theoretical calculations (Figure 3.2). The slightly smaller value obtained experimentally with respect to the theoretical one, may be explained by the smaller refractive index of colloidal silica compared to bulk silica, as was already stated. After calcination, the Bragg displaced to $\lambda = 1356$ nm, after the magnesiothermic reduction showed a redshift to $\lambda = 1553$ nm and finally, after the removal of magnesium oxide with HCl etching, a blueshift was again observed towards $\lambda = 1348$ nm. These displacements of the pseudogap are explained by either a decrease of the effective refractive index of the structure (blueshifts) or an increase (redshifts).

In order to increase the refractive index of the structure and to decrease the porosity of the inverse matrix and shift the photonic gaps to the aimed spectral region, the crystals were further infiltrated using silicon CVD. As in previous works by Blanco *et al.* [143], disilane (Si_2H_6) was the chemical precursor used for the silicon deposition. Disilane, which is a gas at room temperature, was condensed in the substrate by cooling it with liquid nitrogen. Silicon was obtained by its subsequent dissociation with the help of thermal heating. Other silanes might be formed as intermediate species, but the chemical equation which translates the net process is

$$Si_2H_6\,(l) \rightarrow 2Si\,(s) + 3H_2\,(g). \tag{3.3}$$

The temperature program more commonly used for the dissociation was composed of three ramps. In the first one, temperature increased up to 325°C in 30 minutes. In the second, T was maintained constant at 325°C during 12 h. Lastly, T decreased at the natural rate. Higher temperatures may be used for a more fast process although at low t, the rate of decomposition of the disilane is slower, which enhances the penetration into small IO pores.

As may be appreciated in the last plot of Figure 3.23, the Bragg peak displaced towards low energies, in line with the increase of n_{eff}, becoming centered at $\lambda = 1705$ nm. Additionally, the high energy peak, which corresponds to the fPBG, became much more pronounced than in the previous structures, centered at $\lambda = 1091$ nm. This behavior was the expected one, although the silicon IO was probably too porous so that the high energy peak was still far from the aimed 1550 nm region.

3.12 Attempts at fabricating silicon IOs with a fPBG at 1.5 μm

The fabrication procedure corresponding to all the steps indicated in Figure 3.23 was attempted several times. Figure 3.24 exhibits two examples of the optical characterization (reflectance and transmittance spectra) for two samples subjected to the same processing. Different curves in each graph correspond to different areas in the samples. As may be verified, it was possible to produce a silicon IO with the gaps near the aimed regions of interest, although not perfectly tuned with the theoretical expectations ($\lambda = 2587$ nm for the ΓL pseudogap and $\lambda = 1552$ nm for the high energy band). For sample A in Figure 3.24a, the pseudogap was found at an average position of $\lambda = 2277$ nm and the high energy one (fPBG) was observed at $\lambda = 1435$ nm. In the case of sample B, the position of the bands was $\lambda = 1792$ nm

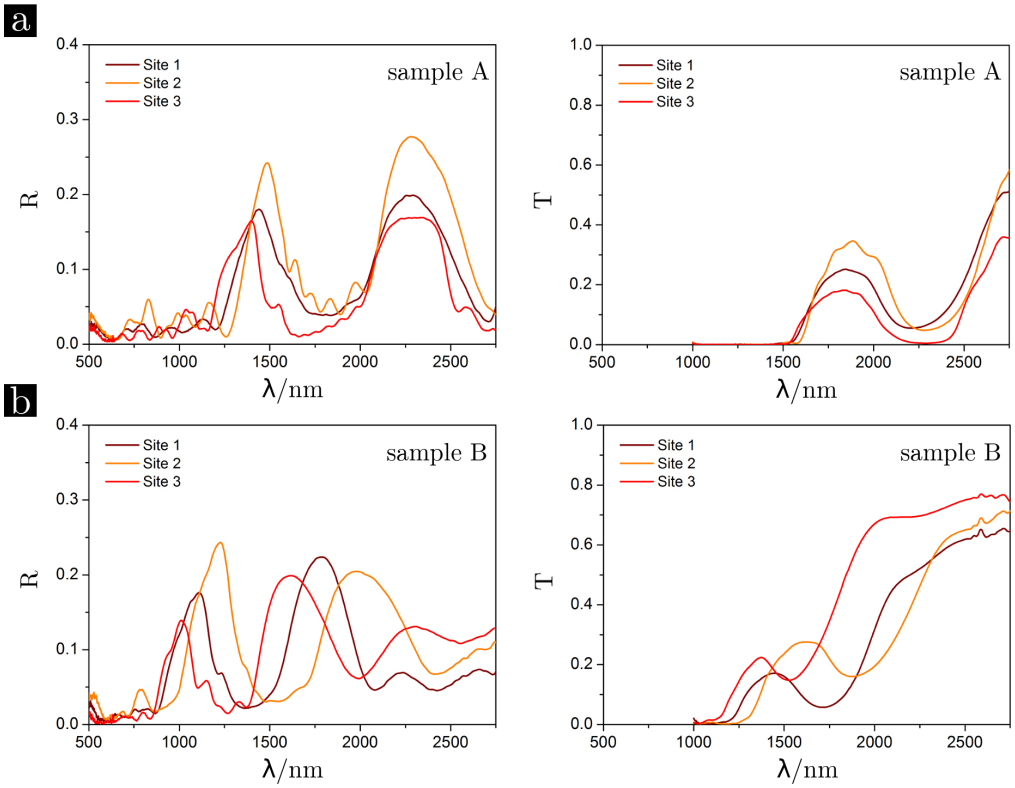

Figure 3.24: Reflectance and transmittance spectra for two different samples subjected to the same processing, aiming at the fabrication of silicon IO with the fPBG in the region of $\lambda = 1.55$ μm.

and $\lambda = 1103$ nm, respectively. These examples demonstrate once again the variability of the grown silicon IOs. In fact, standard deviations of the order of 20% were typically obtained in the position of the gaps. Furthermore, the intensities of reflectance maxima (< 0.2) and the relative transmittance minima to maxima ratio obtained also pointed out to an important scattered component ($S = 1 - T - R$), demonstrating the low quality of the crystals achieved.

3.13 Conclusions

In summary, attempts carried out for fabricating co-doped silica composite opals by coassembly in one step were non-effective. Due to the presence of the additional RE ionic species, the stability of polymeric particle colloids was dramatically affected. If flocculation is to be avoided, small quantities

of dopants must be used but, even in those conditions, the presence of the salts inhibited the crystallization of the sub-micron spheres. This way, only amorphous composites are obtained.

On the contrary, the second approach investigated, in which the silica IOs were initially grown and then doped with REs by using ALD, was effective for fabricating the initially proposed photonic system. Characteristic Er emission was observed in the infrared region, near 1.5 μm. Nevertheless, comparison between samples designed to present the ΓL pseudogap far from the PL and those with the gap very near it did not reveal clear photonic effects derived from the periodicity. This fact was possibly due to the low refractive index contrast of the structure, which does not change the photon density of states significantly. Probably due to the same reason, no significant changes could be either observed in the PL lifetimes of an inverse crystal, when it was stepwise infiltrated with alumina, which displaced the pseudogap through the PL peak, in a very controlled way.

Further efforts were performed towards the fabrication of silicon IOs with a fPBG centered in the spectral region of $\lambda = 1.55$ μm were presented. Such crystals would be expected to have a higher impact on the manipulation of trivalent erbium ion emission. The strategy used to fabricate these crystals was based on vertical deposition and co-assembly to grow composite opals, calcination of the sacrificial PS spheres, magnesioreduction of the silica and chemical etching of the magnesia and, finally, additional silicon CVD infiltration for tuning the spectral position of the gaps.

These objectives were only partially fulfilled. Whereas it was possible to obtain PCs using the fabrication method proposed, no IOs could be achieved with the fPBG exactly centered at $\lambda = 1.54$ μm. The crystals obtained were plagued with defects that derived from the high number of fabrication steps required. Problems such as the intrinsic variability associated with the growth of the composites (inhomogeneous number of layers, polydomain structure and different orientations obtained), cracking due to thermal annealings, curving of the crystallite borders, variations in the silica reduction degree leading to inhomogenities in the refractive index, loss of adherence of the crystallites to the substrate and deposition of particles during the silicon CVD constituted a number of factors that limited the final quality of the samples and dramatically hindered their further application in PL studies.

Part II

Multifunctional exploration of photonic media using programable shape memory polymers

4 Thermoresponsive shape-memory structures

In this chapter, thermoresponsive photonic structures are introduced. They consist of hexagonal arrays of nanobowls imprinted on the surface of a shape memory polymer, fabricated by a process of replica molding. The as produced samples are characterized from the structural and optical points of view. Results show that the proposed elastomers retain shape memory properties which are also reflected in the behavior of the nanopattern. It is demonstrated that it is possible to program the lattice parameter of the system or to temporarily erase the surface pattern.

4.1 Introduction

Despite SMPs having been extensively explored in bulk form [56], the investigation of the SME at the micro/nano scales is still in its infancy [147]. Furthermore, the use of SMPs for producing nanostructures with photonic functionality has been very limited. In general terms, photonic structures refer to patterned media with features in a typical size of the order of, or below, visible or near-infrared radiation wavelengths. These features translate into a modulation of the refractive index that causes a strong radiation/matter interaction and significantly affects the electromagnetic density of states. In this context, strategies for achieving periodic structures exhibiting SME are highly desirable, in order to develop novel multifunctional materials and optical devices.

Contrary to SMPs, elastomers have been more employed in photonics although almost exclusively to take advantage of their elastic properties. For instance, some reports have demonstrated their use in the fabrication of elastic transmission gratings or lenses with real time control of the periodicity or the

focal length, respectively [148]. They have been applied to the preparation of compression sensitive inverse opals which allow the mechanical tuning of the photonic bandgap position [144]. Elastomers have also played a fundamental role for studying color tunable photonic crystals (PCs) [15, 149], whose lattice parameter might be controlled by deformation (mechanochromic effect) or elastomer swelling [150]. An equivalent approach was proposed for the development of tunable phononic crystals [151]. Another active area of research concerns flexible systems implemented, for instance, as UV-filters [152, 153] and light emitting diodes or displays [154].

4.2 Fabrication of the templates

The procedure for the fabrication of the colloidal monolayers used as templates for the subsequent replica molding imprinting was similar to that previously described in chapter 2. For convenience, we briefly detail below some particular points which were adapted to the present case. The spheres used were composed of polystyrene (PS) and purchased from Thermo Scientific (polydispersity around 3%). Several particle diameters were tested for fabricating the crystals. Colloids with a final concentration of 0.5 wt% were prepared by dispersion of the commercial suspensions (at a concentration of 10 wt%) in double distilled water (18 MΩ). As substrates, microscope glass slides were cut to the appropriate length, carefully cleaned and hydrophilized in a chromic mixture. Afterwards, they were assembled into an evaporation cell (Figure 2.1). The substrate was glued to the lower slide with double-sided scotch tape. The upper slide was equally hydrophilized and mounted in the cell forming an angle of 2° with the substrate. Clamps were attached in order to secure all the components. Finally, a small quantity of colloid (typically 100 μl) was inserted between the upper slide and the substrate. The resulting cells were left to evaporate for approximatelly 24 h in a climatic chamber with controlled temperature (20 °C) and relative humidity (90 %).

4.3 Synthesis of PDDC-HD pre-polymer

Polydiolcitrates, such as the one selected for the present work, were first described by Ameer and co-workers as biodegradable elastomers produced upon thermal condensation of citric acid and aliphatic diols [155]. More recently, they were produced as shape-memory thermoresponsive polymers [48], which was achieved by both incorporating a more hydrophobic diol (1,12-dodecanediol, DD) and increasing the mol ratio of hydroxyl to carboxyl

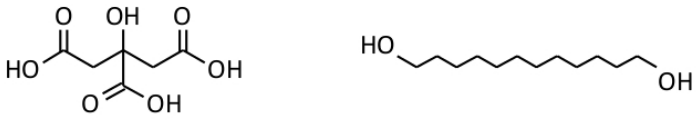

Figure 4.1: Molecular formula of the monomers used for preparing the shape memory pre-polymer - citric acid (left) and 1,12-dodecanediol (right).

groups in the reaction mixture. The obtained networks include covalent netpoints responsible for the permanent shape and hydrophobic microdomains (either pre-polymer or DD-rich domains), physically cross-linked by intermolecular hydrophobic interactions, as switch structures to fix the temporary shape. Interestingly, as far as we know, the applicability of polydiolcitrates in the fabrication of photonic nanostructured systems has not been reported in the literature before.

The synthesis of the hydroxyl-dominant poly(1,12-dodecanediol-co-citrate) prepolymer (PDDC-HD prepolymer) was carried out according to a previously reported protocol [48]. Briefly, citric acid and DD (molar ratio 4:3 of hydroxyl to carboxyl groups) were melted at 165 °C for 10 min, in a round bottom glass flask. Subsequently, the temperature was decreased to 140 °C and the condensation reaction maintained at that temperature for 1 h so that a liquid prepolymer solution was obtained. Figure 4.1 illustrates the chemical structures of the precursors employed. During the thermal treatment, the polymerization of the chains occurs by esterification of the carboxyl groups in citric acid and the hydroxyl groups in the DD molecules. In the present system, the reaction is intentionally interrupted at an early stage so that there is still a significant amount of prepolymer and DD rich domains responsible for the shape memory properties.

For the chemical characterization of the PDDC-HD prepolymer, its ^{1}H-NMR spectrum was recorded at room temperature by using a Bruker spectrometer DRX-500 at 500 MHz. DMSO-d_6 was used as a solvent (δ: 2.5 ppm). The chemical shifts in parts-per-million (ppm) were referenced relative to tetramethylsilane (TMS, 0.00 ppm) as the internal reference. The assignments obtained are as follows. ^{1}H-NMR (500 MHz, DMSO-d_6, δ): 1.3-1.5 ppm (a-c, 20H; -CH_2-) from 1,12-dodecanediol; 2.6-2.9 ppm (d, 4H; -CH_2-) from citric acid; 3.4 ppm (e, -OH) from non-reacted hydroxyl groups in 1,12-dodecanediol and citric acid; 4.0 ppm (f, 4H; -O-CH_2-) from 1,12-dodecanediol; and 4.3 ppm (g, 1H; -COOH) from non-reacted carboxyl groups in citric acid. The results obtained agreed with those previously reported for this type of elastomers [48] and confirmed the expected dominance of hydroxyl to carboxyl groups (mol ratio of DD to citric acid: 1.50) (Figure 4.2).

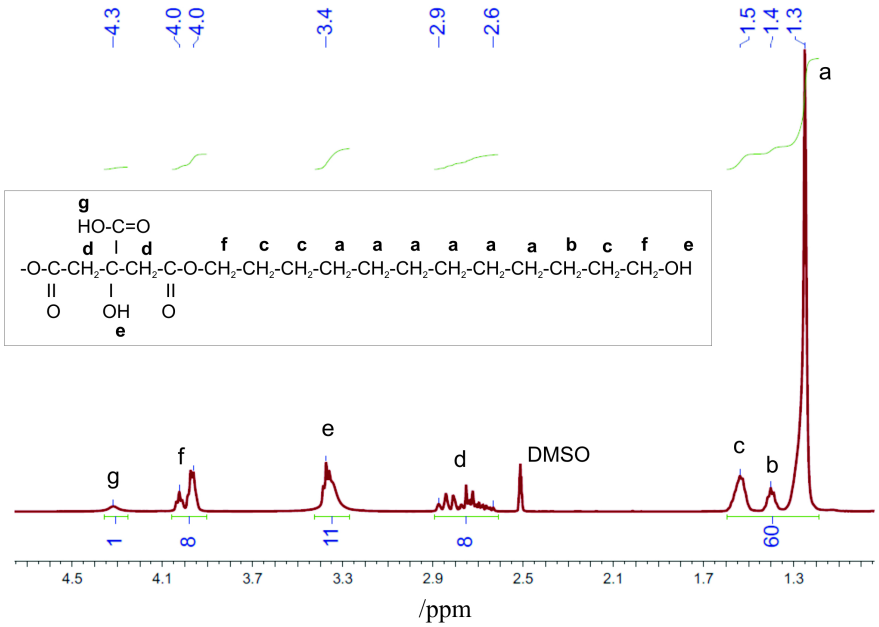

Figure 4.2: Representative ^{1}H-NMR spectrum of the PDDC-HD prepolymer. The inset identifies the labels adopted for the chemical shifts characteristic of the different types of groups.

4.4 Pattern imprinting on the SMP surface

The procedure used for patterning the surface of the PDDC-HD elastomer was based on soft-lithography [156] or, more accurately, on the set of techniques usually denoted as replica molding [157]. It consisted of the steps illustrated in the scheme of Figure 4.3. As at room temperature the PDDC-HD prepolymer is a solid, it was heated at 90 °C (above its transition temperature - T_{trans}) for approximately 10 min, so that a highly viscous and transparent liquid was obtained. In this state, it was spread over the template (step 2) - as templates, most of the work was done using colloidal monolayers composed of PS spheres of 870 nm in diameter, fabricated as described in section 4.2. PS spheres were intentionally selected in order to avoid polymer cross-linking with the mold, that could impair its posterior removal. Afterwards, the sample was placed in an oven and cured at 90 °C for 12 h (step 3), thus inducing the cross-linking between polymeric chains. The curing must be stopped before the complete cross-linking occurs, otherwise the polymer will lose the shape-memory feature. Finally, the elastomer was carefully peeled-off from the monolayer, while still warm, taking advantage of its elastic properties (step 4).

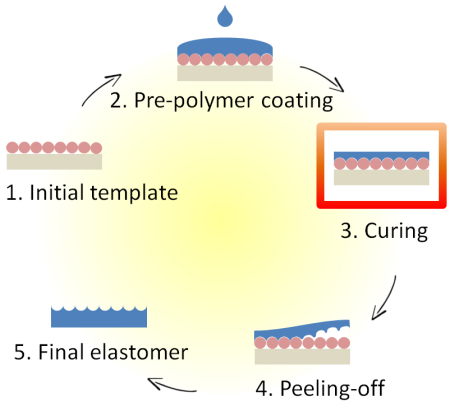

Figure 4.3: Scheme of the protocol followed for the pattern imprinting in the PDDC-HD elastomer surface.

4.5 Microstructural characterization

During cross-linking, the surface of the PDDC-HD polymer acquired the permanent shape determined by the colloidal crystal structure, as confirmed by atomic force microscopy (AFM) studies. The samples were analyzed in a microscope Bruker Nanoscope III A, equipped with a FESP tip and working in tapping mode. Figure 4.4 exhibits a representative 3D reconstruction of the elastomer surface at two different magnifications. These results confirmed that the spheres did not remain attached to the PDDC-HD but, on the contrary, rested on the original glass substrate. As may be observed, the elastomer surface consisted of a homogeneous hexagonal array of nanobowls of an average depth of 140 ± 30 nm. It is possible that the hydrophobic nature of the PS spheres contributed to repeal the elastomer from embedding deeply into the monolayer, thus explaining why the groove's depth obtained was of the order of 140 nm instead of the expected 435 nm, should the elastomer have reached at least the equator of the spheres. Another factor that may explain such a low depth value may be polymer shrinking during curing at high temperature.

Additionally, the patterns were characterized using SEM. Samples were mounted on stubs with carbon tape and visualized in a FEI NovaNano SEM 230 field emission microscope. Images such as that presented in Figure 4.5a demonstrated that very extensive areas of PC monodomain (i.e., regions where the orientation of the hexagonal lattice is constant) could be achieved. It was possible to observe monodomain areas at least as extense as 4500 μm^2 (roughly 8×10^3 nanobowls).

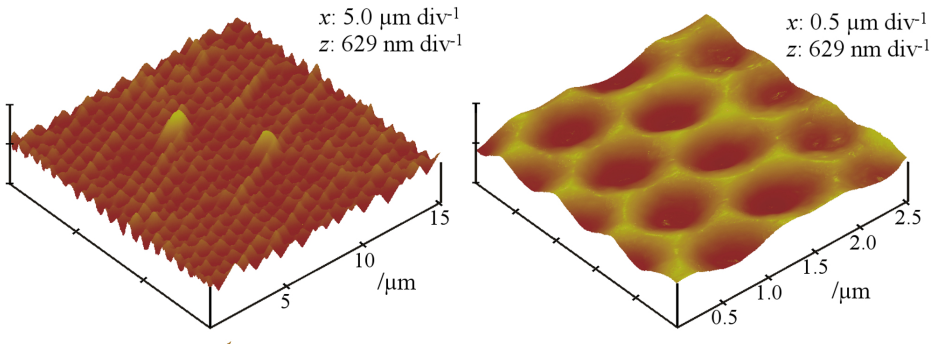

Figure 4.4: AFM 3D surface reconstructions of the nanopatterned elastomer at two different magnifications. These images demonstrate the successful imprinting of the nanobowls in the PDDC-HD surface.

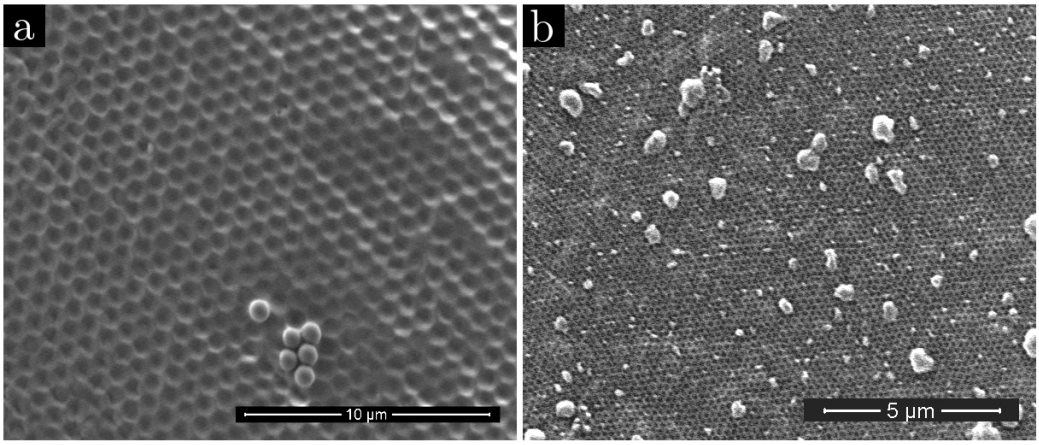

Figure 4.5: a) Topography of a representative region of the patterned PDDC-HD elastomer surface (PS spheres with ϕ = 870 nm) as observed by SEM. b) SEM image of a nanostructured PDDC-HD elastomer surface produced by replica molding from a colloidal monolayer fabricated with PS spheres of 200 nm in diameter.

We would like to note that the replica molding protocol was also suitable for templates composed of spheres of other diameters, as exemplified in Figure 4.5b for ϕ = 200 nm. Nevertheless, the sample in this case was much more inhomogeneous pointing out that an optimization of the fabrication techniques would be desirable if such small sizes are required for applications. The results presented in the rest of the chapter concern samples produced with spheres of ϕ = 870 nm.

4.6 Thermal characterization

Thermal characterization of our elastomers was carried out in order to confirm the presence of thermal transitions and to determine their characteristic temperatures. This information is essential in view of a possible implementation of patterned PDDC-HD as a thermoresponsive optically functional material. Modulated differential scanning calorimetry (mDSC) studies were performed using a Discovery DSC Calorimeter (TA Instruments). The samples were cooled to -60 °C, held for 5 min and then ramped from -60 °C to 75 °C at a rate of 2 °C min^{-1} (modulation amplitude ±2 °C and frequency 60 s^{-1}). As revealed in the thermograms obtained (Figure 4.6a), surface-nanopatterned PDDC-HD displayed two thermal transitions, one at *ca.* -4 °C corresponding to a glass transition and the other near 30 °C, corresponding to a melting transition. The later one is the responsible for the SME and it is usually labeled as T_{trans}. Above T_{trans}, the polymer transits to a rubber like state in which the degree of cross-linking and hydrogen bonding controls the elasticity of the network. The obtained results are in good agreement with previously reported values for PDDC-HD [48, 155].

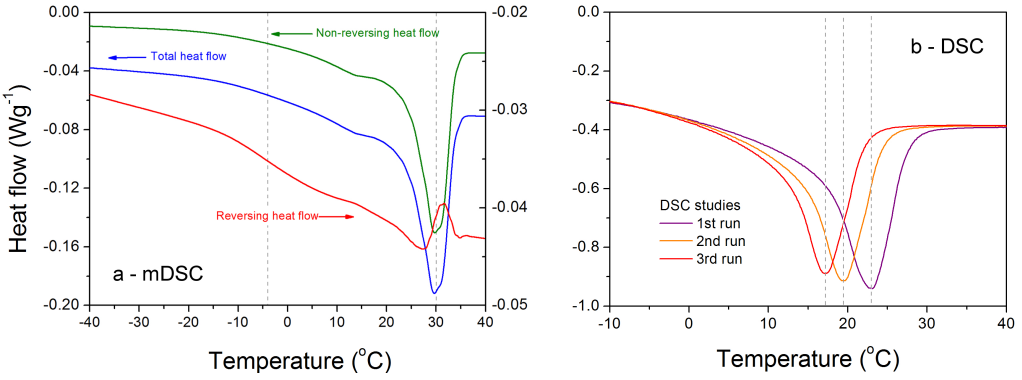

Figure 4.6: Thermal characterization of the PDDC-HD elastomers as obtained by a) mDSC and b) DSC. Endothermic processes are plotted in the negative part of the vertical axis.

Additional differential scanning calorimetry (DSC) studies were made using a DSC Q-100 calorimeter (TA Instruments). In this case, the samples were exposed to an initial isothermal segment at 200 °C, held for 10 min, followed by a cooling segment from 200 °C to -40 °C at 40 °C min^{-1}, and then ramped from -40 °C to 200 °C at 10 °C min^{-1}. Three heating-cooling cycles were run. From these DSC analysis (Figure 4.6b), it was not possible to identify the glass transition. Nevertheless, valuable information was obtained with respect to the melting transition. In fact, comparing the first run from

both mDSC and DSC, a significant difference in the melting temperature was observed. This discrepancy was likely related to two factors. On the one hand, the rates of heating used for both measurements were different and, therefore, the measurements obtained could not be quantitatively compared. On the other hand, the initial heating of the sample at 200 °C and subsequent isothermal segment in DSC studies surely contributed to increase the cross-linking degree of the polymeric network. In this sense, further cooling/heating DSC runs induced a non negligible effect on the elastomer cross-linking that clearly correlated with a decrease of both the melting temperature (23, 19 and 17 °C in successive runs) and the maximum transferred heat. DSC results draw attention to an important issue that must be considered when processing these materials for applications that is polymer aging. As polymer cross-linking relies on condensation reaction that occur spontaneously even at room temperature, although kinetically favored by temperature, heating the polymer (e.g. for DSC studies as well as for shape programming) and its simple storage increases its cross-linking degree, then reducing its shape memory properties.

4.7 Optical characterization

The visual aspect of a representative sample of nanostructured PDDC-HD is shown in Figure 4.7, both below and above T_{trans}. As may be appreciated, the transition could be monitored additionally via the optical properties of the polymer. The opaqueness characteristic of its glassy state at low temperature, caused by the scattering of light from the solid non-cross-linked micro-domains of pre-polymer and DD, gradually disappeared as the material transitioned to the rubbery state. In this state, the micro-domains melt giving rise to a significant increase in transparency.

We further explored this thermally-induced phenomenon by total optical transmittance spectroscopy measurements (Figure 4.8). A small disk of PDDC-HD (2.5 mm-thick) was heated at 90 °C for 10 min and then allowed to cool down at its natural pace while monitoring simultaneously the temperature and the total transmittance. Spectra were collected from 90 °C to 23 °C with an integrating sphere fiber-coupled to an Ocean 2000 compact spectrometer. The temperature was monitored in parallel with a thermocamera Fluke Ti10. As shown in Figure 4.8a, at low temperature, the spectral transmittance of the sample exhibited no anomalies, only a positive slope was observed as a function of wavelength, due to Rayleigh scattering. At high temperature, as scattering was diminished, the spectral response became almoust flat. Results for the wavelengths $\lambda = 532$ and 633 nm are presented in

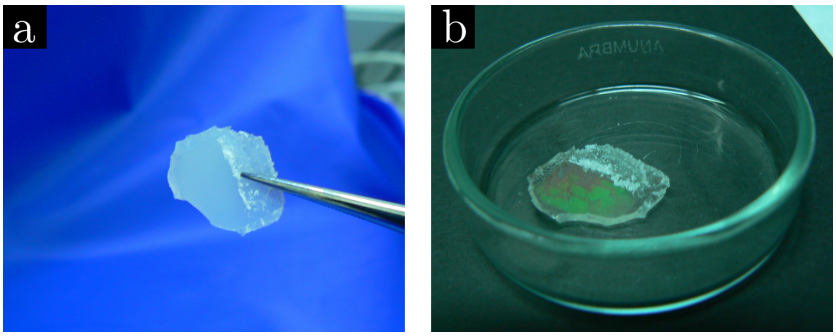

Figure 4.7: Visual aspect of the surface-nanopatterned PDDC-HD elastomer a) below T_{trans} - 21 °C - and b) above it - *c.a* 50 °C.

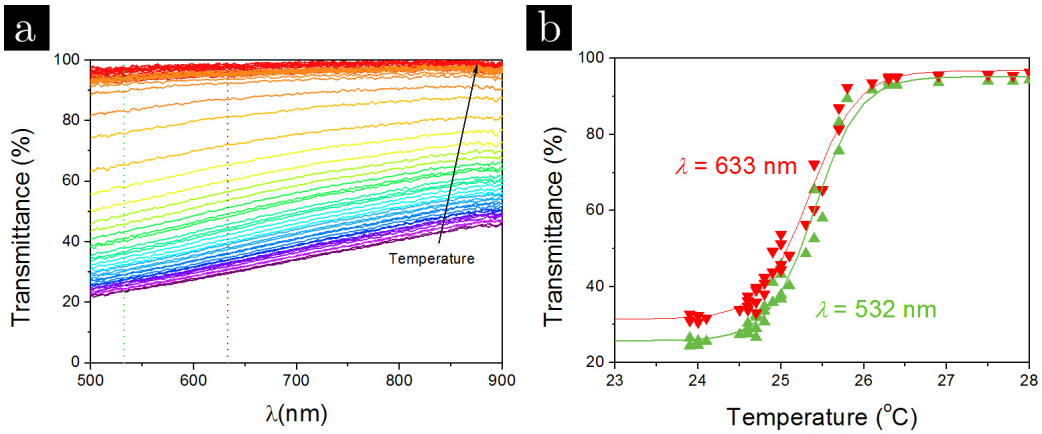

Figure 4.8: a) Temperature dependence of the total optical transmittance of the sample. b) Particular behavior for wavelengths $\lambda = 532$ and 633 nm, underlining the change in transparency characteristic of the transition.

Figure 4.8b. From 70 °C to 26 °C, a constant plateau in which the transmittance was on the order of 95 % was observed. As the temperature decreased below 26 °C, the transition was confirmed by a decrease in transmittance of *ca.* 70 % (final sample transmittance 25–31%). Rayleigh scattering also explains the larger transmittance difference below the transition than above, for both wavelengths. This property is of considerable interest since it supports the applicability of PDDC-HD as a thermo-optical trigger (i.e., a device able to transmit light only above a particular temperature threshold).

4.8 Grating programing

Tailoring of materials towards the development of thermoresponsive optical systems has attracted considerable interest. On one side, materials without SME have been investigated for thermochromic effects (e.g. the fabrication of inverse opals with demonstrated bandgap dependence on temperature [158]). A recent work described novel elastomeric crystalline films with triple stimuli response to strain, light and temperature [159]. On the other side, the full advantages of SME are starting to be explored in the design of photonic devices. Davies *et al.* reported on a chiral-nematic polymeric network presenting SME applied into manufacturing an optical temperature sensor, which changed color as the original shape of the material was restored above a certain temperature threshold [160]. The SME was also the driving mechanism that enabled Xie and co-workers to develop metallic wrinkle membranes exhibiting structural color [161, 162]. Rogers *et al.* reported on the exploration of SMPs towards the fabrication of micro-optical devices or PCs with reversible and programmable characteristics [163]. By using interference lithography, Yang and colleagues developed membranes with programmable color switching [162]. In comparison to this previous work, our strategy for the exploration of SME photonic nanostructures presents important advantages regarding fabrication techniques, due to the use of colloidal crystals as templates. Since these are fabricated with monodisperse particles which are available in a wide range of diameters, an increased control over the final structure and lattice parameter could be achieved. Further, our method is straightforward and does not require complex or expensive equipment.

Light diffraction was used for systematically studying the possibility of programing the sample towards the development of thermoresponsive optical gratings with shape-memory. The diffraction images were acquired with the home-built setup illustrated in the scheme of Figure 4.9. A flip-flop mounted mirror (FF) allowed the selection of the working wavelength (λ = 532 or 633 nm, emitted from either a diode or a HeNe laser, respectively). The

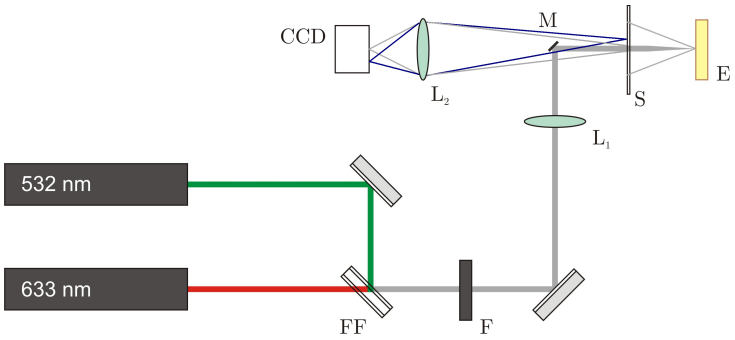

Figure 4.9: Scheme illustrating the optical setup used for collecting the images of the diffraction patterns.

beam was attenuated with a neutral density filter (F) not to shine too much power on the grating. Lens L1 focused the light on the sample (E) while the mirror M deviated the optical path 90 ° enabling a more convenient spatial configuration. The diffracted beams from the elastomer were then projected into the screen (S), positioned 25 mm apart. The screen was composed of semi-opaque paper with a printed scale. Finally, the lens L2 projected an image of the screen in a CCD camera (Allied Vision Technologies, model Guppy), which allowed the digital capture of the images and their posterior analysis. The diffraction angles could be determined from simple geometrical calculations and measuring the distances between the center of the diffraction figure and the diffraction spots.

λ	θ_d	θ_{th}
[nm]	[deg]	[deg]
532	44.9 ± 0.6	44.9
633	57.1 ± 0.8	57.2

Table 4.1: Comparison between the experimental angle (θ_d) described by the diffracted beams and the prevision from the theoretical model (θ_{th}), for the patterned PDDC-HD elastomer at the initial stage (i in Figure 4.10) and for two different wavelengths.

First, the angle of diffraction (θ_d) was measured for the sample at its initial state (permanent shape). The results obtained and their comparison with the theoretical model (see Appendix D) are presented in Table 4.1. As

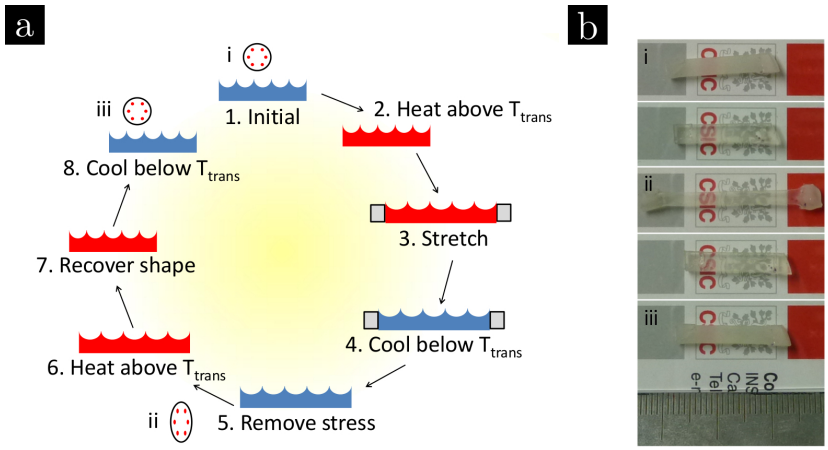

Figure 4.10: a) Scheme of the protocol followed for studying the lattice parameter programing of the patterned PDDC-HD elastomers. b) Photographs of the sample in different stages of the programming cycle: initial (i), deformed and cooled (ii), and cooled down to room temperature after shape recovery (iii). Distance between minor ticks in the bottom bar corresponds to 1 mm.

can be appreciated, the agreement is excellent. We next explored how the elongation affected the PC imprinted in the elastomer. A single iteration of the protocol followed is shown in Figure 4.10a and a photograph of the real sample are presented in Figure 4.10b. Diffraction images were collected in the cycle steps labelled as i, ii and iii. The process was continued by successively increasing the applied strain while monitoring the diffraction angles along the two symmetry directions ($\vec{b}_1$ and $\vec{b}_2$) of the reciprocal space (see Figure D.1 of Appendix D).

When the sample was stretched and cooled below T_{trans}, the temporary shape was fixed and thus the lattice parameter increased (decreased) along $\vec{b}_1$ ($\vec{b}_2$ by Poisson effect). These changes in the periodicity of the grating directly affected the diffraction angles and, therefore, the diffraction figure gradually deformed from a circumference to an ellipse as clearly exhibited in Figure 4.11. The behavior of the diffraction angles as a function of the applied strain is presented in Figure 4.12a and Figure 4.12b, along with the theoretical model (see Appendix D). Programed strain was increased up to 100 % (with higher precision for small strains) while monitoring the angles at $\lambda = 532$ nm or 633 nm. Good agreement was found between experimental data and theoretical predictions up to strains of 100 %, thus confirming that it was possible to fix the lattice parameter of the 2D PC in the predefined way. Nevertheless, the agreement was slightly worse above 60 % of strain possibly due to two contributing factors. On the one hand, the deformation

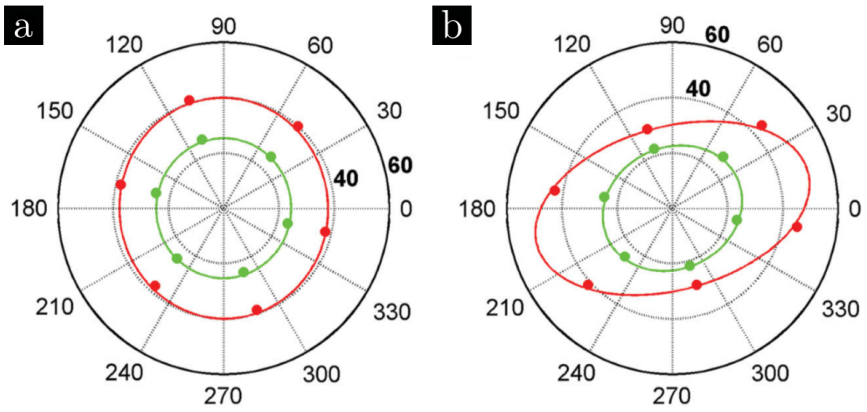

Figure 4.11: Representative polar plots exhibiting the experimental points coordinates of a diffraction figure from nanopatterned PDDC-HD in a) the initial state and b) after fixing a strain of 15% for two wavelengths: $\lambda = 532$ (green) and 633 nm (red).

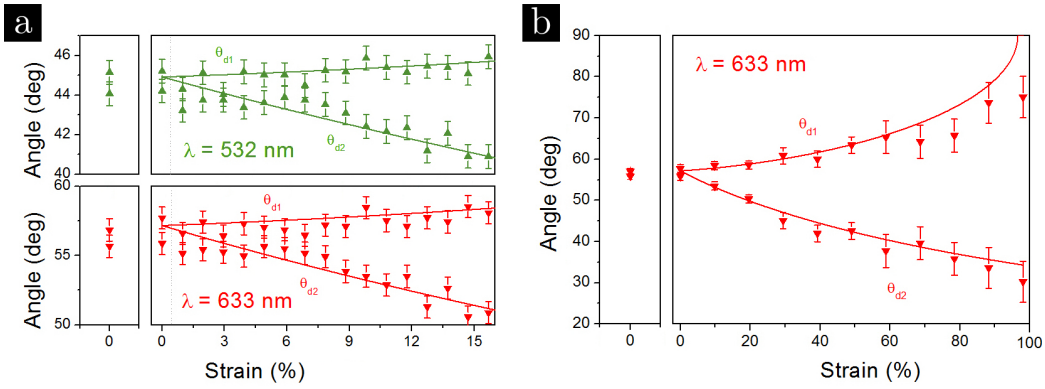

Figure 4.12: Experimental (triangles) and theoretical (solid lines) behaviors of the diffraction angles along the two principal symmetry directions ($\vec{b}_1$ and $\vec{b}_2$) as a function of the strain imposed to the sample: a) up to 15 % of strain for wavelengths $\lambda = 532$ nm (green) or 633 nm (red) and b) up to 100 % strain. Each subplot on the left corresponds to the angles measured after re-heating the polymer and recovering its initial shape.

got increasingly inhomogeneous along the sample, being more intense near the sustaining clamps. On the other hand, the diffraction spots projected on the screen gradually deformed into line segments implying a worse defined θ_d. In any case, as exhibited in the left subplots of Figure 4.12, the original diffraction angles were entirely restored after heating the sample at the end of the process, which demonstrates the SME affecting the 2D grating. It is worth noting that the data plotted correspond to a single piece of polymer and that each data point entails a heat-stretch-cool-relax cycle followed by a heat-relax cycle, setting a cyclability indication. In this particular study, up to 35 cycles were achieved with a representative sample. However, a modest cyclability is expected for this type of polymers as higher temperatures impact on polymer cross-linking and gradually eliminate the shape-memory properties of the material while increasing its stiffness (see Section 4.6).

4.9 Surface pattern self-healing

The second test to ascertain programmable features of the photonic nanostructure imprinted in the PDDC-HD polymer was to study if it could be erased and later recovered by using its SME. This hypothesis was supported by previous work on SME at the nanoscale [147]. The procedure was implemented as depicted in Figure 4.13. Accordingly, the sample was compressed between two hydrophobic surfaces of polypropylene. The thickness reduction of the elastomeric piece, after fixing the temporary shape and releasing the applied stress, was on the order of 50%. The morphology of the PDDC-HD elastomer in the three states labelled as i, ii and iii was characterized by AFM, SEM and optical diffraction measurements (Figure 4.14). As expected, the obtained pattern profile at the nanoscale was very similar for states i and iii, contrarily to that obtained for state ii (Figure 4.14a). The surface roughness in state ii decreased in comparison to i and iii (Table 4.2), in agreement with its much smoother aspect observed by SEM (Figure 4.14b). In ii, the pattern might still be intuited, although with a significant decrease of contrast. Finally, diffraction images were collected in order to study how the described behavior affected the optical properties of the PDDC-HD-based PC. As observed in Figure 4.14c, hexagonal patterns were obtained and reproduced along the entire sample area in states i and iii. On the contrary, for state ii, it was impossible to observe any diffraction image while scanning through the whole surface. We hypothesize that, although the nanopattern was not entirely erased by compression (Figure 4.14b), the periodic part of the modulation became comparable to, or smaller than, the random part so that basically, stray light was observed.

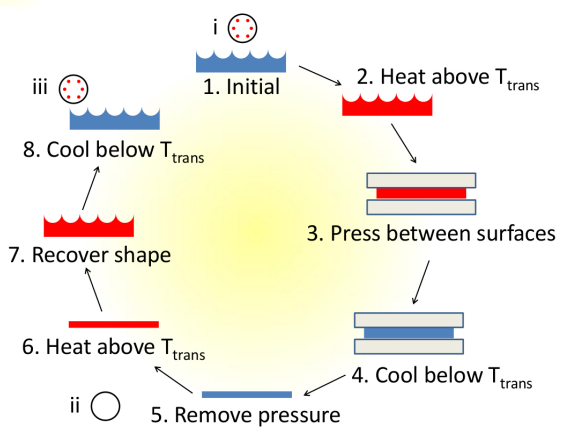

Figure 4.13: Scheme of the protocol followed for studying the hypothesis of erasing the surface nanotopography and testing self-healing features of the imprinted gratings.

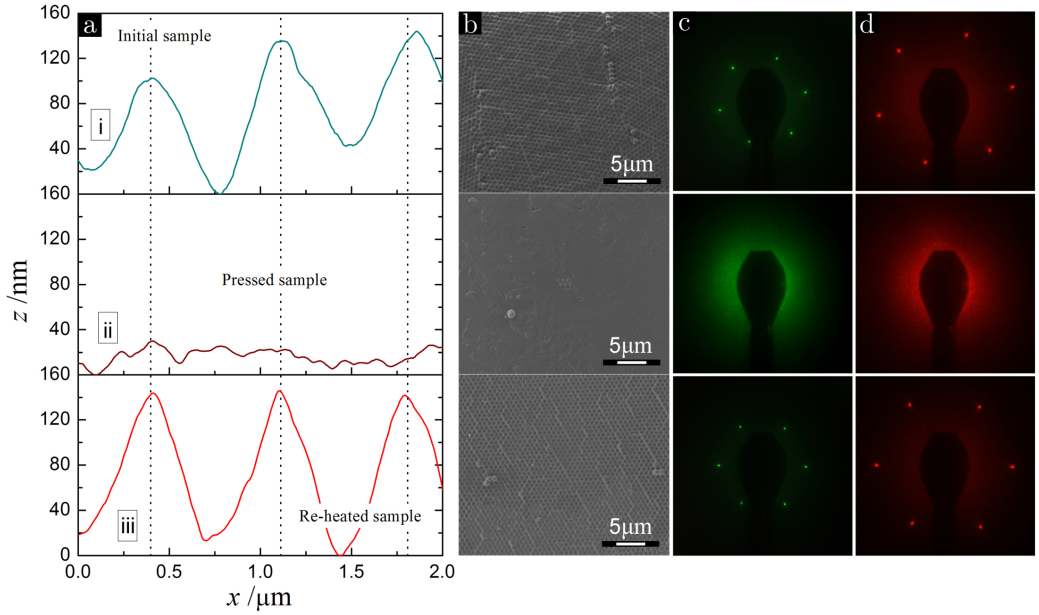

Figure 4.14: a) AFM Horizontal profiles of the initial sample (i), after compression and nanopattern erasing (ii) and after shape recovery (iii). b) Similar characterization using SEM. Diffraction images of the PDDC-HD sample in the referred states for two wavelengths: c) $\lambda = 532$ and d) $\lambda = 633$ nm.

State	R_a [nm]	R_{rms} [nm]	R_{max} [nm]
i	52.8	68.4	774.8
ii	7.1	9.6	71.1
iii	54.4	68.0	631.3

Table 4.2: Comparison among the average (R_a), root mean squared (R_{rms}) and maximum (R_{max}) surface roughnesses of the PDDC-HD sample in states i, ii and iii, as measured by AFM.

4.10 Conclusions

The multifunctional nature of PDDC-HD is confirmed by several interesting features. It is elastomeric, biocompatible, biodegradable and also presents SME capabilities. In the present work, we further expanded this spectrum of functionalities. It was shown that, by using a simple replica molding proceedure, it was possible to engrave a hexagonal nanostructured pattern, from a colloidal crystal template, in the surface of the PDDC-HD elastomer.

Two proofs of concept were reported herein, representing advances in both SMPs and photonics fields. Firstly, we showed that the lattice parameter of the 2D grating was programmable and dependent of the strain imposed to the polymer. Secondly, it was feasible to transitorily erase the surface nanopattern from the optical point of view. In both cases, the characteristics of the original structure were entirely recovered by simply heating the sample above T_{trans}, thus proving the SME affecting the optical properties of the PC and also its read/write capabilities.

The use of light-induced SME, independent from temperature, might be a valuable asset for future developments in this area. We also envision the present system to have a wide impact, not exclusively in the field of photonics, due to the feasibility of incorporating additional components such as bioactive molecules or nanoparticles into the polymeric network. This fact opens a wide range of opportunities for the combination of different functionalities in these nanostructured PDDC-HD elastomers, thus creating systems with application in biomaterials, nanoelectromechanical devices, self-healing optical elements, or devices with programmable hydrophobicity. Their application in diffusive composites will be discussed in the next chapter.

5

Multifunctional diffusive composites with shape-memory

The present chapter addresses the fabrication and characterization of novel composites based on polydiolcitrates doped with titania nanoparticles, aiming at expanding the capabilities of the original elastomers towards the control of light diffusion. These materials constitute advanced photonic white paints which incorporate the shape memory effect as an additional functionality. It is shown that it is possible to taylor the light transport mean free path by acting on the titania fillers concentration. Moreover, optical gain is introduced by doping the composites with organic dyes and it is demonstrated that they may present non-resonant feedback random lasing.

5.1 Introduction

As explained in the previous chapter, SMPs may be useful for producing 2D gratings with increased funtionality, in particular, programmable features. Naturally, for that type of structures, a periodic refractive index is required. On the other hand, random media are also being actively investigated in photonics [64].

In the context of diffusive materials, the application of SMPs as matrices for RLs can be highly convenient. The added functionality provided by the SME would enable the development of thermoresponsive optical gain media with arbitrary and configurable shapes. In the present work, a convenient route to achieve such a system is proposed, by presenting a novel kind of SMP composites, materials which are advancing rapidly nowadays [164, 165]. Traditionally, the motivation to incorporate specific fillers into SMPs has relied on four main reasons: 1) mechanical reinforcement [166], 2) search

for increased functionalities - for example, electrical conductivity [167], 3) exploration of alternative mechanisms responsible for triggering the SME [168] and 4) development of new effects such as multi-shape memory or two-way shape memory [59]. Although composite materials are also tremendously advantageous for implementation in optical systems [169], the incorporation of optically functional fillers in SMPs, addressing the enhancement of the diffusive transport of light, has remained rarely investigated. In most of the cases, the purpose of using these fillers has been to improve light absorption, aiming at their use as internal heat sources and promoting, for instance, a remotely actuated, light-triggered SME [167].

Regarding non-absorbing fillers, there are reports of dielectrics being integrated into SMPs (e.g., silica particles [170] or microfibrillated cellulose [166]) for purposes other than manipulating the light transport. For example, it has been demonstrated that it is feasible to incorporate rutile into PS without drastically affecting its mechanical properties [171]. Moreover, the addition of small titania particles (with sizes typically below 25 nm) in ordinary polymers is frequent [172]. The resulting materials display a higher refractive index while retaining the polymer features of interest like transparency. To date, there are works describing titania embedded in poly(methyl methacrylate) [173] and epoxy [174], as well as polyimidothioethers-TiO_2 hybrids [175], to cite a few.

Here, the fabrication of novel composites made of titania nanoparticles embedded into a SMP polydiolcitrate [155], specifically PDDC-HD, is described. First the preservation of the SME in the resulting elastomer was explored, after the titania addition. Polydisperse particles were used as fillers, in concentrations sufficient to assure that light-matter interaction was within the multiple scattering regime. The transport mean free path of light was characterized from measurements of coherent backscattering. The proposed system was also a suitable host for incorporating organic emitting dyes and its use as a configurable-shape active medium was investigated. To assess its utility for developing RLs, amplified spontaneous emission (ASE) was studied in these dye-doped composites.

5.2 Samples fabrication

Polydisperse titania (rutile) particles coated with a thin alumina layer were purchased from Sachtleben. Their size was characterized by using length measurements from SEM images as the one presented in Figure 5.1a. Furthermore, Figure 5.1b shows the resulting histogram of sizes, obtained from

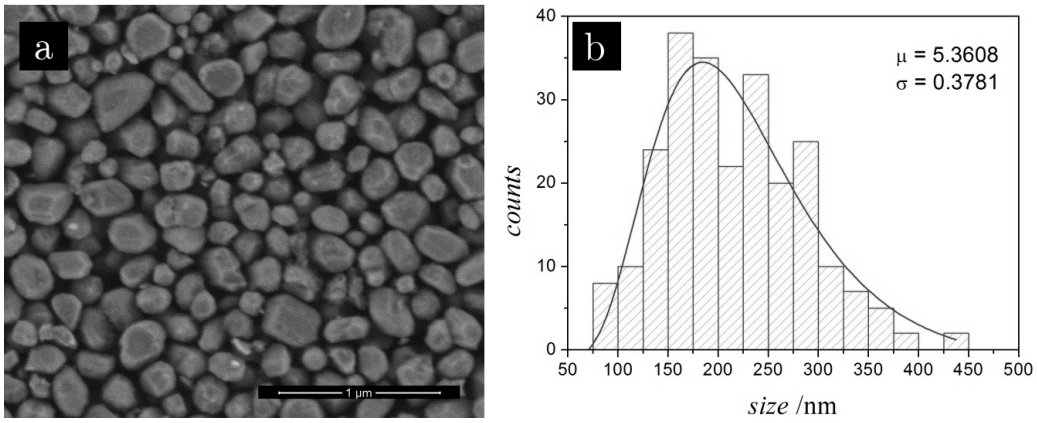

Figure 5.1: a) Representative SEM image used for estimating the size of the titania particles used in this work. b) Resulting particle size histogram.

240 measurements along random directions. The data were fitted using a lognormal distribution of the form

$$\Phi(x|\mu,\sigma) = \frac{1}{x\sigma\sqrt{2\pi}} \exp\left[\frac{-(\ln x - \mu)^2}{2\sigma^2}\right], \tag{5.1}$$

with parameters $\mu = 5.3$ and $\sigma = 0.4$, which translate into a mean (defined as $\exp(\mu + \sigma^2/2)$) of approximately 230 nm (most frequent value of 185 nm). Additionally, citric acid, 1,12-dodecanediol, Rhodamine B (RhB) and fluorescein were purchased from Sigma-Aldrich and used as received. Stilbene 3 was purchased from Lambda Physik GmbH. Ethanol 99.5% was purchased from Panreac. For the synthesis of the shape memory prepolymer, a process similar to the one exposed in the previous chapter (section 4.3) was followed [48].

A method of in situ processing blending was used for preparing the titania-doped PDDC-HD composites. Briefly, the prepolymer was heated up in a thermal bath at 90°C during the time needed for it to become perfectly transparent and transit to the viscous liquid state. Titania particles (powder) were weighted into a polypropylene vessel that was used as a mold for producing tablets and set the permanent shape of the composites. The corresponding mass of prepolymer was poured into the vessels and the mixture was energetically stirred. Samples were then cured in an oven at 90°C during 12 h. After that period, they were unmolded and cut in the desired shape. A similar procedure was followed for the preparation of doped composites containing both titania and the organic dye (RhB, stilbene 3 or fluorescein). In this case, after adding the PDDC-HD prepolymer to the titania particles

and before mixing all the components, a solution composed of the organic dye dissolved in ethanol (15 mg mL^{-1}) was also added, at the desired concentration. Due to the presence of ethanol, the curing process was delayed and extended to 19 h for these samples.

5.3 Microstructural characterization

As mentioned in the previous section, polydisperse rutile particles were selected for these experiments. This choice was due to their high refractive index ($n = 2.61$) and therefore high scattering efficiency, important properties from the optical point of view. In Figure 5.2a, a high-magnification transmission electron microscopy (TEM) image showing the aspect of these particles is presented. It is notorious that they display irregular shapes and their size is of the order of visible radiation wavelengths.

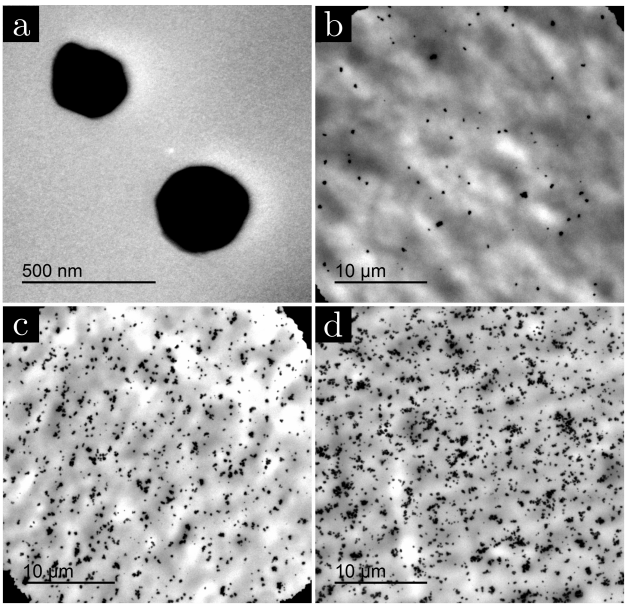

Figure 5.2: a) High-magnification TEM image showing representative titania particles used as scatters embedded in the elastomers. TEM images of thin laminar cuts of PDDC-HD samples doped with 1, 10, and 20 wt% of titania particles (b, c, and d, respectively).

After curing and unmolding, solid tablets were obtained, with 2 cm in diameter and variable thickness (controlable by setting the initial quantities of prepolymer and titania). In these experiments, the mass of titania with respect to the total mass - expressed as the ratio f - ranged from 0 to 20 wt%.

A summary of the samples fabricated is shown in Table 5.1. The mass density of the resulting composites was determined experimentally by weighting sample pieces and dividing these values by their corresponding volumes as measured from the vertical displacement of water in a graduated cylinder. The results are shown in Table 5.1 (ρ) and also in Figure 5.3. Each data point corresponds to the average of at least six samples. As may be observed, ρ revealed a monotonous increase with the increase of f. Moreover, a theoretical estimation was also determined based on the mass densities of the pure elastomer PDDC-HD ($\rho_p = 1.10$ g cm^{-3}) and titania ($\rho_t = 4.00$ g cm^{-3}) and as a function of f, according to Equation

$$\rho(f) = \frac{\rho_p \rho_t}{\rho_p f + \rho_t [1 - f]}. \tag{5.2}$$

This mathematical function is plotted in Figure 5.3 along with the experimental data. Although Equation 5.2 is approximate, it describes quite accurately the expected behavior of the composites mass densities in the range of concentrations studied.

f %	ρ [gcm^{-3}]	c [cm^{-3}]	N_{TEM} [cm^{-3}]
0	1.10	0.0	*
1	1.11	5.7×10^{11}	5.1×10^{11}
2	1.15	1.2×10^{12}	*
5	1.17	2.9×10^{12}	*
10	1.25	6.3×10^{12}	6.1×10^{12}
20	1.30	1.3×10^{13}	1.1×10^{13}

*No TEM data acquisition

Table 5.1: Summary of the samples fabricated, presenting the percentage of titania mass with respect to the total mass (f), the respective mass density of the composite after curing (ρ) and the concentration of titania expressed as the number of particles per unit volume (c). Selected concentrations were compared with the concentrations estimated from TEM images (N_{TEM}).

Using the mass densities of the composites, weight percentages were converted to estimated particle concentration (c). The obtained values (Table 5.1) are in range with the typical concentrations of scatters used for studying diffusive systems [176]. An important point must be noticed. It is well known that achieving filler uniformity in polymeric matrices during the fabrication of composites is a critical issue. A very common problem hindering good quality materials has to do with filler aggregation, due to van der Waals or

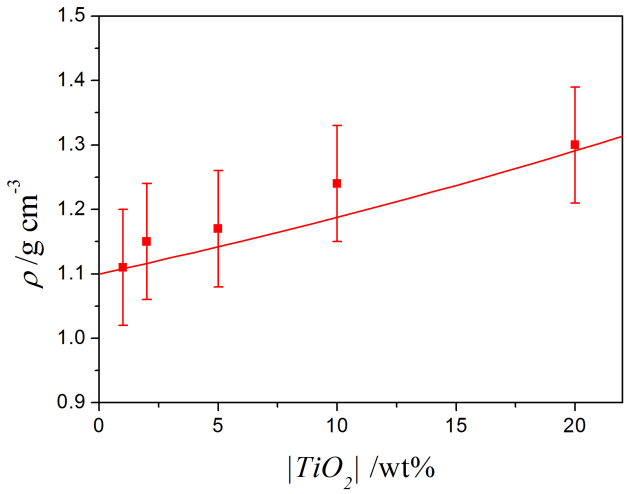

Figure 5.3: Plot exhibiting the measured mass density of the composite as a function of the weight percentage of titania embedded. The solid line corresponds to the expected variation of this parameter as determined by Equation 5.2.

electrostatic forces [171]. Surface treatment is a possible solution to change interparticle potential and to reduce those interactions. In that way, to avoid aggregation and improve titania dispersion into the viscous prepolymer, particles coated with a thin (nm) layer of alumina were selected for all the experiments described in this work (for convenience, referred to merely as titania particles throughout the text). Selected samples were characterized using TEM in order to ascertain the state of the fillers dispersion in the elastomer. Some representative images are shown from Figure 5.2b through Figure 5.2d, for the concentrations of 1, 10, and 20 wt%, respectively. Because titania is opaque to the electron beam, it was clearly distinguishable from the background, which corresponded to the elastomer matrix. Moreover, TEM images analysis confirmed the expected differences in particle density and no significant aggregation, even for the samples containing the highest amount of fillers. The concentration of titania particles was determined from these images (Table 5.1, column N_{TEM}) and, as can be verified, it was in excellent agreement with those estimated from the parameters f and ρ.

5.4 Shape memory effect

In order to confirm that the shape memory features were preserved in titania-doped composites and to determine T_{trans}, modulated DSC measurements similar to those in the previous chapter were performed. Figure 5.4a com-

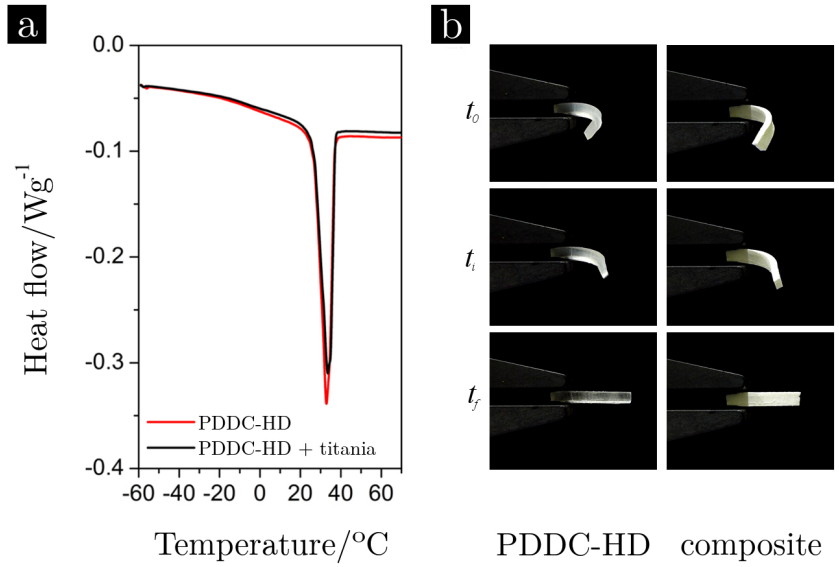

Figure 5.4: Comparison of a sample of PDDC-HD containing 10 wt% of titania with non-doped PDDC-HD regarding a) total heat flow measured by mDSC and b) thermomechanical programming, being t_0 the temporary shape, t_i an intermediate state, and t_f the permanent recovered shape.

pares the total heat flow from a sample of PDDC-HD elastomer with that of a composite doped with 10 wt% of titania. In both cases, the results demonstrated the existence of a melting transition at *ca.* 32°C, in agreement with previous reports [48], which confirmed that titania particles did not interfere thermally with the SME in these composites. As already described, this transition is the mechanism originating the physical switching responsible for the SME in this kind of SMPs. Preservation of the SME was further verified by analyzing thermomechanical programming (Figure 5.4b). Small rods with approximately $(20 \times 2 \times 1)$ mm^3 were cut from the initial tablets, heated up, deformed, and then cooled down to set the temporary state t_0. As the rods were slowly warmed up using a hot air flux, the temperature surpassed the melting transition and the permanent shape was restored. This evolution is exhibited in the figure, illustrating images of t_0 (left column), an intermediate state t_i during recovery (middle) and the restoration of the permanent shape t_f (right) for both PDDC-HD and 10 wt% titania-doped PDDC-HD rods.

5.5 Optical properties

As may be appreciated in Figure 5.5, both the aspect and the behavior as a function of temperature of a cured tablet composed of PDDC-HD only (Figure 5.5a) was quite distinct from the one of a PDDC-HD disk doped with titania (Figure 5.5b, 2 wt% of titania). Both samples presented negligible absorption in the visible range, therefore their aspect was white and opaque at room temperature. In the case of nondoped elastomers, this phenomenon was due to light scattering from hydrophobic microdomains of prepolymer and remaining non-cross-linked 1,12-dodecanediol [48]. In doped ones, additional scattering resulted from the presence of titania particles. This effect could be clearly noticed, by the naked eye, by a significant decrease in translucence. The optical behavior of the materials was significantly different when heated above T_{trans}. Specifically, while the nondoped sample became transparent (increase of ca. 70% in transmittance - see section 4.7) due to solid microdomains melting, the titania-doped composites retained an opaque and white appearance (transmitted signal below detector limit), independently of titania concentration, as measured by total transmittance spectroscopy.

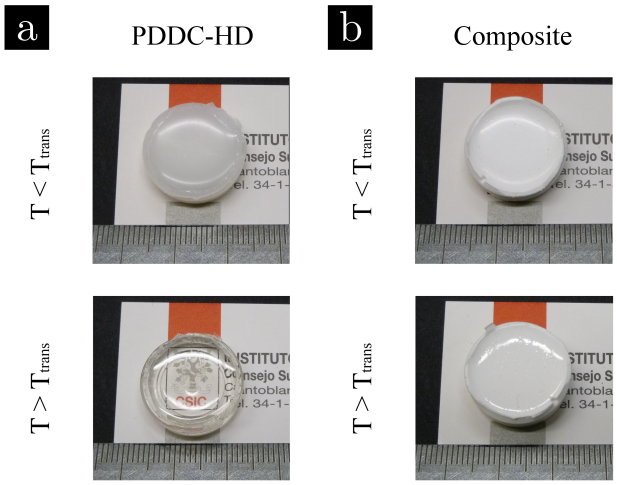

Figure 5.5: Typical images of a tablet made of a) PDDC-HD only and b) PDDC-HD doped with 2 wt% of titania, at two different temperatures: below (top) and above (bottom) T_{trans}.

Light transport in these composites was characterized for the wavelength $\lambda = 633$ nm (He–Ne laser) by measuring the intensity of backscattered light from thick samples (*ca.* 5 mm) and analyzing the coherent back scattering cones (CBCs). For diffusive materials, it is known that light following different optical paths in the medium interferes constructively and builds an

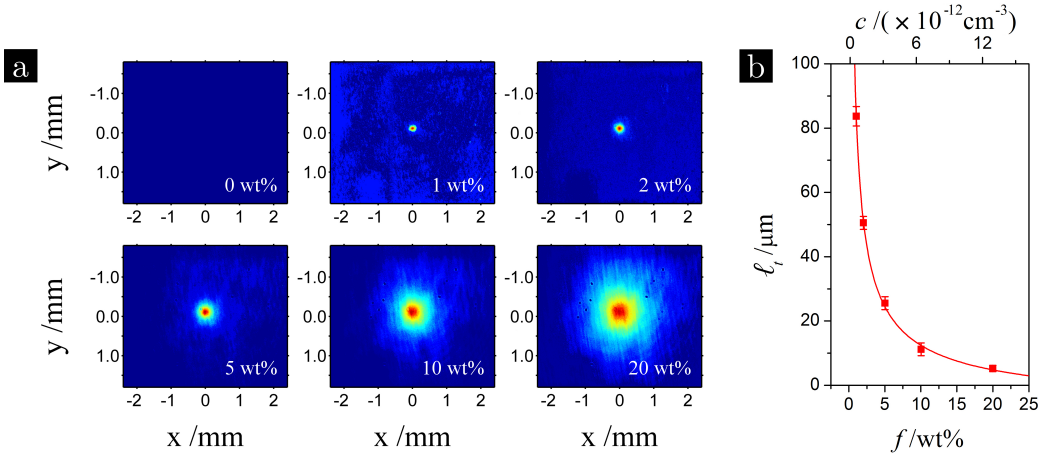

Figure 5.6: a) Consecutive intensity plots exhibiting the widening of the CBC (λ = 633 nm) emanating from PDDC-HD elastomers doped with titania, as a function of particle concentration. The intensities were normalized so that the color code corresponds to the interval [0,1]. b) Behavior of ℓ_t at λ = 633 nm, depending on titania content (bottom axis) or particle concentration (top axis).

enhanced reflectance for small angles around the incidence direction. This observation is referred as the CBC [177,178], which is a signature of weak localization of light. The width of the observed cone is related to the transport mean free path (ℓ_t) of the radiation in the medium (see Appendix C).

The CBCs measured at room temperature, obtained for the samples containing the different titania concentrations are presented in Figure 5.6a. For the case of non-doped samples (top left), a homogeneous background was obtained, not exhibiting any appreciable sign of the coherent component. This fact accounts for a very large ℓ_t that implied a very narrow CBC, beyond the resolution limit of the optical setup used. As appreciated in the subsequent plots of the figure, the CBC built up and its width increased as the concentration of titania in the composite augmented. This observation is consistent with a decrease of ℓ_t. In Figure 5.6b, the results of ℓ_t obtained from the profile fittings, using Equation C.1, are plotted as a function of f and c. The trend obtained agrees with previous results reported on colloidal suspensions [177]. The solid line corresponds to a fit using an equation of the form $(1/\ell_t - 1/\ell_0) = k \cdot c$ [38], which describes very reasonably the trend expressed by the data. The parameter ℓ_0 is the transport mean free path of light in the limit where no titania scatters are present (PDDC-HD only) and resulted in a value of approximately 210 μm.

5.6 Incorporation of organic dyes

A new set of samples was prepared incorporating also RhB as a dopant to further ascertain the multifunctional features of these composites - see section 5.2 for experimental details. The possibility of including fluorescent dyes in SMPs has drawn attention recently [179–181]. Although previous work reported the loading of dichlorofluorescein in shape memory polydiolcitrates [48], the purpose of those studies was to explore drug delivery capabilities of PDDC-HD. On the contrary, the present objective was to introduce optical gain in the composites so that light amplification could be achieved and studied. The dye might be incorporated during the prepolymer synthesis, during the preparation of the composites, or even later in the already cross-linked composite by swelling in ethanol. While the first method could cause undesired chemical alterations on the dopant, due to the use of higher temperatures (*ca.* 140°C), the third one results in a lower and more heterogeneous dye loading dependent on ethanol infiltration in the polymer. After an initial exploration, the second procedure (i.e., loading during polymer cross-linking at a milder temperature) was selected as the most convenient since it allowed for both the homogeneous mixing of the different components and a more accurate control of the concentration of each one (prepolymer, titania, and RhB).

Contrarily to PDDC-HD and titania-doped composites, PDDC-HD doped with RhB presented an intense red color, which was due to the absorption of the organic dye (Figure 5.7a). In these samples, the quantity of RhB incorporated was 0.2 wt% of the total composite mass (concentration of the order of those used in previous work [38]). Apart from color, dye-doped PDDC-HD presented a temperature dependence equivalent to the one shown in Figure 5.5a, meaning that its transparency increased significantly above T_{trans}. This phenomenon extends its technological interest by potentiating systems with switching capability from transparent gain media (to be applied in conventional lasers) to scattering media for application in RLs. Suggestions in this direction, proposing devices with controlled diffusivity, have been recently reported in the literature [182] and are expected to lead to new tools in a near future. In our case, diffusivity switching was also associated with shape changes, a fact that may benefit the development of programmable sensing/actuating devices in which thermal, optical, and mechanical properties are coupled. Regarding the elastomers doped with both titania and RhB, as the quantity of particles increased, a color gradient was appreciated, from intense red to slightly stained magenta (Figure 5.7a). Tuning the concentration of particles is thus an effective protocol for changing the color saturation of these materials.

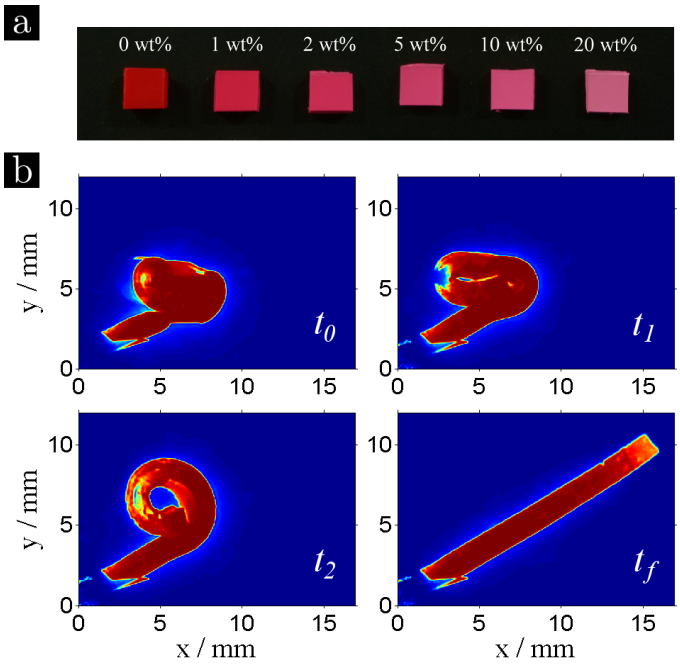

Figure 5.7: a) Image of a set of composites of PDDC-HD doped with 0.2 wt% RhB and increasing quantity of titania particles. b) Photoluminescence images of a titania (10 wt%) and RhB (0.2 wt%) doped rod programmed in a temporary state t_0 and at different steps of the shape recovering process - t_1 (24 s), t_2 (29 s), and the final permanent shape t_f (36 s). The intensity was normalized so that the color code corresponds to the range [0,1].

As demonstrated by mDSC and thermomechanical characterization, the SME was also preserved in the dye-doped media. Thermal analysis revealed that the melting transition at *ca.* 32°C was also present in PDDC-HD doped only with RhB and doped with both titania and RhB (Figure 5.8a). Furthermore, in thermomechanical programming experiments, these samples exhibited a behavior similar to that exemplified in Figure 5.4b. As may be observed in Figure 5.8b, the RhB doped rods also recovered their permanent shape after heating. The fact that the organic dye could be incorporated within the composites, while preserving the SME has interesting implications. Functionalities of PDDC-HD, which are typically explored only from the SMP point of view, were enhanced by producing elastomers that add up both scattering and photoluminescence (PL). Figure 5.7b exhibit the PL spatial distribution of a rod composed of PDDC-HD doped with 0.2 wt% of RhB and 10 wt% of titania particles, during a representative thermomechanical programming cycle. A rod cut from the initial tablet was programmed in a temporary shape

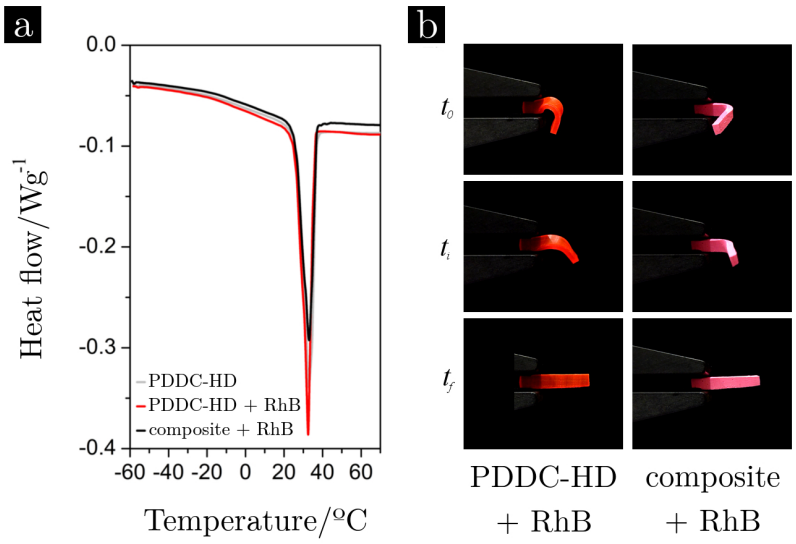

Figure 5.8: Comparison of a sample of PDDC-HD containing 10 wt% of titania and 0.2 wt% of RhB with the dye-doped PDDC-HD regarding a) total heat flow measured by mDSC - for reference the curve of the non-doped elastomer was also included - and b) thermomechanical programming, being t_0 the temporary shape, t_i an intermediate state, and t_f the permanent recovered shape.

by heating, rolling, and cooling it down while maintaining the applied stress. It was then excited with an expanded 532 nm laser pulsed at 10 Hz and slowly heated with a hot air flux. Simultaneously, the PL in the red range of the spectrum was recorded. In the figure, t_1 corresponds to the state of the sample 24 s after starting the application of the hot air flux and t_2 after 29 s. As observed, the rod unrolled, which was reflected on the PL spatial distribution. After 36 s, the permanent shape was completely restored (t_f). While Figure 5.7b demonstrates the possibility of monitoring the shape recovering process using PL in a single thermomechanical cycle, the reciprocal is also true. Different cycles of programming could lead to a different shape set each time, thus evidencing that these composites performed as configurable shape, optically active media.

It is also worth noticing that the results obtained in the red region of the visible electromagnetic spectrum due to RhB emission ($\lambda \sim 610$ nm, see Figure 5.10a) could be transferred to other spectral regions, in particular to the blue and green ones. This was achieved, as explained in section 5.2, by incorporating other organic dyes with luminescence in those ranges: stilbene 3 and fluorescein, respectively. In the case of stilbene 3, the doped-composite showed a white aspect derived from the fact that the absorption was in the

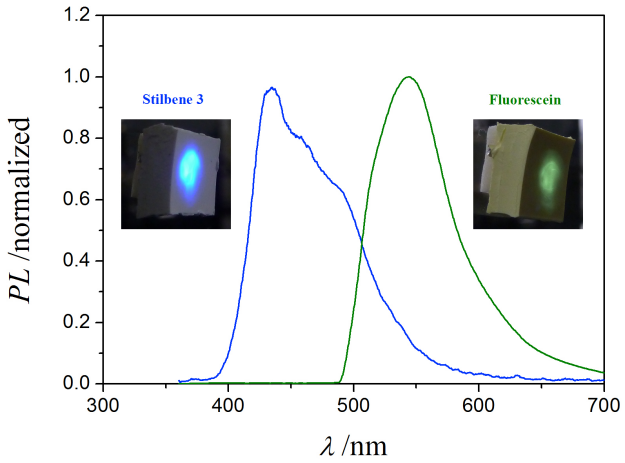

Figure 5.9: Images of blocks of PDDC-HD elastomer doped with 10 wt% of titania particles and either stilbene 3 (left) or fluorescein (right) (0.2 wt%). Blue and green curves correspond to the PL spectra emitted from the respective samples.

UV range. The maximum PL was at *ca.* 430 nm. On its turn, the composite doped with fluorescein presented yellow color and maximum PL at *ca.* 540 nm (Figure 5.9). The fact that the three regions of the electromagnetic spectrum could be accessed by using this procedure potentiates the versatility of these materials and opens their interest for the development of novel thermoresponsive displays and white light generation.

5.7 Amplified spontaneous emission

In order to assess the performance of the proposed composites as a gain material, ASE was systematically characterized. Samples were optically pumped at $\lambda = 532$ nm. Two sets of experiments were performed: first, varying the amount of titania while keeping the concentration of RhB constant at 0.2 wt% and second, using an intermediate titania concentration (5 wt%) and varying the concentration of RhB. It was not possible to identify ASE from the elastomer doped only with RhB (Figure 5.10). In this case, the PL intensity increased linearly with pumping energy (there was no evidence of ASE threshold) and no spectral narrowing could be observed up to pumping energies of the order of 1.5 mJ per pulse. Further increase of the pumping energy led to sample damage. On the contrary, for the composites incorporating titania scatters, ASE was observed, even for those with the smallest amount of particles. The complete set of measurements showing the spectral narrowing

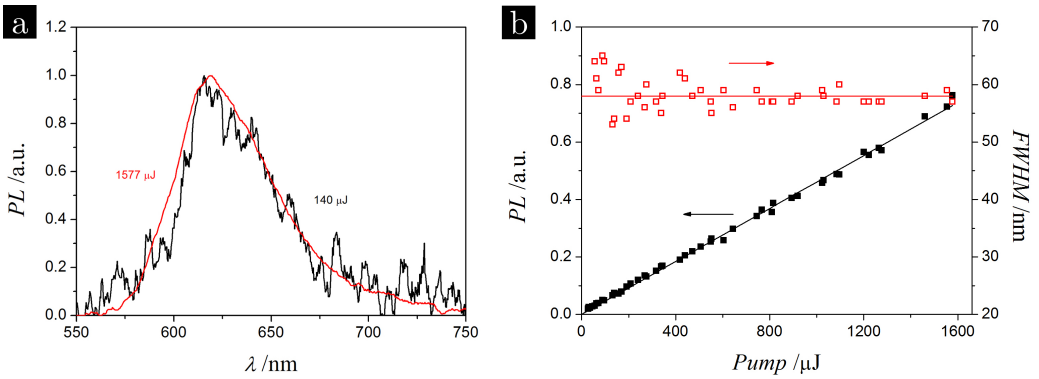

Figure 5.10: a) PL spectra of a sample of PDDC-HD doped with 0.2 wt% of RhB at low (black) and high (red) pumping energies. b) PL intensity (solid black squares, left axis) and spectral width (open red squares, right axis) as a function of the pumping energy for the same sample.

of PL is presented in Figure 5.11. A typical peak narrowing of the order of 60% was achieved in these measurements, which is slightly higher than that generally reported for other kinds of non-resonant feedback RLs. This observation suggests a significant contribution of spontaneous emission and also other possible fluctuations derived from the material complexity. A red shift of the stimulated emission with respect to the maximum gain was observed as the concentration of fillers increased. This phenomenon might be due to ground state absorption, as reported previously [183]. Importantly, in these spectra, discrete lasing modes frequently observed in RLs were not revealed, likely because no coherent feedback [35] was present in our samples. ASE behavior was evidenced more clearly in the curves of PL intensity and full width at half maximum as a function of the pumping energy (Figure 5.12), from which the thresholds were extracted by fitting a linear dependence to the high fluence range. For all titania concentrations, the fittings intersected the horizontal axis in a value different from zero, confirming that an ASE threshold was present. The results revealed that the threshold energy (E_{th}) decreased as the amount of titania present in the composite increased or, equivalently, E_{th} increased with the increase of ℓ_t (Figure 5.13a). This was expected due to the increase of the stimulated emission optical path, derived from the increased scattering.

In parallel, a set of samples varying the quantity of doping organic dye was prepared, maintaining the concentration of scatters constant (ℓ_t constant). In this case, changes of the mass density of the composite were negligible since the quantity of RhB was at least one order of magnitude smaller than the one of titania. The concentration of the emitter was varied in the range [0.002,

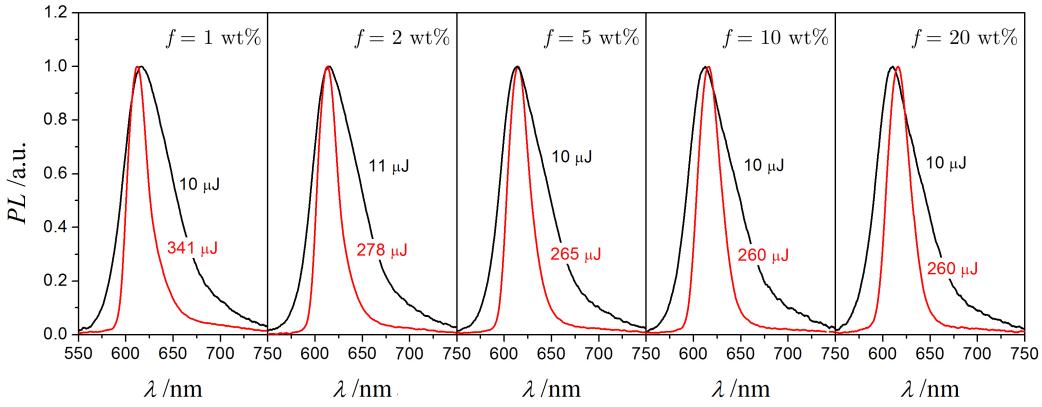

Figure 5.11: Complete set of PL spectra from samples of PDDC-HD doped with 0.2 wt% of RhB at low (black) and high (red) pumping energies for increasing doping quantities of titania scatters.

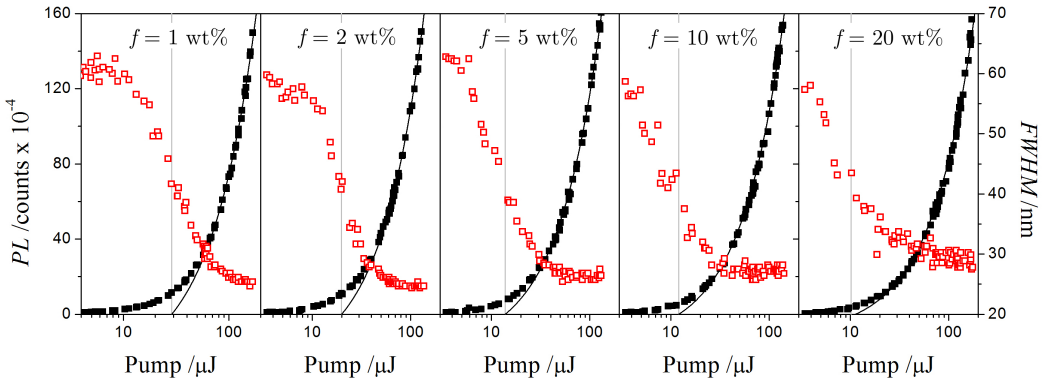

Figure 5.12: PL intensity (solid black squares, left axis) and spectral width (open red squares, right axis) as a function of pumping energy for samples of PDDC-HD doped with 0.2 wt% of RhB and increasing doping quantities of titania scatters. The grey line marks the point in which the linear fitting of the high energy data intersects the horizontal axis.

0.1] wt%. Similarly to previous experiments varying titania concentration, spectral narrowing of the PL emission, characteristic of ASE, was also noticed. A slight red shift with respect to the gain maximum could be observed only for the two samples containing the smallest amount of RhB. As shown in Figure 5.13b, the threshold decreased with the increase of dopant RhB in the composites. This trend agrees with previous work [184] and is derived from the fact that, as the concentration of emitter increases, the gain length is expected to decrease, thus absorption increases and is easier to attain ASE.

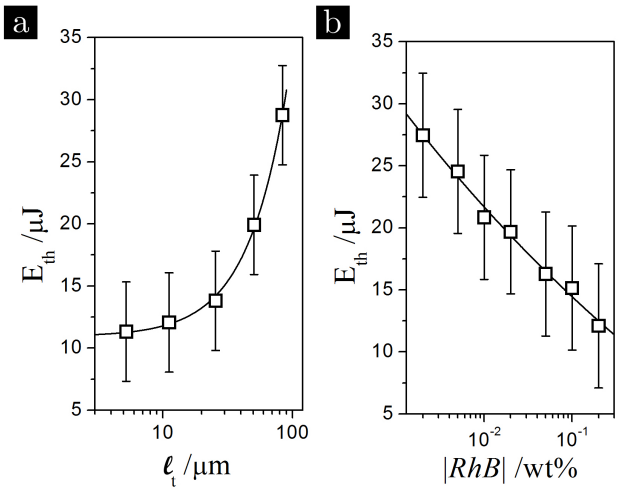

Figure 5.13: a) Dependence of the energy threshold of a set of samples on ℓ_t, for a fixed RhB amount (0.2 wt%). b) Dependence of the energy threshold of a set of samples on RhB concentration, for a fixed titania quantity of 5 wt%.

5.8 Conclusions

In summary, it was possible to efficiently embed titania particles, homogeneously dispersed, in the PDDC-HD elastomer matrix and take advantage of their strong scattering efficiency for developing new diffusive media. The composites produced in this way still preserved the SME exhibited by the non-doped elastomer and its characteristic melting T_{trans}, regardless on doping (with titania particles, RhB, or both). A clear influence of filler concentration on light transport properties of the media was demonstrated, being an essential parameter to consider when designing and applying these systems so their full multifunctional potential can be exploited. PL from dye-doped samples was characterized in detail, enabling pioneering observation of ASE in this type of composites. In this way, their usefulness for achieving non-resonant feedback RLs was confirmed.

We hope that this work paves the way for new advances in topics such as SME triggering, especially on light induced SMPs [52], new intelligent and responsive illumination systems, and fluorescence detectable actuators. The composites described here are highly versatile and may allow the stacking of different functionalities, for instance by incorporating more than one kind of fillers. In this sense, new programmable optoelectronic or optomagnetic devices [185] may come to light. Finally, interesting additional features of these composites, such as their low fabrication cost and easy scalable technology, might be very attractive from the industrial point of view.

Part III

Appendices

A

Fourier image spectroscopy

In order to further characterize the samples and ascertain their interaction with light, Fourier image spectroscopy was employed, in reflectance mode. This is a very powerful technique that enables the angle-resolved collection of the spectra and thus the direct probing of the dispersion relation of photonic crystals. Below we present a very brief overview of this technique. For further details and technical aspects about the home-built optical setup used for the measurements, see reference [186].

The setup used for FIS was adapted from the one proposed by Cottrell *et al.* [187] and its working principle was based on imaging the back focal plane of a high numerical aperture microscope objective (48.5°). Its fundamental element is schematized in Figure A.1 and is composed essentially of two lenses

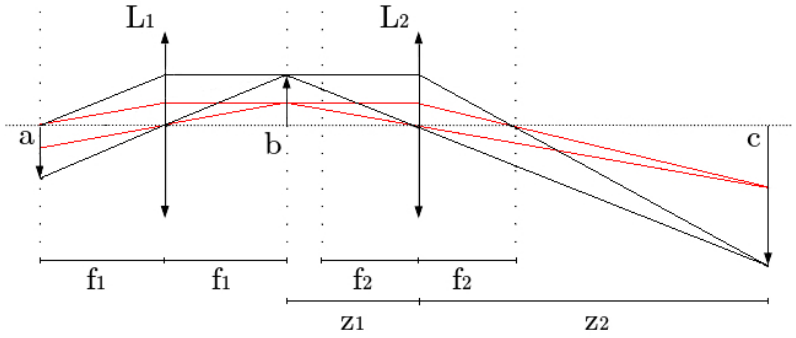

Figure A.1: Scheme illustrating the ray tracing in the fundamental unit of the optical setup used for characterizing Fourier image spectroscopy.

with focal distances f_1 and f_2, respectively. The figure shows the ray tracing for light leaving the sample at two different angles (black and red curves). As may be observed, parallel rays, at the front focal plane of lens L_1 (a),

are focused in the same point of its back focal plane - at position b. This configuration is usually denoted 2-f. Due to the small dimension of the image produced by the microscope objective at b, an additional lens L_2 is used, for creating a magnified image at the plane positioned in c. Therefore, this optical configuration maps angles leaving the sample at the front focal plane of L_1 to spatial coordinates at the plane c. For example, a point like isotropic light source would originate a uniformly illuminated circle at c. Illuminating the sample with white light and scanning an optical fiber, which is coupled to a spectrometer, perpendicularly to the optical axis at the position c, enables to collect the reflectance spectrum as a function of the angle.

B

Experimental setup for REs PL measurements

The optical setup employed in the PL characterization is schematized in Figure B.1. A continuous wave diode laser CNI-MDL-N, emitting at the wavelength $\lambda = 980$ nm, was used as light source (green beam in the figure). The setup was thus optimized for pumping ytterbium, which resonantly transferred energy to erbium, as explained in Section 3.1. The beam was focused and re-expanded by two lenses and a chopper blade, placed at the focal distance between them, cut it at a selected frequency. The incident laser power was further adjusted with neutral density filters (F), if required. The laser was focused on the sample and the PL (illustrated in red color in Figure B.1) was collected in reflection mode, by the same lens. A beam splitter (Bs) was used to separate the PL to another branch of the setup that was focused on the entrance of an optical fiber. Two additional long pass filters (LP) were employed in order to remove the pumping component and prevent it to reach the detector. The PL light was transmitted in optical fiber and coupled to the entrance slit of a Bentham TM300 monochromator. The output of the monochromator was again coupled through optical fiber to the entrance of a Hamamatsu H10330A-75 thermoelectric cooled photomultiplier tube module. The electric signal generated by the module was analyzed using a SR510 Stanford Research Systems lock-in amplifier (in the case of spectroscopy measurements) or to a Tektronix DPO3032 oscilloscope (in the case of PL life time measurements). By using a flip flop (Ff) mounted mirror, there was an additional possibility of introducing a white light line in the setup, in order to image the surface of the sample and better control the measurement point and focus. The images were captured using a Thorlabs DCU223M CCD camera.

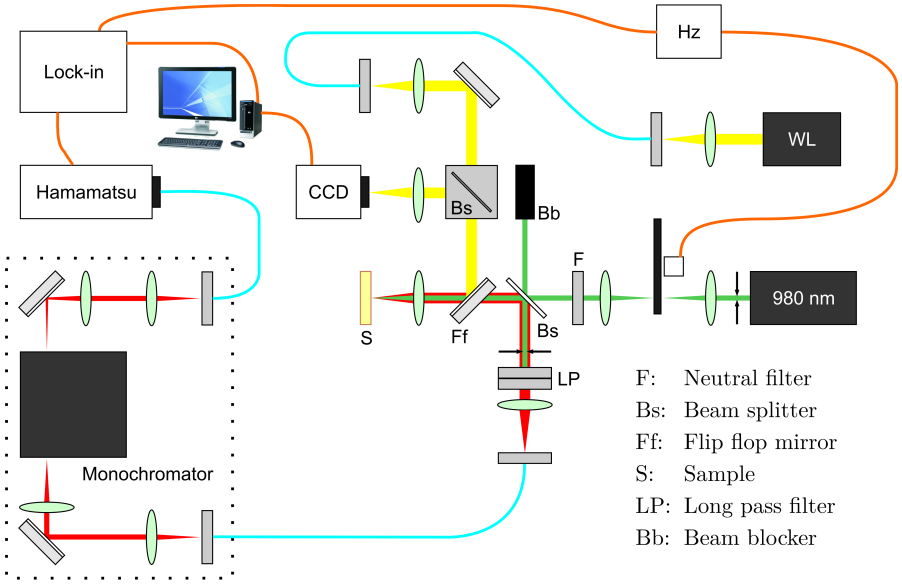

Figure B.1: Schematic illustration of the optical setup built for characterizing erbium PL, in the infrared region of the spectrum. Optical fibers are drawn in blue while orange connectors represent electrical connections.

C

Coherent backscattering of light

In this appendix we give a very short introduction to the phenomenon of coherent backscattering of light, also known as weak localization, so that the measurements of the light transport mean free path, may be better understood. For a more comprehensive treatment of the matter see, for example, references [188–190].

The coherent backscattering is a phenomenon that may be appreciated for different kinds of waves (acustic, quantum wave packets, electromagnetic radiation) interacting with strongly scattering media. In comparison with other systems, light study presents some advantages due to the weak photon-photon interaction, long coherence time that leads to high sensitivity to coherence effects and also the possibility of analyzing the angular distribution of the reflected and transmitted waves.

When a strongly scattering medium is illuminated with coherent light from a laser source, the light intensity at the incidence semi-space is essentially composed of a non-coherent and a coherent component. The non-coherent term is weakly dependent on the angle and is usually approximated to a flat background. The coherent term results from interference between reciprocal paths within the random medium. For different configurations of the sample, this component averages to zero, except for a narrow angular range around the incidence direction. Therefore, an enhancement of light intensity for the backscattering direction may be detected.

It can be shown theoretically that the enhancement should be of a factor 2, at exact backscattering direction and rapidly decay for higher angles. This shape of the intensity profile is called the coherent backscattering cone. Furthermore, its width is related to the transport mean free path (ℓ_t) of the radiation inside the medium and, by fitting the experimental cone profile to

the theoretical function

$$\gamma_c(\theta) = \frac{3}{2\ell_t^3 \alpha u} \frac{\alpha + u(1 - \exp(-2\alpha\xi))}{(u+\alpha)^2 + \eta^2}, \tag{C.1}$$

one can extract it as a characteristic constant of the medium [190]. The other parameters appearing in Equation C.1 are explicitlty defined as $\eta = k(1-\mu_s)$, $u = (2\ell_t)^{-1}(1+\mu_s^{-1})$, $\xi = (2/3)\ell_t$, $\mu_s = \cos\theta$, and $\alpha = k\sin\theta$.

The experimental setup used for collecting the backscattered intensity from the PGs is illustrated in the scheme of Figure C.1. It was designed so that the helicity conserving polarization was analyzed. Using a rotary motor, the sample was rotated around the optical axis so that each acquisition of the CCD camera corresponded to an average over several configurations of the sample. Otherwise, only one figure of speckle pattern is obtained on the CCD. Additionally, for each measurement, fifty cone images were collected and further averaged so that signal to noise ratio was improved. Profiles along the horizontal direction were extracted and processed into data values. The experimental results were fitted using Equation C.1 to determine ℓ_t.

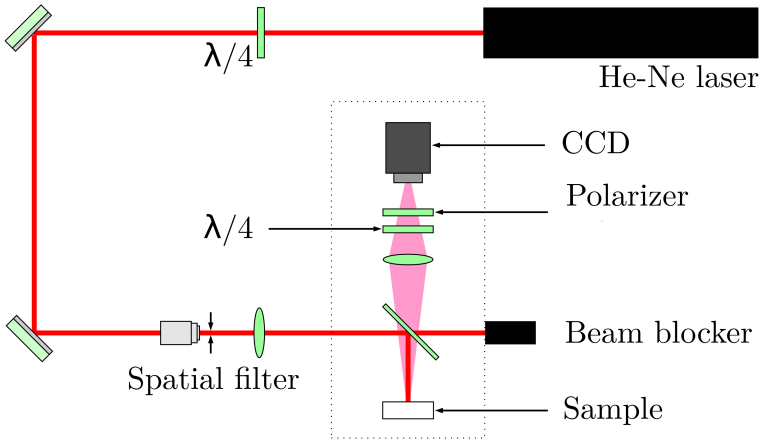

Figure C.1: Scheme of the optical setup used for collecting the backscattered intensity from diffusive samples. The label $\lambda/4$ stands for quarter wavelength plate.

D

Theoretical model for elastomeric grating

The model derived herein is valid for elastomeric gratings, both with and without SME. Nevertheless, in the former case, the stress could be released after stretching the structure (for what follows, it is assumed that shape relaxation is neglectable) while the deformation is preserved. The real periodic lattice is described by a two dimensional hexagonal Bravais lattice. As typically, one defines the primitive vectors of the basis ($\vec{a}_i$) according to the scheme of Figure D.1a. Mathematically, they can be expressed as:

$$\vec{a}_1 = d\,(1,0)\,, \tag{D.1}$$

$$\vec{a}_2 = d\left(-\frac{1}{2}, \frac{\sqrt{3}}{2}\right). \tag{D.2}$$

In the above equations, d is the diameter of the spheres used to grow the template crystals - see Section 4.2). Using the relation $\vec{a}_i \,.\, \vec{b}_j = 2\pi\delta_{ij}$, it is straightforward to calculate the primitive vectors $\vec{b}_i$ of the reciprocal lattice. After some algebra, it results:

$$\vec{b}_1 = \frac{2\pi}{d\sqrt{3}/2}\left(\frac{\sqrt{3}}{2}, \frac{1}{2}\right), \tag{D.3}$$

$$\vec{b}_2 = \frac{2\pi}{d\sqrt{3}/2}\,(0,1)\,. \tag{D.4}$$

Any vector $\vec{G}$ of the reciprocal lattice may be written as a linear combination of the vectors of the base as $\vec{G} = m_1\vec{b}_1 + m_2\vec{b}_2$, being m_i any integer numbers. Further, it is well known that, when light of wavelength λ interacts with a periodic interface, it is diffracted according to the Bragg condition:

$$\vec{\kappa}_{out\|}(\lambda) = \vec{\kappa}_{in\|}(\lambda) + \vec{G}, \tag{D.5}$$

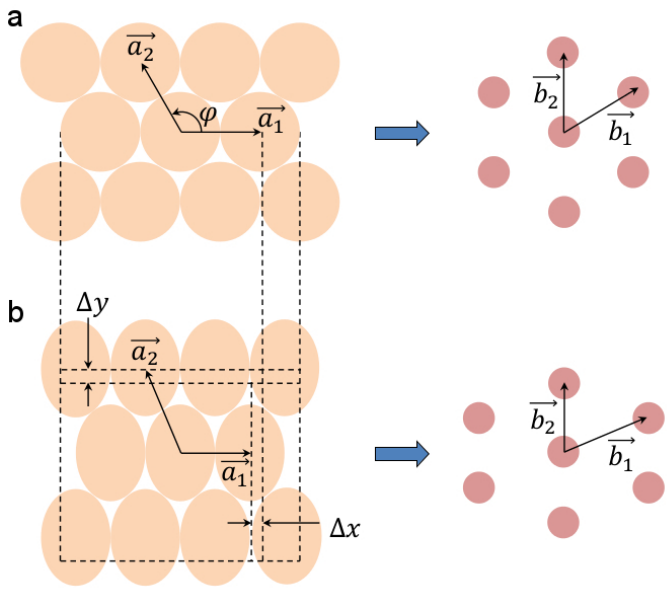

Figure D.1: Scheme illustrating the real (left) and reciprocal (right) lattices of a two dimensional hexagonal Bravais lattice, before (a) and after (b) being subjected to strain along the y direction.

where $\vec{\kappa}_{out\parallel}(\lambda) = (2\pi/\lambda)\sin\theta_d$ is the component of the wave vector of the diffracted light parallel to the grating and $\vec{\kappa}_{in\parallel}(\lambda) = (2\pi/\lambda)\sin\theta_{in}$ is the corresponding component of the incident wave vector (θ_d is the angle described between the diffracted ray and the normal to the surface). In our measurements, the incident angle is always $\theta_{in} = 0°$. From Equation D.5, one can obtain an expression for the first order diffraction angles (θ_{d1} and θ_{d2}) along the two principal symmetry directions:

$$\frac{2\pi}{\lambda}\sin\theta_{di} = \frac{2\pi}{\lambda}\sin\theta_{in} \pm m|\vec{b}_i| \Leftrightarrow \sin\theta_{di} = \pm\frac{2\lambda}{\sqrt{3}d}. \tag{D.6}$$

Naturally, the light probes the same lattice parameter along directions $\vec{a}_1$ and $\vec{a}_2$, for a perfectly symetric hexagonal grating. Therefore the modulus of the reciprocal primitive vectores are equal and the diffraction angles are the same ($\theta_{d1} = \theta_{d2}$).

Let us now analyze what happens after the sample being stretched and programed with a determined uniaxial strain, performed along the y direction (Figure D.1b). This is assumed to be the direction of growth of 2D colloidal crystals, which is taken as reference for straining in the actual experiments. In real materials, due to Poisson effect, this deformation will also induce strain along the orthogonal directions x and z (although the deformation along z

is not relevant for the present argument). The new basis vectors of the real lattice would change as

$$\vec{a}_1 = d(1,0) + (\Delta x, 0), \tag{D.7}$$

$$\vec{a}_2 = d\left(-\frac{1}{2}, \frac{\sqrt{3}}{2}\right) + \left(-\frac{\Delta x}{2}, \Delta y\right), \tag{D.8}$$

where Δx and Δy are half of the total deformations per unit cell. Furthermore, knowing that the strains along transverse and axial directions are related as $\varepsilon_x = -\upsilon\varepsilon_y$ (υ being the Poisson ratio), the expressions of the deformations can be re-written as a function of the strains:

$$\Delta x = -d\upsilon\frac{\varepsilon_y}{2}, \tag{D.9}$$

$$\Delta y = \frac{\sqrt{3}d}{2}\frac{\varepsilon_y}{2}. \tag{D.10}$$

Substituting Equation D.9 and Equation D.10 on the primitive vectors expressions (Equation D.7 and D.8), one obtains:

$$\vec{a}_1 = \left(d\left[1 - \upsilon\frac{\varepsilon_y}{2}\right], 0\right), \tag{D.11}$$

$$\vec{a}_2 = \frac{d}{2}\left(\upsilon\frac{\varepsilon_y}{2} - 1, \sqrt{3}\left[1 + \frac{\varepsilon_y}{2}\right]\right). \tag{D.12}$$

The validity of these expressions might be confirmed by substituting $\varepsilon_y = 0$ and recovering Equation D.1 and D.2. The new primitive vectors of the reciprocal lattice can thus be calculated, following the same reasoning as before, and departing from expressions D.11 and D.12:

$$\vec{b}_1 = \frac{2\pi}{d\sqrt{3}/2}\left(\frac{\sqrt{3}}{2[1 - \upsilon\varepsilon_y/2]}, \frac{1}{2[1 + \varepsilon_y/2]}\right), \tag{D.13}$$

$$\vec{b}_2 = \frac{2\pi}{d\sqrt{3}/2}\left(0, \frac{1}{1 + \varepsilon_y/2}\right). \tag{D.14}$$

Again using Equation D.6, the diffraction angles as determined as

$$\sin\theta_{d1} = \pm\left(\frac{\lambda}{2}\right)\left(\frac{1}{d\sqrt{3}/2}\right)\sqrt{\frac{3}{(1 - \upsilon\varepsilon_y/2)^2} + \frac{1}{(1 + \varepsilon_y/2)^2}}, \tag{D.15}$$

$$\sin\theta_{d2} = \pm\left(\frac{\lambda}{2}\right)\left(\frac{1}{d\sqrt{3}/2}\right)\left(\frac{2}{1 + \varepsilon_y/2}\right). \tag{D.16}$$

These equations allow a systematic study of the behavior of the elastic gratings in different scenarios, in view of their application as sensors of strain,

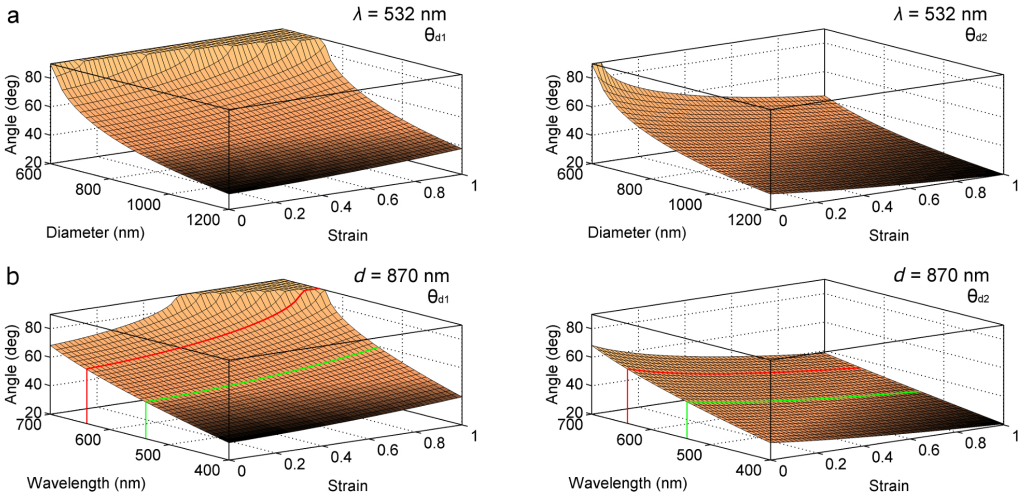

Figure D.2: a) Surface plots presenting the variation of angles θ_{d1} (left) and θ_{d2} (right) as a function of both the diameter of the spheres choosen for fabricating the template and the strain programed to the sample, at $\lambda = 532$ nm. b) Corresponding surface plots exhibiting the dependence of those angles on both the wavelength of the working radiation and the strain, for $d = 870$ nm.

for example. They determine the tailoring or programing parameters necessary for the preparation of the imprinted patterns, aiming a particular range of operation. In Figure D.2a, the dependence of the angles θ_{d1} and θ_{d2} on both d and set ε_y is presented for the case of $\lambda = 532$ nm, as lasers working at this wavelength are common in optical laboratories. As can be observed, θ_{d1} monotonously increases with the increase of ε_y, being this change more pronounced for low values of d. Besides, θ_{d2} is naturally equal to θ_{d1} for zero strain but, on the contrary, decreases monotonously with the increase of ε_y. At the referred wavelength, the range of angle variation for both directions is augmented when lower diameter spheres are used. This aspect is fundamental when designing a device or a sensor, as a wider range of variation increases resolution. This analysis also revealed that there is a limit for which the first-order diffracted angles become complex. This phenomenon is more clearly visible in the case of θ_{d1} (for a determined wavelength, this limit occurs at a higher strain as a higher d is employed for fabricating the template). Additionally, for a particular selected d, the cut-off will occur at a higher strain when lower wavelengths are used to probe the sample. On the contrary, in the case of θ_{d2}, the cut-off would occur for compression (negative values of strain) and not for stretching. The dependence of θ_{d1} and θ_{d2} on both the radiation wavelength used and strain applied is better appreciated

in Figure D.2b for the particular case of $d = 870$ nm (the diameter of spheres mainly discussed in the current chapter). Fixing d, it is clear that a higher wavelength favors a wider angle variation, although the cut-off strain would be lower. As an alternative to this approach, it would be possible to fix the geometry of the experimental setup and, in particular, the observation angle, for example with the use of an optical fiber, while impinging white light upon the sample. In this way, Equation D.15 and Equation D.16 could be used to preview the color observed as the PC is programed with different strains. In this sense, this system could be implemented as a deformation sensor or a reusable labelling machine to be optically read.

Bibliography

[1] S. John, "Strong localization of photons in certain disordered dielectric superlattices," *Physical Review Letters*, vol. 58, no. 23, pp. 2486–2489, 1987.

[2] E. Yablonovitch, "Inhibited spontaneous emission in solid-state physics and electronics," *Physical Review Letters*, vol. 58, no. 20, pp. 2059–2062, 1987.

[3] C. López, "Three-dimensional photonic bandgap materials: semiconductors for light," *Journal of Optics A*, vol. 8, no. 5, pp. R1–R14, 2006.

[4] A. Ledermann, L. Cademartiri, M. Hermatschweiler, C. Toninelli, G. Ozin, D. Wiersma, M. Wegener, and G. von Freymann, "Three-dimensional silicon inverse photonic quasicrystals for infrared wavelengths," *Nature Materials*, vol. 5, no. 12, pp. 942–945, 2006.

[5] L. Woodcock, "Entropy difference between crystal phases," *Nature*, vol. 388, no. 6639, pp. 236–237, 1997.

[6] R. Mayoral, J. Requena, J. S. Moya, C. López, A. Cintas, H. Míguez, F. Meseguer, L. Vázquez, M. Holgado, and A. Blanco, "3D long-range ordering in an SiO_2 submicrometer-sphere sintered superstructure," *Advanced Materials*, vol. 9, no. 3, pp. 257–260, 1997.

[7] M. Holgado, F. García-Santamaría, A. Blanco, M. Ibisate, A. Cintas, H. Míguez, C. J. Serna, C. Molpeceres, J. Requena, A. Mifsud,

F. Meseguer, and C. López, "Electrophoretic deposition to control artificial opal growth," *Langmuir*, vol. 15, no. 14, pp. 4701–4704, 1999.

[8] S. H. Park, D. Qin, and Y. Xia, "Crystallization of mesoscale particles over large areas," *Advanced Materials*, vol. 10, no. 13, pp. 1028–1032, 1998.

[9] S. Yang, H. Míguez, and G. Ozin, "Opal circuits of light-planarized microphotonic crystal chips," *Advanced Functional Materials*, vol. 12, no. 6-7, pp. 425–431, 2002.

[10] F. García-Santamaría, H. Miyazaki, A. Urquia, M. Ibisate, M. Belmonte, N. Shinya, F. Meseguer, and C. López, "Nanorobotic manipulation of microspheres for on-chip diamond architectures," *Advanced Materials*, vol. 14, no. 16, pp. 1144–1147, 2002.

[11] P. Jiang and M. McFarland, "Large-scale fabrication of wafer-size colloidal crystals, macroporous polymers and nanocomposites by spin-coating," *Journal of the American Chemical Society*, vol. 126, no. 42, pp. 13778–13786, 2004.

[12] O. Pursiainen, J. Baumberg, H. Winkler, B. Viel, P. Spahn, and T. Ruhl, "Shear-induced organization in flexible polymer opals," *Advanced Materials*, vol. 20, no. 8, pp. 1484–1487, 2008.

[13] P. Jiang, J. F. Bertone, K. S. Hwang, and V. L. Colvin, "Single-crystal colloidal multilayers of controlled thickness," *Chemistry of Materials*, vol. 11, no. 8, pp. 2132–2140, 1999.

[14] S. A. Asher, H. John, L. Liu, and Z. Wu, "Self-assembly motif for creating submicron periodic materials. polymerized crystalline colloidal arrays," *Journal of the American Chemical Society*, vol. 116, no. 11, pp. 4997–4998, 1994.

[15] C. I. Aguirre, E. Reguera, and A. Stein, "Tunable colors in opals and inverse opal photonic crystals," *Advanced Functional Materials*, vol. 20, no. 16, pp. 2565–2578, 2010.

[16] S. Nishimura, N. Abrams, B. Lewis, L. Halaoui, T. Mallouk, K. Benkstein, and A. Frank, "Standing wave enhancement of red absorbance and photocurrent in dye-sensitized titanium dioxide photoelectrodes coupled to photonic crystals," *Journal of the American Chemical Society*, vol. 125, no. 20, pp. 6306–6310, 2003.

[17] A. Esmanski and G. Ozin, "Silicon inverse opal based macroporous materials as negative electrodes for lithium ion batteries," *Advanced Functional Materials*, vol. 19, no. 12, pp. 1999–2010, 2009.

[18] S. Choi, J. Xie, and Y. Xia, "Chitosan-based inverse opals: three-dimensional scaffolds with uniform pore structures for cell culture," *Advanced Materials*, vol. 21, no. 29, pp. 2997–3001, 2009.

[19] Y. Vlasov, K. Luterova, I. Pelant, B. Hönerlage, and V. Astratov, "Enhancement of optical gain of semiconductors embedded in three-dimensional photonic crystals," *Applied Physics Letters*, vol. 71, no. 12, pp. 1616–1618, 1997.

[20] R. Sapienza, P. D. García, J. Bertolotti, M. Martín, A. Blanco, L. Viña, C. López, and D. S. Wiersma, "Observation of resonant behavior in the energy velocity of diffused light," *Physical Review Letters*, vol. 99, no. 23, p. 233902, 2007.

[21] O. Svelto, *Principles of lasers*. New York: Springer-Verlag, 2010.

[22] M. Leonetti, R. Sapienza, M. Ibisate, C. Conti, and C. López, "Optical gain in DNA-DCM for lasing in photonic materials," *Optics letters*, vol. 34, no. 24, pp. 3764–6, 2009.

[23] K. Sakoda, *Optical properties of photonic crystals*. Berlin: Springer-Verlag, 2005.

[24] C. López, "Materials aspects of photonic crystals," *Advanced Materials*, vol. 15, no. 20, pp. 1679–1704, 2003.

[25] X. Liu, Y. Wang, B. Cheng, and D. Zhang, "Conservative form of the density of states of a photonic crystal with a pseudogap," *Physical Review E*, vol. 68, no. 3, p. 036610, 2003.

[26] Y. Nishijima, K. Ueno, S. Juodkazis, V. Mizeikis, H. Fujiwara, K. Sasaki, and H. Misawa, "Lasing with well-defined cavity modes in dye-infiltrated silica inverse opals," *Optics Express*, vol. 17, no. 4, pp. 2976–2983, 2009.

[27] S. Furumi, "Active lasing from organic colloidal photonic crystals," *Journal of Materials Chemistry C*, vol. 1, pp. 6003–6012, 2013.

[28] P. D. García and C. López, "From Bloch to random lasing in ZnO self-assembled nanostructures," *Journal of Materials Chemistry C*, vol. 1, pp. 7357–7362, 2013.

[29] D. S. Wiersma, "The physics and applications of random lasers," *Nature Physics*, vol. 4, no. 5, pp. 359–367, 2008.

[30] R. Ambartsumyan, N. Basov, P. Kryukov, and V. Letokhov, "A laser with a nonresonant feedback," *IEEE Journal of Quantum Electronics*, vol. 2, no. 9, pp. 442–446, 1966.

[31] H. Cao, "Lasing in random media," *Waves in Random Media*, vol. 13, no. 3, pp. R1–R39, 2003.

[32] J. Liu, P. D. García, S. Ek, N. Gregersen, T. Suhr, M. Schubert, J. Mork, S. Stobbe, and P. Lodahl, "Random nanolasing in the Anderson localized regime," *Nature Nanotechnology*, vol. 9, no. 4, pp. 285–289, 2014.

[33] X. Shi, Y. Wang, Z. Wang, S. Wei, Y. Sun, D. Liu, J. Zhou, Y. Zhang, and J. Shi, "Random lasing with a high quality factor over the whole visible range based on cascade energy transfer," *Advanced Optical Materials*, vol. 2, no. 1, pp. 88–93, 2014.

[34] B. Redding, M. Choma, and H. Cao, "Speckle-free laser imaging using random laser illumination," *Nature Photonics*, vol. 6, no. 6, pp. 355–359, 2012.

[35] H. Cao, Y. G. Zhao, S. Ho, E. Seelig, Q. Wang, and R. Chang, "Random laser action in semiconductor powder," *Physical Review Letters*, vol. 82, no. 11, pp. 2278–2281, 1999.

[36] N. Lawandy, R. Balachandran, A. Gomes, and E. Sauvain, "Laser action in strongly scattering media," *Nature*, vol. 368, no. 6470, pp. 436–438, 1994.

[37] I. Viola, N. Ghofraniha, A. Zacheo, V. Arima, C. Conti, and G. Gigli, "Random laser emission from a paper-based device," *Journal of Materials Chemistry C*, vol. 1, no. 48, p. 8128, 2013.

[38] Y. Ling, H. Cao, A. Burin, M. Ratner, X. Liu, and R. Chang, "Investigation of random lasers with resonant feedback," *Physical Review A*, vol. 64, no. 6, p. 063808, 2001.

[39] A. Tulek, R. C. Polson, and Z. V. Vardeny, "Naturally occurring resonators in random lasing of pi-conjugated polymer films," *Nature Physics*, vol. 6, no. 4, pp. 303–310, 2010.

[40] C. Kallinger, M. Hilmer, A. Haugeneder, M. Perner, W. Spirkl, U. Lemmer, J. Feldmann, U. Scherf, K. Müllen, A. Gombert, and V. Wittwer, "A flexible conjugated polymer laser," *Advanced Materials*, vol. 10, no. 12, pp. 920–923, 1998.

[41] P. D. García, R. Sapienza, A. Blanco, and C. López, "Photonic glass: a novel random material for light," *Advanced Materials*, vol. 19, no. 18, pp. 2597–2602, 2007.

[42] S. Gottardo, R. Sapienza, A. Blanco, D. S. Wiersma, and C. López, "Resonance-driven random lasing," *Nature Photonics*, vol. 2, no. 7, pp. 429–432, 2008.

[43] L. C. Chang and T. A. Read, "Plastic deformation and diffusionless phase changes in metals - the Gold-Cadmium beta-phase," *Transactions of the American Institute of Mining and Metallurgical Engineers*, vol. 191, no. 1, pp. 47–52, 1951.

[44] B. Kim, S. Lee, and M. Xu, "Polyurethanes having shape memory effects," *Polymer*, vol. 37, no. 26, pp. 5781–5793, 1996.

[45] Y. Osada and A. Matsuda, "Shape-memory in hydrogels," *Nature*, vol. 376, no. 6537, p. 219, 1995.

[46] A. Lendlein and S. Kelch, "Shape-memory polymers," *Angewandte Chemie*, vol. 41, no. 12, pp. 2034–2057, 2002.

[47] M. Behl and A. Lendlein, "Shape-memory polymers," *Materials Today*, vol. 10, no. 4, pp. 20–28, 2007.

[48] M. C. Serrano, L. Carbajal, and G. Ameer, "Novel biodegradable shape-memory elastomers with drug-releasing capabilities," *Advanced Materials*, vol. 23, no. 19, pp. 2211–2215, 2011.

[49] I. Bellin, S. Kelch, R. Langer, and A. Lendlein, "Polymeric triple-shape materials," *Proceedings of the National Academy of Sciences of the United States of America*, vol. 103, no. 48, pp. 18043–7, 2006.

[50] J. W. Cho, J. W. Kim, Y. C. Jung, and N. S. Goo, "Electroactive shape-memory polyurethane composites incorporating carbon nanotubes," *Macromolecular Rapid Communications*, vol. 26, no. 5, pp. 412–416, 2005.

[51] T. Weigel, R. Mohr, and A. Lendlein, "Investigation of parameters to achieve temperatures required to initiate the shape-memory effect of magnetic nanocomposites by inductive heating," *Smart Materials and Structures*, vol. 18, no. 2, p. 025011, 2009.

[52] A. Lendlein, H. Jiang, O. Junger, and R. Langer, "Light-induced shape-memory polymers," *Nature*, vol. 434, no. 7035, pp. 879–882, 2005.

[53] P. Jiang, "Large-scale fabrication of periodic nanostructured materials by using hexagonal non-close-packed colloidal crystals as templates," *Langmuir*, vol. 22, no. 9, pp. 3955–3958, 2006.

[54] R. Yoshida, K. Uchida, Y. Kaneko, K. Sakai, A. Kikuchi, Y. Sakurai, and T. Okano, "Comb-type grafted hydrogels with rapid de-swelling response to temperature changes," *Nature*, vol. 374, no. 6519, pp. 240–242, 1995.

[55] A. Lendlein and R. Langer, "Biodegradable, elastic shape-memory polymers for potential biomedical applications," *Science*, vol. 296, no. 5573, pp. 1673–1676, 2002.

[56] M. Behl, M. Y. Razzaq, and A. Lendlein, "Multifunctional shape-memory polymers," *Advanced Materials*, vol. 22, no. 31, pp. 3388–3410, 2010.

[57] A. Lendlein and V. P. Shastri, "Stimuli-sensitive polymers," *Advanced Materials*, vol. 22, no. 31, pp. 3344–3347, 2010.

[58] D. J. Maitland, W. Small, J. M. Ortega, P. R. Buckley, J. Rodriguez, J. Hartman, and T. S. Wilson, "Prototype laser-activated shape memory polymer foam device for embolic treatment of aneurysms," *Journal of Biomedical Optics*, vol. 12, no. 3, p. 030504, 2007.

[59] M. Behl and A. Lendlein, "Triple-shape polymers," *Journal of Materials Chemistry*, vol. 20, p. 3335, 2010.

[60] J. Kunzelman, T. Chung, P. Mather, and C. Weder, "Shape memory polymers with built-in threshold temperature sensors," *Journal of Materials Chemistry*, vol. 18, pp. 1082–1086, 2008.

[61] J. Hu, *Shape memory polymers and textiles*. Cambridge: Woodhead Publishing Limited, 2007.

[62] W. Huang, C. Lee, and H. Teo, "Thermomechanical behavior of a polyurethane shape memory polymer foam," *Journal of Intelligent Material Systems and Structures*, vol. 17, no. 8, pp. 753–760, 2006.

[63] Y. Fang, Y. Ni, B. Choi, S.-Y. Leo, J. Gao, B. Ge, C. Taylor, V. Basile, and P. Jiang, "Chromogenic photonic crystals enabled by novel vapor-responsive shape-memory polymers," *Advanced Materials*, pp. n/a–n/a, 2015.

[64] J. F. Galisteo-López, M. Ibisate, R. Sapienza, L. S. Froufe-Pérez, A. Blanco, and C. López, "Self-assembled photonic structures," *Advanced Materials*, vol. 23, no. 1, pp. 30–69, 2011.

[65] T. Mitsui, Y. Wakayama, T. Onodera, T. Hayashi, N. Ikeda, Y. Sugimoto, T. Takamasu, and H. Oikawa, "Micro-demultiplexer of coupled resonator optical waveguide fabricated by microspheres," *Advanced Materials*, vol. 22, no. 28, pp. 3022–6, 2010.

[66] P. Kumnorkaew, Y. Ee, N. Tansu, and J. Gilchrist, "Investigation of the deposition of microsphere monolayers for fabrication of microlens arrays," *Langmuir*, vol. 24, no. 21, pp. 12150–12157, 2008.

[67] M. López-García, J. F. Galisteo-López, A. Blanco, J. Sánchez-Marcos, C. López, and A. García-Martín, "Enhancement and directionality of spontaneous emission in hybrid self-assembled photonic-plasmonic crystals," *Small*, vol. 6, no. 16, pp. 1757–1761, 2010.

[68] H. Deckman and J. Dunsmuir, "Natural lithography," *Applied Physics Letters*, vol. 41, no. 4, pp. 377–379, 1982.

[69] D. Wang and H. Möhwald, "Rapid fabrication of binary colloidal crystals by stepwise spin-coating," *Advanced Materials*, vol. 16, no. 3, pp. 244–247, 2004.

[70] A. Emoto, E. Uchida, and T. Fukuda, "Fabrication and optical properties of binary colloidal crystal monolayers consisting of micro- and nano-polystyrene spheres," *Colloids and Surfaces A*, vol. 396, pp. 189–194, 2012.

[71] Y. Li, W. Cai, and G. Duan, "Ordered micro/nanostructured arrays based on the monolayer colloidal crystals," *Chemistry of Materials*, vol. 20, no. 3, pp. 615–624, 2008.

[72] G. Zhang and D. Wang, "Ordered binary arrays of Au nanoparticles derived from colloidal lithography," *Nano Letters*, vol. 7, no. 1, pp. 127–132, 2007.

[73] Y. Kurokawa, H. Miyazaki, and Y. Jimba, "Light scattering from a monolayer of periodically arrayed dielectric spheres on dielectric substrates," *Physical Review B*, vol. 65, no. 20, p. 201102, 2002.

[74] V. Canalejas-Tejero, M. Ibisate, D. Golmayo, A. Blanco, and C. López, "Qualitative and quantitative analysis of crystallographic defects present in 2D colloidal sphere arrays," *Langmuir*, vol. 28, no. 1, pp. 161–167, 2011.

[75] P. Born, S. Blum, A. Munoz, and T. Kraus, "Role of the meniscus shape in large-area convective particle assembly," *Langmuir*, vol. 27, no. 14, pp. 8621–8633, 2011.

[76] J. Sun, C. Tang, P. Zhan, Z. Han, Z. Cao, and Z. L. Wang, "Fabrication of centimeter-sized single-domain two-dimensional colloidal crystals in a wedge-shaped cell under capillary forces," *Langmuir*, vol. 26, no. 11, pp. 7859–7864, 2010.

[77] J. Zhang, Y. Li, X. Zhang, and B. Yang, "Colloidal self-assembly meets nanofabrication: from two-dimensional colloidal crystals to nanostructure arrays," *Advanced Materials*, vol. 22, no. 38, pp. 4249–69, 2010.

[78] L. Jia and W. Cai, "Micro/nanostructured ordered porous films and their structurally induced control of the gas sensing performances," *Advanced Functional Materials*, vol. 20, no. 21, pp. 3765–3773, 2010.

[79] Y. Li and E. J. Lee, "Superhydrophobic coatings on curved surfaces featuring remarkable supporting force," *The Journal of Physical Chemistry C*, vol. 111, no. 40, pp. 14813–14817, 2007.

[80] C. Li, G. Hong, and L. Qi, "Nanosphere lithography at the gas/liquid interface: a general approach toward free-standing high-quality nanonets," *Chemistry of Materials*, vol. 22, no. 2, pp. 476–481, 2010.

[81] T. Tatsuma, A. Ikezawa, Y. Ohko, and T. Miwa, "Microstructured TiO_2 templates for the preparation of size-controlled bryopsis protoplasts as cell models," *Advanced Materials*, vol. 12, no. 9, pp. 643–646, 2000.

[82] E. Min, K. H. Wong, and M. Stenzel, "Microwells with patterned proteins by a self-assembly process using honeycomb-structured porous films," *Advanced Materials*, vol. 20, no. 18, pp. 3550–3556, 2008.

[83] Y. Li, W. Cai, G. Duan, F. Sun, B. Cao, F. Lu, Q. Fang, and I. W. Boyd, "Large-area In_2O_3 ordered pore arrays and their photoluminescence properties," *Applied Physics A*, vol. 81, no. 2, pp. 269–273, 2005.

[84] J. Yang, G. Duan, and W. Cai, "Controllable fabrication and tunable magnetism of Nickel nanostructured ordered porous arrays," *The Journal of Physical Chemistry C*, vol. 113, no. 10, pp. 3973–3977, 2009.

[85] F. Sun, W. Cai, Y. Li, B. Cao, Y. Lei, and L. Zhang, "Morphology-controlled growth of large-area two-dimensional ordered pore arrays," *Advanced Functional Materials*, vol. 14, no. 3, pp. 283–288, 2004.

[86] Y. Li, W. Cai, B. Cao, G. Duan, C. Li, F. Sun, and H. Zeng, "Morphology-controlled 2D ordered arrays by heating-induced deformation of 2D colloidal monolayer," *Journal of Materials Chemistry*, vol. 16, no. 6, p. 609, 2006.

[87] S. Yang, W. Cai, J. Yang, and H. Zeng, "General and simple route to micro/nanostructured hollow-sphere arrays based on electrophoresis of colloids induced by laser ablation in liquid," *Langmuir*, vol. 25, no. 14, pp. 8287–91, 2009.

[88] F. Sun and J. Yu, "Photochemical preparation of two-dimensional gold spherical pore and hollow sphere arrays on a solution surface," *Angewandte Chemie International Edition*, vol. 46, no. 5, pp. 773–777, 2007.

[89] T. Zhang, J. Qian, X. Tuo, J. Yuan, and X. Wang, "Fabricating ordered porous monolayers from colloidal monolayer and multilayer," *Colloids and Surfaces A*, vol. 335, no. 1-3, pp. 202–206, 2009.

[90] L. Landström, N. Arnold, D. Brodoceanu, K. Piglmayer, and D. Bäuerle, "Photonic properties of silicon-coated monolayers of colloidal silica microspheres," *Applied Physics A*, vol. 83, no. 2, pp. 271–275, 2006.

[91] W. J. Hyun, H. K. Lee, S. S. Oh, O. Hess, C. Choi, S. H. Im, and O. O. Park, "Two-dimensional TiO_2 inverse opal with a closed top surface structure for enhanced light extraction from polymer light-emitting diodes," *Advanced Materials*, vol. 23, no. 16, pp. 1846–50, 2011.

[92] Y. Li and N. Koshizaki, "Periodic one-dimensional nanostructured arrays based on colloidal templates, applications, and devices," *Coordination Chemistry Reviews*, vol. 255, no. 3-4, pp. 357–373, 2011.

[93] A. Blanco and C. López, "Silicon onion-layer nanostructures arranged in three dimensions," *Advanced Materials*, vol. 18, no. 12, pp. 1593–1597, 2006.

[94] B. Hatton, L. Mishchenko, S. Davis, K. H. Sandhage, and J. Aizenberg, "Assembly of large-area, highly ordered, crack-free inverse opal films," *PNAS*, vol. 107, no. 23, pp. 1–6, 2010.

[95] Y. Li, W. Cai, B. Cao, G. Duan, F. Sun, C. Li, and L. Jia, "Two-dimensional hierarchical porous silica film and its tunable superhydrophobicity," *Nanotechnology*, vol. 17, no. 1, pp. 238–243, 2006.

[96] Z. Lu, A. Namboodiri, and M. M. Collinson, "Self-supporting nanopore membranes with controlled pore size and shape," *ACS Nano*, vol. 2, no. 5, pp. 993–9, 2008.

[97] K. L. Wu and S. K. Lai, "Theoretical studies of the early stage coagulation kinetics for a charged colloidal dispersion," *Langmuir*, vol. 21, no. 8, pp. 3238–3246, 2005.

[98] M. López-García, J. F. Galisteo-López, C. López, and A. García-Martín, "Light confinement by two-dimensional arrays of dielectric spheres," *Physical Review B*, vol. 85, no. 23, pp. 1–5, 2012.

[99] Z. Bao, M. Weatherspoon, S. Shian, and Y. Cai, "Chemical reduction of three-dimensional silica micro-assemblies into microporous silicon replicas," *Nature*, vol. 446, pp. 172–175, 2007.

[100] Z. Xia, S. Davis, A. Eftekhar, A. Gordin, M. Askari, Q. Li, F. Ghasemi, K. H. Sandhage, and A. Adibi, "Magnesiothermically formed porous silicon thin films on silicon-on-insulator optical microresonators for high-sensitivity detection," *Advanced Optical Materials*, vol. 2, no. 3, pp. 235–239, 2014.

[101] M. Ibisate, D. Golmayo, and C. López, "Silicon direct opals," *Advanced Materials*, vol. 21, no. 28, pp. 2899–2902, 2009.

[102] R. M. Cole, S. Mahajan, and J. Baumberg, "Stretchable metal-elastomer nanovoids for tunable plasmons," *Applied Physics Letters*, vol. 95, no. 15, p. 154103, 2009.

[103] S. V. Boriskina, M. Povinelli, V. N. Astratov, A. V. Zayats, and V. a. Podolskiy, "Collective phenomena in photonic, plasmonic and hybrid structures," *Optics Express*, vol. 19, no. 22, p. 22024, 2011.

[104] M. Otto, M. Algasinger, H. Branz, B. Gesemann, T. Gimpel, K. Füchsel, T. Käsebier, S. Kontermann, S. Koynov, X. Li, V. Naumann, J. Oh, A. N. Sprafke, J. Ziegler, M. Zilk, and R. B. Wehrspohn, "Black silicon photovoltaics," *Advanced Optical Materials*, vol. 3, no. 2, pp. 147–164, 2015.

[105] A. G. Cullis, L. T. Canham, and P. Calcott, "The structural and luminescence properties of porous silicon," *Journal of Applied Physics*, vol. 82, no. 3, pp. 909–965, 1997.

[106] F. Gallego-Gómez, M. Ibisate, D. Golmayo, F. Palomares, M. Herrera, J. Hernández, S. Molina, A. Blanco, and C. López, "Light emission from nanocrystalline Si inverse opals and controlled passivation by atomic layer deposited Al_2O_3," *Advanced Materials*, vol. 23, no. 44, pp. 5219–5223, 2011.

[107] H. Kim, B. Han, J. Choo, and J. Cho, "Three-dimensional porous silicon particles for use in high-performance lithium secondary batteries," *Angewandte Chemie*, vol. 120, no. 52, pp. 10305–10308, 2008.

[108] M. Barth, A. Gruber, and F. Cichos, "Spectral and angular redistribution of photoluminescence near a photonic stop band," *Physical Review B*, vol. 72, no. 8, p. 085129, 2005.

[109] P. Lodahl, A. V. Driel, I. Nikolaev, and A. Irman, "Controlling the dynamics of spontaneous emission from quantum dots by photonic crystals," *Nature*, vol. 430, no. 7000, pp. 654–657, 2004.

[110] H. Ning, A. Mihi, J. B. Geddes, M. Miyake, and P. V. Braun, "Radiative lifetime modification of LaF_3:Nd nanoparticles embedded in 3D silicon photonic crystals," *Advanced Optical Materials*, vol. 24, no. 23, pp. OP153–158, 2012.

[111] S. Gaponenko, V. Bogomolov, E. Petrov, A. Kapitonov, D. Yarotsky, and F. Gindele, "Spontaneous emission of dye molecules, semiconductor nanocrystals, and rare-earth ions in opal-based photonic crystals," *Journal of Lightwave Technology*, vol. 17, no. 11, pp. 2128–2137, 1999.

[112] M. Ajgaonkar, Y. Zhang, H. Grebel, M. Sosnowski, and D. C. Jacobson, "Linear and nonlinear optical properties of erbium-implanted coherent

array of submicron silica spheres," *Applied Physics Letters*, vol. 76, no. 26, p. 3876, 2000.

[113] S. Romanov, A. Fokin, and R. De La Rue, "Eu^{3+} emission in an anisotropic photonic band gap environment," *Applied Physics Letters*, vol. 76, no. 13, p. 1656, 2000.

[114] G. N. Aliev, V. G. Golubev, A. A. Dukin, D. A. Kurdyukov, and A. V. Medvedev, "Structural, photonic band-gap, and luminescence properties of the opal-erbium composite," *Physics of the Solid State*, vol. 44, no. 12, pp. 2224–2231, 2002.

[115] R. Withnall, M. I. Martinez-Rubio, G. R. Fern, T. G. Ireland, and J. Silver, "Photonic phosphors based on cubic Y_2O_3:Tb^{3+} infilled into a synthetic opal lattice," *Journal of Optics A*, vol. 5, no. 4, pp. S81–S85, 2003.

[116] M. Y. Tsvetkov, S. M. Kleshcheva, M. I. Samoilovich, N. V. Gaponenko, and A. N. Shushunov, "Erbium photoluminescence in opal matrix and porous anodic alumina nanocomposites," *Microelectronic Engineering*, vol. 81, no. 2-4, pp. 273–280, 2005.

[117] M. de Dood, C. M. V. Kats, and A. Polman, "Acid-based synthesis of monodisperse rare-earth-doped colloidal SiO_2 spheres," *Chemistry of Materials*, vol. 14, no. 7, pp. 2849–2853, 2002.

[118] L. Li, C. Tsung, Z. Yang, and G. Stucky, "Rare-earth-doped nanocrystalline Titania microspheres emitting luminescence via energy transfer," *Advanced Materials*, vol. 20, no. 5, pp. 903–908, 2008.

[119] Z. Yang, J. Zhou, X. Huang, G. Yang, Q. Xie, L. Sun, B. Li, and L. Li, "Photonic band gap and photoluminescence properties of $LaPO_4$:Tb inverse opal," *Chemical Physics Letters*, vol. 455, no. 1-3, pp. 55–58, 2008.

[120] M. Li, P. Zhang, J. Li, and J. Zhou, "Directional emission from rare earth ions in inverse photonic crystals," *Applied Physics B*, vol. 89, no. 2-3, pp. 251–255, 2007.

[121] M. Aloshyna, S. Sivakumar, M. Venkataramanan, A. Brolo, and F. van Veggel, "Significant suppression of spontaneous emission in SiO_2 photonic crystals made with Tb^{3+}-doped LaF_3 nanoparticles," *Journal of Physical Chemistry C*, vol. 111, no. 10, pp. 4047–4051, 2007.

[122] M. C. Gonçalves, L. Fortes, R. M. Almeida, A. Chiasera, A. Chiappini, and M. Ferrari, "3D rare earth-doped colloidal photonic crystals," *Optical Materials*, vol. 31, no. 9, pp. 1315–1318, 2009.

[123] J. Kalkman, E. de Bres, A. Polman, Y. Jun, D. J. Norris, and A. van Blaaderen, "Selective excitation of erbium in silicon-infiltrated silica colloidal photonic crystals," *Journal of Applied Physics*, vol. 95, no. 5, p. 2297, 2004.

[124] Z. Yang, D. Yan, H. Wu, R. Wang, Z. Song, D. Zhou, X. Yu, Y. Yang, Z. Yin, L. Yan, and J. Qiu, "Photoluminescence in Gd_2O_3: Er^{3+}, Yb^{3+} upconversion inverse opal," *Journal of Physics and Chemistry of Solids*, vol. 73, no. 11, pp. 1278–1281, 2012.

[125] Z. Yang, D. Yan, K. Zhu, Z. Song, X. Yu, D. Zhou, Z. Yin, and J. Qiu, "Modification of the upconversion spontaneous emission in photonic crystals," *Materials Chemistry and Physics*, vol. 133, no. 2-3, pp. 584–587, 2012.

[126] J. A. Sánchez-Martín, J. A. Abenia, M. A. Rebolledo, M. V. Andrés, and A. Díez, "Amplifiers and lasers based on Erbium-doped photonic crystal fiber: simulation and experiments," *IEEE Journal of Quantum Electronics*, vol. 48, no. 3, pp. 338–344, 2012.

[127] E. Cantelar and J. Muñoz, "Yb^{3+} to Er^{3+} energy transfer in $LiNbO_3$," *Journal of Physics: Condensed Matter*, vol. 10, no. 39, pp. 8893–8903, 1998.

[128] J. Päiväsaari, M. Putkonen, T. Sajavaara, and L. Niinistö, "Atomic layer deposition of rare earth oxides: Erbium oxide thin films from β-diketonate and ozone precursors," *Journal of Alloys and Compounds*, vol. 374, no. 1-2, pp. 124–128, 2004.

[129] M. C. Gonçalves, L. Fortes, R. M. Almeida, A. Chiasera, A. Chiappini, M. Ferrari, and S. Bhaktha, "Photoluminescence in Er^{3+}/Yb^{3+} doped silica-titania inverse opal structures," *Journal of Sol-Gel Science and Technology*, vol. 55, no. 1, pp. 52–58, 2010.

[130] S. Johnson and J. Joannopoulos, "MIT Photonic-Bands."

[131] D. J. Norris, E. G. Arlinghaus, L. Meng, R. Heiny, and L. E. Scriven, "Opaline photonic crystals: How does self-assembly work?," *Advanced Materials*, vol. 16, no. 16, pp. 1393–1399, 2004.

[132] N. Denkov, O. Velev, P. Kralchevski, I. Ivanov, H. Yoshimura, and K. Nagayama, "Mechanism of formation of two-dimensional crystals from latex particles on substrates," *Langmuir*, vol. 8, no. 12, pp. 3183–3190, 1992.

[133] L. Hench and J. West, "The sol-gel process," *Chemical Reviews*, vol. 90, no. 1, pp. 33–72, 1990.

[134] W. Stöber, A. Fink, and E. Bohn, "Controlled growth of monodisperse silica spheres in the micron size range," *Journal of Colloid and Interface Science*, vol. 26, no. 1, pp. 62–69, 1968.

[135] J. F. Galisteo-López, E. Palacios-Lidón, E. Castillo-Martínez, and C. López, "Optical study of the pseudogap in thickness and orientation controlled artificial opals," *Physical Review B*, vol. 68, p. 115109, 2003.

[136] Q. Nie, L. Lu, T. Xu, S. Dai, X. Shen, X. Liang, X. Zhang, and X. Zhang, "Effect of hydroxyl groups on Er^{3+} doped Bi_2O_3-B_2O_3-SiO_2 glasses," *Journal of Physics and Chemistry of Solids*, vol. 68, no. 4, pp. 477–481, 2007.

[137] L. Fortes, Y. Li, R. Réfega, and M. C. Gonçalves, "Up-conversion in rare earth-doped silica hollow spheres," *Optical Materials*, vol. 34, no. 8, pp. 1440–1446, 2012.

[138] F. Meseguer, A. Blanco, H. Míguez, F. García-Santamaría, M. Ibisate, and C. López, "Synthesis of inverse opals," *Colloids and Surfaces A: Physicochemical and Engineering Aspects*, vol. 202, no. 2-3, pp. 281–290, 2002.

[139] Y. Zhang and Y. Xia, "Formation of embryoid bodies with controlled sizes and maintained pluripotency in three-dimensional inverse opal scaffolds," *Advanced Functional Materials*, vol. 22, no. 1, pp. 121–129, 2012.

[140] K. Lee and S. Asher, "Photonic crystal chemical sensors: pH and ionic strength," *Journal of the American Chemical Society*, vol. 15260, no. 14, pp. 9534–9537, 2000.

[141] Y.-J. Lee, S. a. Pruzinsky, and P. V. Braun, "Glucose-sensitive inverse opal hydrogels: analysis of optical diffraction response," *Langmuir*, vol. 20, no. 8, pp. 3096–3106, 2004.

[142] M. Ren, R. Ravikrishna, and K. T. Valsaraj, "Photocatalytic degradation of gaseous organic species on photonic band-gap titania," *Environmental Science and Technology*, vol. 40, no. 22, pp. 7029–7033, 2006.

[143] A. Blanco, E. Chomski, S. Grabtchak, and M. Ibisate, "Large-scale synthesis of a silicon photonic crystal with a complete three-dimensional bandgap near 1.5 micrometres," *Nature*, vol. 405, pp. 437–440, 2000.

[144] A. Arsenault, T. J. Clark, G. von Freymann, L. Cademartiri, R. Sapienza, J. Bertolotti, E. Vekris, S. Wong, V. Kitaev, I. Manners, R. Z. Wang, S. John, D. S. Wiersma, and G. Ozin, "From colour fingerprinting to the control of photoluminescence in elastic photonic crystals," *Nature Materials*, vol. 5, no. 3, pp. 179–184, 2006.

[145] A. van Driel, I. Nikolaev, P. Vergeer, P. Lodahl, D. Vanmaekelbergh, and W. Vos, "Statistical analysis of time-resolved emission from ensembles of semiconductor quantum dots: interpretation of exponential decay models," *Physical Review B*, vol. 75, no. 3, p. 035329, 2007.

[146] A. Blanco, C. López, R. Mayoral, H. Míguez, F. Meseguer, A. Mifsud, and J. Herrero, "Cds photoluminescence inhibition by a photonic structure," *Applied Physics Letters*, vol. 73, no. 13, pp. 1781–1783, 1998.

[147] T. Altebaeumer, B. Gotsmann, H. Pozidis, A. Knoll, and U. Duerig, "Nanoscale shape-memory function in highly cross-linked polymers," *Nano Letters*, vol. 8, no. 12, pp. 4398–4403, 2008.

[148] J. L. Wilbur, R. J. Jackman, G. M. Whitesides, E. L. Cheung, L. K. Lee, and M. Prentiss, "Elastomeric optics," *Chemistry of Materials*, vol. 8, no. 7, pp. 1380–1385, 1996.

[149] B. Viel, T. Ruhl, and G. P. Hellmann, "Reversible deformation of opal elastomers," *Chemistry of Materials*, vol. 19, no. 23, pp. 5673–5679, 2007.

[150] J. M. Jethmalani and W. T. Ford, "Diffraction of visible light by ordered monodisperse silica - poly(methylacrylate) composite films," *Chemistry of Materials*, vol. 8, no. 8, pp. 2138–2146, 1996.

[151] J. Jang, C. K. Ullal, T. Gorishnyy, V. V. Tsukruk, and E. L. Thomas, "Mechanically tunable three-dimensional elastomeric network/air structures via interference lithography," *Nano Letters*, vol. 6, no. 4, pp. 740–3, 2006.

[152] M. E. Calvo and H. Míguez, "Flexible, adhesive, and biocompatible bragg mirrors based on polydimethylsiloxane infiltrated nanoparticle multilayers," *Chemistry of Materials*, vol. 22, no. 13, pp. 3909–3915, 2010.

[153] J. R. C. Smirnov, M. E. Calvo, and H. Míguez, "Selective UV reflecting mirrors based on nanoparticle multilayers," *Advanced Functional Materials*, vol. 23, no. 22, pp. 2805–2811, 2013.

[154] J. Liang, L. Li, X. Niu, Z. Yu, and Q. Pei, "Elastomeric polymer light-emitting devices and displays," *Nature Photonics*, vol. 7, pp. 3–10, 2013.

[155] J. Yang, R. Webb, and G. Ameer, "Novel citric acid-based biodegradable elastomers for tissue engineering," *Advanced Materials*, vol. 16, no. 6, pp. 511–516, 2004.

[156] Y. Xia and G. M. Whitesides, "Soft lithography," *Angewandte Chemie International Edition*, vol. 37, no. 5, pp. 550–575, 1998.

[157] D. Losic, J. G. Mitchell, R. Lal, and N. H. Voelcker, "Rapid fabrication of micro and nanoscale patterns by replica molding from diatom biosilica," *Advanced Functional Materials*, vol. 17, no. 14, pp. 2439–2446, 2007.

[158] G. Wu, Y. Jiang, D. Xu, H. Tang, X. Liang, and G. Li, "Thermoresponsive inverse opal films fabricated with liquid-crystal elastomers and nematic liquid crystals," *Langmuir*, vol. 27, no. 4, pp. 1505–9, 2011.

[159] C. G. Schäfer, M. Gallei, J. T. Zahn, J. Engelhardt, G. P. Hellmann, and M. Rehahn, "Reversible light-, thermo-, and mechano-responsive elastomeric polymer opal films," *Chemistry of Materials*, vol. 25, no. 11, pp. 2309–2318, 2013.

[160] D. J. D. Davies, A. R. Vaccaro, S. M. Morris, N. Herzer, A. P. H. J. Schenning, and C. W. M. Bastiaansen, "A printable optical time-temperature integrator based on shape memory in a chiral nematic polymer network," *Advanced Functional Materials*, vol. 23, no. 21, pp. 2723–2727, 2013.

[161] T. Xie, X. Xiao, J. Li, and R. Wang, "Encoding localized strain history through wrinkle based structural colors," *Advanced Materials*, vol. 22, no. 39, pp. 4390–4394, 2010.

[162] J. Li, J. Shim, J. Deng, J. Overvelde, X. Zhu, K. Bertoldi, and S. Yang, "Switching periodic membranes via pattern transformation and shape memory effect," *Soft Matter*, vol. 8, no. 40, pp. 10322–10328, 2012.

[163] H. Xu, C. Yu, S. Wang, V. Malyarchuk, T. Xie, and J. Rogers, "Deformable, programmable, and shape-memorizing micro-optics," *Advanced Functional Materials*, vol. 23, no. 26, pp. 3299–3306, 2013.

[164] J. Leng, X. Lan, Y. Liu, and S. Du, "Shape-memory polymers and their composites: stimulus methods and applications," *Progress in Materials Science*, vol. 56, no. 7, pp. 1077–1135, 2011.

[165] H. Meng and G. Li, "A review of stimuli-responsive shape memory polymer composites," *Polymer*, vol. 54, no. 9, pp. 2199–2221, 2013.

[166] X. Qi, G. Yang, M. Jing, Q. Fu, and F.-c. Chiu, "Microfibrillated cellulose-reinforced bio-based poly(propylene carbonate) with dual shape memory and self-healing properties," *Journal of Materials Chemistry A*, vol. 2, no. 47, pp. 20393–20401, 2014.

[167] H. Koerner, G. Price, N. Pearce, M. Alexander, and R. Vaia, "Remotely actuated polymer nanocomposites - stress-recovery of carbon-nanotube-filled thermoplastic elastomers," *Nature Materials*, vol. 3, no. 2, pp. 115–20, 2004.

[168] R. Mohr, K. Kratz, T. Weigel, M. Moneke, and A. Lendlein, "Initiation of shape-memory effect by inductive heating of magnetic nanoparticles in thermoplastic polymers," *Proceedings of the National Academy of Sciences of the United States of America*, vol. 103, no. 10, pp. 3540–3545, 2006.

[169] L. L. Beecroft and C. K. Ober, "Nanocomposite materials for optical applications," *Chemistry of Materials*, vol. 9, no. 6, pp. 1302–1317, 1997.

[170] Y. Zhang, Q. Wang, C. Wang, and T. Wang, "High-strain shape memory polymer networks crosslinked by SiO_2," *Journal of Materials Chemistry*, vol. 21, no. 25, p. 9073, 2011.

[171] A. Chandra, L.-s. Turng, S. Gong, D. C. Hall, and D. F. Caulfield, "Study of polystyrene/titanium dioxide nanocomposites via melt compounding for optical applications," *Polymer Composites*, vol. 28, no. 2, pp. 241–250, 2007.

[172] J. Gutierrez, A. Tercjak, and I. n. Mondragon, "Transparent nanostructured thermoset composites containing well-dispersed TiO_2 nanoparticles," *Journal of Physical Chemistry C*, vol. 114, no. 51, pp. 22424–22430, 2010.

[173] G. Arrachart, I. Karatchevtseva, A. Heinemann, D. J. Cassidy, and G. Triani, "Synthesis and characterisation of nanocomposite materials prepared by dispersion of functional TiO_2 nanoparticles in PMMA matrix," *Journal of Materials Chemistry*, vol. 21, no. 34, p. 13040, 2011.

[174] J. L. H. Chau, C.-T. Tung, Y.-M. Lin, and A.-K. Li, "Preparation and optical properties of titania/epoxy nanocomposite coatings," *Materials Letters*, vol. 62, no. 19, pp. 3416–3418, 2008.

[175] C. Tsai, H. Yen, W. Chen, and G. Liou, "Novel solution-processable optically isotropic colorless polyimidothioethers-TiO_2 hybrids with tunable refractive index," *Journal of Materials Chemistry*, vol. 22, no. 33, p. 17236, 2012.

[176] H. Cao, J. Y. Xu, S. Chang, and T. Ho, "Transition from amplified spontaneous emission to laser action in strongly scattering media," *Physical Review E*, vol. 61, no. 2, pp. 1985–1989, 2000.

[177] M. Van Albada and A. Lagendijk, "Observation of weak localization of light in a random medium," *Physical Review Letters*, vol. 55, no. 24, pp. 2692–2695, 1985.

[178] P. E. Wolf and G. Maret, "Weak localization and coherent backscattering of photons in disordered media," *Physical Review Letters*, vol. 55, no. 24, pp. 2696–2699, 1985.

[179] Y. Chung, K. Yang, J. Choi, and B. Chun, "Characterisation and application of polyurethane copolymers grafted with photoluminescent dyes," *Coloration Technology*, vol. 130, no. 4, pp. 305–313, 2014.

[180] A. H. Torbati, R. T. Mather, J. E. Reeder, and P. T. Mather, "Fabrication of a light-emitting shape memory polymeric web containing indocyanine green," *Journal of Biomedical Materials Research - Part B Applied Biomaterials*, vol. 102, no. 6, pp. 1236–1243, 2014.

[181] Y. Zhang, Y. Li, and W. Liu, "Dipole-dipole and H-bonding interactions significantly enhance the multifaceted mechanical properties of thermoresponsive shape memory hydrogels," *Advanced Functional Materials*, vol. 25, no. 3, pp. 471–480, 2015.

[182] T. Ohzono, K. Suzuki, T. Yamaguchi, and N. Fukuda, "Tunable optical diffuser based on deformable wrinkles," *Advanced Optical Materials*, vol. 1, no. 5, pp. 374–380, 2013.

[183] M. A. Noginov, H. J. Caulfield, N. E. Noginova, and P. Venkateswarlu, "Line narrowing in the dye solution with scattering centers," *Optics Communications*, vol. 118, no. 3, pp. 430–437, 1995.

[184] J. Kitur, G. Zhu, M. Bahoura, and M. A. Noginov, "Dependence of the random laser behavior on the concentrations of dye and scatterers," *Journal of Optics*, vol. 12, no. 2, p. 024009, 2010.

[185] J. M. Haberl, A. Sánchez-Ferrer, A. M. Mihut, H. Dietsch, A. M. Hirt, and R. Mezzenga, "Light-controlled actuation, transduction, and modulation of magnetic strength in polymer nanocomposites," *Advanced Functional Materials*, vol. 24, no. 21, pp. 3179–3186, 2014.

[186] M. López-García, *Self assembled photonic-plasmonic crystals for light control at the nanoscale*. PhD thesis, Universidade de Santiago de Compostela, 2011.

[187] W. Cottrell, J. Wilson, and T. Foster, "Microscope enabling multimodality imaging, angle-resolved scattering, and scattering spectroscopy," *Optics Letters*, vol. 32, no. 16, pp. 2348–2350, 2007.

[188] E. Akkermans and G. Montambaux, *Mesoscopic physics of electrons and photons*. New York: Cambridge University Press, 2007.

[189] C. M. Aegerter and G. Maret, "Coherent backscattering and Anderson localization of light," *Progress in Optics*, vol. 52, pp. 1–62, 2009.

[190] P. D. García, *From photonic crystals to photonic glasses through disorder*. PhD thesis, Universidad Autónoma de Madrid, 2008.

General conclusions

Finally, the major milestones achieved on the course of this thesis are presented in the form of a brief summary.

- It was possible to combine the co-assembly growth technique with confinement in a wedge shaped cell in order to fabricate composite monolayers made of PS spheres embedded in a silica matrix. The samples were robust enough to withstand calcination in order to remove the sacrificial polymeric spheres. Extense and good quality inverse monolayers could be produced with this procedure. Attempts to replicate the structure into silicon were not successful whereas an exotic structure of inverse tetrapods was obtained.

- The co-doped, co-assembly method for one-step growing composite opals made of PS or PMMA spheres in a silica matrix were unfruitfull. In fact, adding the REs precursors, even in small quantities, severelly affected the stability of the particle colloids. Therefore, only amorphous composites could be processed. RE Atomic layer deposition of pregrown samples was effective for doping silica IOs, although PL studies revealed no significant effects induced by the presence of the ΓL pseudogap. Attempts to fabricate silicon IOs, aiming at similar PL studies in systems with a fPBG, alowed us only to achieve poor quality crystals with imense variability of the gap position. The fabrication process used revealed thus composed of a too large number of steps, each one introducing a large number of defects, thus had a very low throughput.

- We proposed an effective replica molding approach, to imprint hexagonal nanopatterns in the surface of SMPs. Due to the use of colloidal

monolayers as templates, this patterns are composed of nanobowls. It was demonstrated that they can perform as configurable gratings particularly, it was possible to tune the lattice parameter of the structure by mechanical deformation. The behavior of the diffraction angles in successive programming cycles agreed with the theoretically expected. Moreover, it was shown that the surfaces present self-healing capabilities. These results point out that the proposed system may be usefull for developping adaptative nanoptics devices, for example.

- Dispersing titania nanoparticles within the SMPs was effective for producing a novel kind of photonic white paint, that incorporates the SME as a new functionality. Transport properties of the material were assessed and shown to depend on the fillers concentration. Moreover, by doping the composites with organic dyes, it was demonstrated that these materials could perform as shape configurable active media, enabling ASE observation.

Acknowledgments

I would like to thank my supervisors Álvaro and Cefe for receiving me at their group, for establishing a very stimulating working environment and for all the support they gave me during these years. It was a pleasure and a privilege. I would also like to thank Dr. Luis Viña for his role as my tutor and for all the administrative help he provided.

I want to give a special acknowledgement to Marta and Juan. Marta for welcoming me so nicely in the chemistry lab, for her guidance and for always being available... for *being a sun*, in general. Juan for his incredible patience answering my questions. Sometimes, for his incredible patience answering my questions twice... I want to thank him for all his assistance and teaching about Optics and also Opera!

I want to acknowledge all my other colleges with whom, at some point, I overlaped at the Photonics Group of ICMM. Lola, who retired after my first year and provided me with one of the most delightful memories that I keep from when I first interviewed for my PhD. I want to thank Luis, who had a lot of rythm and made theory seem more relaxing. Nuno, for always having a good scientific conversation at hand and because it is nice to have a bit of home nearby. Martín because... well... this same reason? Ah! And also for the nice tips about Blender. Paco who enlightened me about Andaluz pronunciation. Victor, who first introduced me to this obscure science that is growing opals. The italian sector composed by Marco, Diego, Silvia and more recently Antonio. It was wonderful to share this time and learn with you. Victoria, for her contagious sympathy. Miguel, for his inteligent and ready comment. Alberto, for his teaching about the intrincacies of heavy metal. Luz, for her singular energy and for the good moments shared in the

lab. To Supratim, for introducing a bit of the other side of the world in our lives. Ángel, because is always interesting to discuss about technologies and Linux. Denise, for her canarian essence and to José, for always being in a good mood. I would like to thank some other people from the ICMM, in particular, Andrés and Carlos for the pleasant SEM sessions. Thank you so much also to the experienced technicians at the SIdI-UAM, specifically Dr. María José de la Mata and Francisco Urbano for their efficient assistance. I would like to thank to Dr. Concepción Gutiérrez for a friendly hand in many occasions and to Dr. Carlos Zaldo for relaxing escapes to the inspiring mountains nearby Madrid. To Marisa, for friendly discussions and taking care of my plants.

I want to express my gratitude to our colaborators in Lisbon, especially to Dr. Clara Gonçalves, Dr. Luís Fortes and to Giullia Smonker. I am sorry the things did not work the way we expected. I would like to thank Dr. Diederik Wiersma for giving me the possibility of doing the two month short stay at LENS, Firenze. Thank you also to Dr. Matteo Burresi for his assistance and patient supervision. I would like to acknowledge all the people with whom I contacted more directly in particular Kevin, Thomas, Romolo, Filippo, Rajesh, Lorenzo, Sara and Giacomo. Thank you so much also to the friends that I met, who made my stay at Firenze such a wonderful time namely Luísa, Carina, Eduardo, João, Martino, Nadia and Yannis. I hope I am not forgetting anyone... Thank you also to all the people in the University of Cambridge, in particular Dr. Silvia Vignolini, for help with the European seed project and receiving me for the short stay at her group. Thank you also to Dr. Ahu Dumanli, to Gen, Lisa and to the tireless Giullia. It was a memorable experience to work in your lab.

Me gustaría agradecer a Mariana, a Rui, a Gianna, a Valerio, a Celine, a Alain, a Gaelle, a Juanqui y a Emilio. Además, a David por su amistad y complicidad. Todos habéis hecho que mi venida a Madrid haya costado muy poco y mi paso por Tres Cantos haya sido extraordinario. Muchas gracias por las cenas multiculturales. Mi gratitud también a Stefania, a Elena y a Katja por los buenos recuerdos juntos. Finalmente, mi estancia en Madrid no hubiera sido lo mismo sin el cariño de María Concepción y Pedro, Noemi, Alba, Gabriel, Beatriz y Pedro A. Muchas gracias por acogerme de forma tan genial y por todo vuestro apoyo.

Claro, gostaria de enviar uma palavra de gratidão aos amigos Duarte e Cristina e ao Bernardo por momentos tão agradáveis. Quem diria que terminaríamos coincidindo em Madrid... Queria agradecer aos amigos da EMOS, sobretudo à Luísa, ao Diogo, à Chica (que ganas tenho de conhecer o pequenito Novo!), à Sara e ao Nuno. É das melhores coisas da vida, reencontrar a vossa amizade mesmo depois de longos meses sem nos vermos. O mesmo tam-

bém para a malta da Senhora da Hora. Agradeço ao Rui Pedro e à Lourdes, à Gisela e ao Chico, à Gouvinhas, à Andreia e às Joanas. É uma felicidade imensa ter crescido convosco e seguir contando com a vossa amizade ao longo dos anos. Agradeço-vos tanto por continuarmos a encontrar momentos para estarmos juntos. À Irina por ser uma lutadora nata. Ao Vasco, obrigado por não esquecer e quem sabe, alguma vez ainda toquemos esse Mozart juntos. Finalmente, obrigado à Marta por compreender tão bem e por um café boémio de vez em quando; ao Daniel e à Ana (não sabia bem se os devia incluir neste ou no seguinte parágrafo)... obrigado pelos jantares, pelos serões, pelas corridas e pela vossa presença constante.

Agradeço à minha família por ser um alicerce seguro. Obrigado pelo vosso encorajamento constante e por me ajudarem a construir e a lutar pelos sonhos. Pelo vosso carinho e por sofrerem tanto ou mais do que eu quando as coisas pareciam não sair do sítio. Obrigado aos meus pais por serem o modelo teórico com o qual valido as minhas experiências. Obrigado à mana pelo seu abraço terno e por sempre recordar que a poesia é a linguagem do coração. Obrigado ao Toninho e ao Alexandre pelos seus exemplos de determinação e às minhas avós Alice e Mercedes por fazerem com que cada regresso a casa seja tão belo. Ah! Obrigado pelas castanhas e pelos bacalhaus.

Finalmente, la última palabra va para Conchi, a quien he sido afortunado de conocer y enamorarme mientras realizaba la tesis. Si he podido tirar adelante y llegar a terminar este proyecto, sin duda que a ti es debido, tanto profesional como personalmente. Gracias por *suministrar la luz*! Gracias por las discussiones científicas, por tus consejos, por echar una mano amiga en el lab y por tu voluntad de experimentar cosas nuevas. Gracias por tu entusiasmo contagiante, por tu sonrisa y por tu *brilhozinho nos olhos*. Por hacerme feliz y querer compartir tu vida con la mía.